Scattering of State-Selected and Oriented Hydroxyl Radicals by Halogen Hydrides and Xenon

Scattering of State-Selected and Oriented Hydroxyl Radicals by Halogen Hydrides and Xenon
Moise, Angelica Valentina
PhD Thesis, Radboud University Nijmegen, The Netherlands – 2007
With references, summary in Dutch and Romanian
ISBN/EAN: 978-90-9021885-4
Subject headings: hydroxyl/halides/elastic, inelastic, reactive collisions/steric asymmetry
Front cover: photo of the hexapole (made by Leander Gerritsen)
Back cover: graph of the VUV intensities produced by frequency tripling in Xe-Ar mixture as function of the Ar pressure and the wavelength of the generated radiation

Scattering of State-Selected and Oriented Hydroxyl Radicals by Halogen Hydrides and Xenon

Een wetenschappelijke proeve op het gebied van de
Natuurwetenschappen, Wiskunde en Informatica

Proefschrift

ter verkrijging van de graad van doctor
aan de Radboud Universiteit Nijmegen
op gezag van de Rector Magnificus prof. mr. S.C.J.J. Kortmann,
volgens besluit van het College van Decanen
in het openbaar te verdedigen op dinsdag 28 Augustus 2007
om 15:30 uur precies
door

Angelica Valentina Moise
geboren op 4 Juli 1974
te Râmnicu-Sărat, Roemenië

Promotores: Prof. dr. J.J. ter Meulen
Prof. dr. D.H. Parker

Manuscriptcommissie: Prof. dr. ir. A. van der Avoird
Prof. dr. S. Stolte, Vrije Universiteit Amsterdam
Dr. N. J. Dam

Dit werk maakt deel uit van het onderzoekprogramma van de Stichting voor Fundamenteel Onderzoek der Materie (FOM), die financieel wordt gesteund door de Nederlandse Organisatie voor Wetenschappelijk Onderzoek (NWO).

Project FOM-N-05

To my parents
Părinților mei, 1 Cor. 13

Contents

Chapter 1

Introduction

1.1 General introduction

Molecules can influence each other via collisions, in which the interaction is probed over a large range of intermolecular distances. Collision processes are defined here as brief dynamic events consisting of the approach of two or more particles, resulting in the (ex)change of momentum, energy or mass. These processes may have a predominant elastic, inelastic or reactive character. In elastic scattering the total kinetic energy of the particles before and after the collision is the same, while in an inelastic collision, a transfer between kinetic and internal energy of the system takes place. Chemical reactions involve transfer of atoms or, for relativistic collisions, emission of subatomic particles. Molecular dynamics research encompasses at present a rich variety of laser and molecular beam techniques, and aims at a profound understanding of fundamental processes involving gases or plasmas.

For the collision of two molecules many initial parameters determine the pathway to the final state and its properties. Among these parameters the collision energy, the impact parameter, the internal energy and the relative orientation of the approaching molecules may be of great importance. Possible transient species and intermediate complexes determine the dynamical probabilities for the exit channels with specific mass, momentum and energy distribution among the stable products. Various research methods can elucidate the transformation of the molecules at the collision time scale. In our laboratory we study single collisions at well-defined conditions in a crossed molecular beam experiment. Laser radiation with pulses of a few nanoseconds is used to probe the initial and final states of the molecules undergoing a collision. The outcome of such a study can validate the theoretical models and their level of approximation on building the Potential Energy Surfaces.

Special attention is paid to molecules having one or more unpaired electrons in their outer shell. These molecules, called transient molecules or free radicals, are very reactive and thus short-lived under ambient conditions. Free radicals are involved in many atmospheric processes and in plasmas as intermediate products or catalysts and play a key role in numerous chain reactions. This thesis focuses on one of the most relevant free radicals, OH, and treats especially the behavior of the hydroxyl radical in bi-molecular inelastic and reactive scattering.

1.2 OH interactions

The hydroxyl radical plays a crucial role in atmospheric chemistry [1-5]. In the mesosphere the presence of OH, H, NO, HO_2, O_2, and O_3 is common and the most prominent chemical reactions producing OH are: $H_2O + h\nu \rightarrow OH + H$, where $h\nu$ is the energy of an ultraviolet photon corresponding to the wavelength < 240 nm, and $H_2O + O \rightarrow OH + OH$. Among the most efficient reactions taking place in the stratosphere, the following lead to the formation of the radical [1, 2]: $H_2 + O \rightarrow OH + H$ and $CH_4 + O \rightarrow OH + CH_3$. In the troposphere OH is produced by UV photodissociation of ozone and subsequent reaction of the emerging O (^1D) with water vapour [3, 4]: $O_3 + h\nu$ (< 340 nm) $\rightarrow O(^1D) + O_2$, $O(^1D) + H_2O \rightarrow OH + OH$.

Chemical reactions with OH initialize the removal of green-house gases, like carbon monoxide and methane, and of volatile organic compounds (part of them carcinogenic) [4, 5]. Therefore, OH is called the detergent of the atmosphere. Nearly all the organic compounds react with OH, a fact that makes it one of the main atmospheric oxidants. Only few very stable compounds like chlorofluorocarbons, nitrous oxide or carbon dioxide do not react at all or react very slowly with OH [5, 6]. The hydroxyl radical has a strong tendency to abstract hydrogen atoms from organic compounds RH whenever possible and to form water. In the next step the radical R reacts with oxygen and forms organic peroxides that are involved in the ozone formation cycle. Reactive also with the special class of organic compounds of alkenes, OH tends to add to the double bond as long as the H abstraction is not statistically favored [6].

Several species X have been suggested [3-5] for the catalytic ozone destruction in the atmosphere via the reaction $X + O_3 \rightarrow XO + O_2$ followed by $XO + O \rightarrow X + O_2$, with the net effect of: $O_3 + O \rightarrow 2O_2$. The most common of such species have been identified to be free radicals and are classified in three main categories: HO_n, NO_n and ClO_n. Other possibly important species involve Br and I atoms. The iodine as well can efficiently catalyse the ozone destruction in the stratosphere and marine troposphere. Man has made significant contributions to the atmospheric burdens of these species, especially those involving chlorine and bromine. Depending on the altitude and the mixing ratio, each species has a varying ability to destroy ozone. Near the stratosphere the HO_n radicals account for up to 70% of the total ozone destruction including only the oxygen processes [3, 4].

The detailed study of the scattering processes can provide a large contribution to the understanding of complex phenomena such as flames and plasmas, since inelastic and reactive collisions contribute to the chemistry dynamics evolving there and shape the regime of production or quenching of various molecular species [8]. The OH radical can be abundant in all plasmas where O_2 or H_2O are present.

Combustion chemistry is another field where its importance is substantial. In the final step of hydrocarbon oxidation OH reacts with CO forming CO_2 [7, 8]. For the H abstraction in flames the equilibrium reaction rate controls the amount of water vapor production. The reaction of OH radicals with the simplest hydrocarbon, CH_4, is of great importance since it represents the most significant depletion channel for atmospheric methane at low temperatures [3] and a propagation reaction in methane combustion at high temperatures. Because of atmospheric and combustion interest, there are 95 studies of this reaction listed in the current NIST database [9].

The maser radiation from interstellar space is ascribed to radiative pumping and collision processes involving selective redistribution of rotational population in molecular scattering [10, 11]. Population inversion of molecules is occasionally achieved under natural conditions in interstellar space, creating bright spectral line sources [11]. The OH molecule was the first to be detected as a maser [12]. Other important species that have "masing" transitions are H_2O, SiO and CH_3OH. Except CH_3OH, all occur in the envelopes of evolved stars in the interstellar medium [11]. The understanding of these maser phenomena is therefore essential in the study of star formation processes.

1.3 Research goals

Elastic, inelastic and reactive channels compete and contribute to the final results of a molecular collision process. This interplay of various energy exchanges in the collisions of the OH radical, as function of key parameters, is the goal of the experimental research presented in this thesis. Parameters such as the physical-chemical nature of the collision partner, relative orientation, translation and internal energy are to some extent experimentally tuneable and therefore become a tool of enhancing or suppressing different intermolecular interaction pathways. Molecules with a predicted high reactive affinity with respect to the hydroxyl radical have been chosen: HCl, HBr and HI.

A wealth of experimental and theoretical studies has elucidated the OH-HCl interaction and reaction dynamics. Quantitative information on the reactivity of the OH + HCl system is provided by an extensive set of kinetic experiments in which temperature dependent rate constants were measured in a wide temperature range [13-20]. Several theoretical studies reported to date, approached the OH + HCl system at different levels of theory in order to develop the Potential Energy Surface (PES) governing the interaction and to calculate rate constants and reaction cross sections [21-26]. A PES suitable for calculations for the non-reactive channel was lately presented [26]. The accuracy of different features of this PES was refined in order to allow for state-resolved quantum scattering calculations.

Various kinetic studies on the OH + HBr system have been reported as well, resulting in the determination of reaction rate constants as a function of temperature [27-31]. The theoretical calculations [21, 32, 33] revealed a higher reactivity and smaller reaction barrier for the OH + HBr reaction compared with the OH + HCl reaction. The PES of the OH-HI interaction is less known. Reported kinetic studies of the OH + HI reaction indicate a large rate coefficient and no significant activation barrier [34-39]. Concerning the reaction with the OH radical, among the three HX halides, X = Cl, Br and I, the HI molecule is found to have the highest room temperature rate and the highest exothermicity.

In spite of the great number of studies devoted to the reactivity of these systems, no experiments concerning the state-to-state scattering of OH by HCl, HBr and HI have been reported so far. For the experiments described in this work, the molecular beam technique and hexapole electrostatic fields are employed for the selection and focusing of OH molecules in a single energy state ($X\ ^2\Pi_{3/2}$, J = 3/2, f) enabling the determination of the state-to-state cross sections, which test in detail the computed PES. Subsequently, these molecules are oriented in a uniform electric field so that they collide with either the O-side or the H-side directed to the collision partner. The measured steric effects contain as well very detailed information about the PES. Similar experimental methods are used for the inelastic scattering of oriented NO radical by rare-gas atoms [40] and for the reactive scattering of oriented methyl-iodide molecules by Rubidium atoms [41].

In order to extend the field of comparison on the basis of mass, electric moments and polarizability of the collision partner for OH, the scattering of OH by Xe has been studied as well. Atomic Xe has a relatively large polarizability and a mass very close to that of the HI molecule. Thus, a comparison between these systems may infer which measurable quantities are affected mainly by the interactions based on the permanent electric moments of the HI molecule. Related to a survey of the interactions of OH with the rare gases, the previously obtained experimental results for the inelastic scattering of OH by He [42] and by Ar [43] and the features of the PES's of these 3-atom systems [44, 45] are available for comparison. With the increase of the polarizability going from He and Ar to Xe one would expect a relatively stronger interaction with the polar OH molecule.

An intrinsic issue addressed by these atom-molecule or bi-molecular interaction studies is a detailed description of the contribution to the interaction of each type of intermolecular force, long-range electrostatic or forces of quantum mechanical nature. The analysis of the inelastic scattering experimental results attempts also to correlate the type and strength of the dominant interaction with the configurations and binding energies of the van der Waals complexes and thus to the anisotropy of the PES. The propensities for particular orientations (before) and internal states (after the molecular impact) need to be traced to their origin.

In addition to the inelastic state-to-state collision studies we tried to measure reaction products. Hereto the REMPI detection technique was applied using various excitation schemes. Thus far no successful REMPI experiments on state-to-state reactions of OH have been reported. Very recently Kasai et al. have observed the Br product of the OH + HBr reaction by the use of LIF [46].

1.4 Outline

Five more chapters follow the introduction in this thesis. The experimental methods employed are described in **Chapter 2** including the experimental set-up, general spectroscopic features and experimental methods for the preparation and the detection of the hydroxyl radical, the deduction of the cross sections and steric asymmetries from the measured quantities and the characterization of the OH collision partners. **Chapter 3** presents attempts to study the crossed beam reactive scattering of the state-selected hydroxyl radical by HCl, HBr and HI. The measured state-to-state relative cross sections and steric-asymmetries for the OH-HX, with X = Cl, Br and I, and OH-Xe scattering systems are presented in the following chapters as qualitative comparisons: of the OH-HCl with the OH-CO and OH-N_2 systems in **Chapter 4**, of the OH-HCl, OH-HBr and OH-HI systems in **Chapter 5** and of the OH-Xe with the previously studied OH-He and OH-Ar systems in **Chapter 6**. Effects on the interaction and on the experimental results of the nature and polarity of the OH collision partner and the collision energy are discussed. In **Chapter 6** an analysis using the more extensive theoretical information related to the atom-diatom interaction is made.

Chapter 2

Experimental methods

2.1 Experimental set-up

The experimental set-up for the crossed beam experiment [47], shown in Fig.2.1, is composed of three main parts: one for the production and subsequent selection and orientation of the OH molecular beam, the second one for the formation of the OH collision partner beam and the third one for the collision of the two molecular beams and the detection.

The OH beam is produced by expanding 3% H_2O in Ar through a pulsed valve (Jordan) with a nozzle opening of 0.2 mm diameter and working at 10 Hz. The pulse duration is 50 μs (FWHM). The backing pressure is typically 800 mbar. In the supersonic expansion the molecular beam is internally cooled down to a rotational temperature of 35 K. At 3 mm from the nozzle a stainless steel ring with an inner diameter of 3 mm is kept at - 4 kV, producing an electrical discharge in the expanding mixture. After passing a skimmer with an opening of 2.5 mm diameter and at a voltage of – 300 V to deflect the ions formed in the discharge, the beam molecules enter a double hexapole state-selector with 6mm inner diameter and 2.5 mm cylindrical rods.

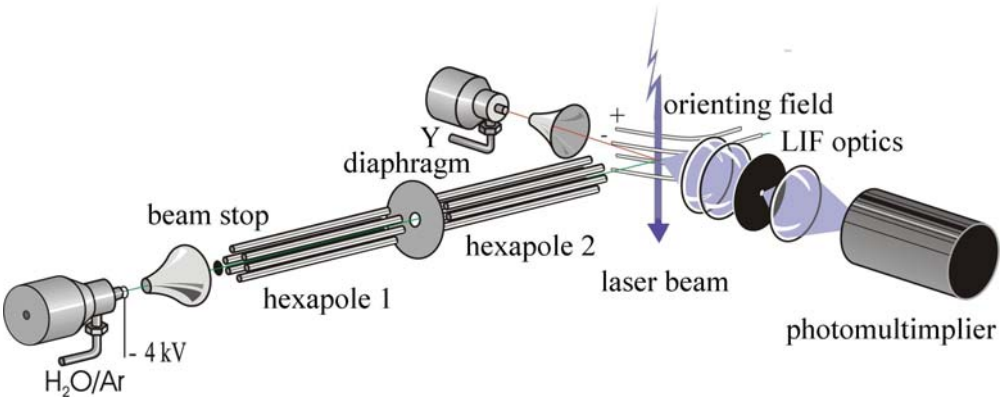

Fig. 2.1 *The experimental set-up for the measurements of inelastic scattering of the OH molecules*

A beam stop with a 2 mm diameter is placed on the molecular beam axis in front of the state selector to block molecules which fly along the central axis and do not experience any field for the selection. The hexapole voltage is set to focus OH molecules in a selected internal state for the first time half way along the state selector and for the second time into the region of collisions with the secondary beam. This geometry allows the blocking of OH molecules in the other low field seeking states by inserting a diaphragm with a diameter of 3.5 mm in between the 120 mm long halves of the hexapole.At the exit of the state selector the OH molecules may experience another external field used for orientation with respect to the collision partner. This orientation field produced by four parallel rods kept at alternating positive and negative high voltage has an intensity of 7.5 kV/cm [48] in collision region of the molecular beams and a direction parallel to the relative velocity of the beams. The distance between the axes of the adjacent rods for the orientation electric field is 17 mm, which provides a homogeneous electric field distribution over the crossing region of the molecular beams. In combination with the state selector the orientation field prepares the OH molecules with the H or O end directed towards the collision partner, prior to collision event.

2.2 Detection of the OH molecule

The OH molecules are detected by Laser Induced Fluorescence (LIF) using the A $^2\Sigma^+$, v' = 0 $\leftarrow$ X $^2\Pi_{3/2}$, v" = 0 transition at 308 nm. These two electronic states are presented here in more detail. The notations used for the molecular angular momenta are: the total electronic orbital angular momentum $\vec{L}$, the total electronic spin angular momentum $\vec{S}$, the angular momentum of the molecular end-over-end rotation $\vec{R}$, the total orbital-rotational quantum number $\vec{N} = \vec{L} + \vec{R}$ and the total molecular angular momentum $\vec{J} = \vec{L} + \vec{S} + \vec{R}$.

The Laser Induced Fluorescence method probes the population distribution of the OH molecules in the ground electronic and vibrational state. The molecules absorb one UV photon and are excited to a rotational state in the first excited electronic state. The decay from this excited state is strongly fluorescent. For the $^2\Sigma \leftarrow {}^2\Pi$ electric dipole transitions the selection rules are given by [49, 50]:

$$\Delta J = 0, \pm 1; \Delta N = 0, \pm 1, \pm 2; \; + \leftrightarrow -, \tag{2.1}$$

where + and – denote the total parity (symmetry of the corresponding wavefunction with respect to an inversion of all the coordinates of the nuclei and electrons in the laboratory frame with the origin in the center of mass).

For the electronic transitions the notation convention is used as given by Dieke and Crosswhite [51] and LIFBASE 1.9 [52]. The O, P, Q, R and S branches designate the transitions for which ΔN is –2, -1, 0, 1 and 2, respectively. Two subscripts are used to indicate the spin-rotation label for the final state, f = 1, 2, and the spin-orbit label for the initial state, F = 1, 2, and only one of these subscripts is given if they are equal. In parenthesis the value of the N quantum number of the initial rotational state is given. To probe the OH molecules in the F_1 spin-orbit component with f and e symmetry, Q_1 (N) and P_1 (N) branches have been used, respectively, while in the case of the F_2 spin-orbit component the P_{12}, R_2 or P_2 (N) and Q_2 (N) branches have been used to probe the molecules in f and e states, respectively. The ρ-doublet splitting of the rotational states in the A state yielding satellite lines such as Q_{21} (N), P_{12} (N) or Q_{12} (N) is resolved except for the lowest rotational states (Ω = 3/2, J = 3/2, f; Ω = 1/2, J = 1/2, e and Ω = 1/2, J = 3/2, f), in which cases the change in the excitation rates is taken into consideration (see paragraph 2.4, Eq. 2.21). In particular, for N = 1, Ω = 1/2 only the satellite line exists. The vacuum wavelengths of the spectral lines used in this work as given by LIFBASE 1.9 [52] are reproduced in Table 2.1.

Upon relaxation of the molecules back to the ground state the fluorescence signal detected contains information about the population of the molecules that have been excited. The (0 – 0) band of the $A\ ^2\Sigma^+ \leftarrow X\ ^2\Pi$ transition can be saturated at low laser fluencies, which simplifies the deduction of the initial state population from the fluorescence signal, since the transition strength is independent of the rotational state.

The second harmonic generation of a Nd-YAG laser with a 5 ns pulse length and 10 Hz repetition rate is used to pump a dye laser (Lambda Physik model Scanmate 2) operating with Sulforhodamine SR 640. The doubled output is set at 0.5-0.8 mJ/pulse in order to prevent line broadening and still saturate the absorption. The laser bandwidth of 0.45 cm^{-1} allows the spectral resolution of all OH transitions used, except for the Q_2 (2) and Q_2 (3) transitions. A system of two lenses and a UG-11 filter is used to transmit the fluorescent light onto the photo-multiplier tube (EMI 9235 QB). The laser beam is passed through light baffles before and after the detection region and is dumped into a Wood's horn in order to reduce the background due to the laser beam. Gated boxcar signals are accumulated over 2000 shots with secondary valve modulation every 128 shots during which the gas pulse is delayed or not by 1ms with respect to the primary beam. Subtraction of the modulated signals gives the effect of the collisions: an in- or out-scattering signal. Ten to 80 measurements have been used for each rotational state to deduce the mean value of the LIF intensity and its accuracy by weighted averaging.

Table 2.1: *Vacuum wavelengths (nm), of transitions belonging to the rotational branches of OH $A\ ^2\Sigma^+ \leftarrow X\ ^2\Pi_{3/2}$ (0 – 0) used in this work [52]. J" designates the total angular momentum quantum number of the ground state. An explanation of the notation is given in the text.*

J"	P_1	Q_1	Q_{21}	Q_2	Q_{12}	P_{12}	P_2	R_2
0.5	--	--	--	309.138	309.135	309.462	--	308.494
1.5	308.256	307.933	307.937	309.076	309.071	309.724	309.727	308.113
2.5	308.729	308.085	308.090	309.075	309.067	310.044	310.050	307.792
3.5	309.209	308.244	308.252	309.127	309.117	310.417	310.425	307.526
4.5	309.702	308.417	308.427	309.226	309.214	310.836	310.846	307.310
5.5	310.213	308.610	308.621	309.369	309.355	311.297	311.309	307.137
6.5	310.745	308.824	308.838	309.552	309.536	311.796	311.810	307.007

2.2.1 The electronic ground state

In the united atom representation the electronic configuration of the X $^2\Pi$ state of OH molecule is $(1s\sigma)^2\ (2s\sigma)^2\ (2p\sigma)^2\ (2p\pi)^3$. Regarding the angular momenta couplings, this state is described by an intermediate case between Hund's cases (a) and (b) [49]. A (near) Hund's case (a) is appropriate for the lowest few rotational states, while for increased rotational excitation the nuclear and electronic momenta coupling allows relatively more freedom to the spin vector and gives way to the mixing of the cases (a) and (b).

As a characteristic of Hund's case (a) the total electronic orbital and spin angular momentum, $\vec{L}$ and $\vec{S}$ respectively, are coupled to the internuclear axis. Their projections on this axis, Λ and Σ, have the absolute values of 1 and 1/2, respectively. The conserved quantities are J^2, M (the component of $\vec{J}$ on an external axis) and the sum $\Omega = |\ \Lambda + \Sigma\ |$. The molecular rotational angular momentum $\vec{R}$ couples to $\vec{\Omega}$, which is parallel to the molecular axis, forming the total angular momentum, $\vec{J}$.

The strong spin-orbit interaction determines two components of the projection Ω on the internuclear axis of the total molecular angular momentum; these components are: Ω = 3/2 (labeled F_1) and Ω = 1/2 (labeled F_2), of which F_1 lies lower in energy. The quantum number J is given by Ω + R, with R ≥ 0. The Hamiltonian for the spin-orbit interaction and for the molecular rotation can be written:

$$H_{rot} = A_v \vec{L} \cdot \vec{S} + B_v (\vec{R})^2, \tag{2.2}$$

where A and B are the spin-orbit coupling and rotational constants, respectively, and v designates the vibration quantum number. For the ground state of the hydroxyl radical these constants are: $A_0 = -139.73$ cm^{-1}and $B_0 = 18.52$ cm^{-1} [51]. As basis wavefunctions of this Hamiltonian we can consider the rigid rotor wavefunctions multiplied by the electron spin and orbital angular wavefunction [53]:

$$\psi = |\Omega JM\rangle |\Lambda\Sigma\rangle, \tag{2.3}$$

where the rigid rotor basis functions are related to the Euler rotation matrix as follows:

$$|\Omega JM\rangle = \sqrt{\frac{2J+1}{8\pi^2}} \cdot D^{J*}_{M\Omega}(\theta, \varphi, 0). \tag{2.4}$$

The M quantum number can take 2J + 1 values ranging from – J to + J. The energy of the rotational state is given by [53]:

$$E_{rot} = B_v \cdot (J-1/2) \cdot (J+3/2) \pm [B_v^2 \cdot (J+1/2)^2 + A_v(A_v-4)/4]^{1/2}, \tag{2.5}$$

with the plus sign for the Ω = 3/2 states and the minus states for the Ω = 1/2 states. These energy levels are degenerate, i.e. the same value of the internal energy corresponds to many (2J+1) different states, depicted by sets of good quantum numbers Ω, J, M_J, ε. Two doubly degenerate states are correlated to the two opposite directions of the projections of $\vec{J}$ on the internuclear axis, ± Ω. Conventionally, the positive direction of Ω on the molecular axis is chosen from the O side to the H side, as for the dipole moment direction. This degeneracy is lifted by a perturbation of the Π state due to nearby Σ states. As a result, the coupling of the nuclear rotation and the electronic orbital angular momentum, the $\vec{R} \cdot \vec{L}$ interaction, determines a splitting of the rotational levels, called Λ-doubling.Corresponding to the rotationless parity [54], the spectroscopic symmetry labels are e (ε = +1) and f (ε = -1), where ε is the symmetry of the wavefunction defined below. The total parity is given by [53, 54]:

$$p = \varepsilon \cdot (-1)^{J-1/2}. \tag{2.6}$$

The basis functions for each Λ-doublet state can be chosen as:

$$\left|\Omega JM\varepsilon\right\rangle = \frac{1}{\sqrt{2}}\left(\left|\Omega JM\right\rangle + \varepsilon\left|-\Omega JM\right\rangle\right). \tag{2.7}$$

For stronger Hund's case (b) character, Ω loses its relevance as a good quantum number, the two spin-orbit components F_1 (Ω = 3/2) and F_2 (Ω = 1/2) start to mix and the wavefunctions are linear combinations of the pure F_1 and F_2 functions:

$$\left|\Omega JM\varepsilon\right\rangle = C_{\Omega,3/2}\left|3/2\, JM\varepsilon\right\rangle + C_{\Omega,1/2}\left|1/2\, JM\varepsilon\right\rangle. \tag{2.8}$$

The C coefficients reflect the degree of mixing of the two spin-orbit components. The ground state OH molecules exhibit a pure Hund's case (a) for Ω = 1/2, J = 1/2 and a gradual mixing with case (b) for increasing J. The magnitude of the Λ-doublet splitting, dependent on the spin-orbit mixing coefficients C, is about 0.055 cm^{-1} for the lowest rotational state and increases with increasing rotational excitation in the Ω = 3/2 ladder [55, 56]. The spectral hyperfine splitting due to the nuclear spin of the hydrogen atom cannot be resolved within the spectral bandwidth of the laser used.

Regarding the symmetry of the electronic wavefunction with respect to a reflection in the rotation plane the notation A' and A" is used for the symmetric and anti-symmetric configurations, respectively [57]. The A" configuration corresponds to the situations where the π orbital of the unpaired electron is perpendicular to the plane of the end-over-end rotation, which is the case for Ω = 3/2, f and Ω = 1/2, e states. In the A' configuration the half filled π orbital is in the plane of rotation, which is the case for Ω = 3/2, e and Ω = 1/2, f states.

2.2.2 The first excited electronic state

In the united atom representation the electronic configuration of the $A\ ^2\Sigma^+$ state of the OH molecule is $(1s\sigma)^2\ (2s\sigma)^2\ (2p\sigma)\ (2p\pi)^4$. This state of OH can be described by a Hund's case (b), for which Λ = 0 and S = 1/2. The nuclear rotation-electron spin interaction is significant. The electron spin angular momentum, $\vec{S}$, is not coupled to the internuclear axis; therefore S is a good quantum number.

The total angular momentum, J, can take all half integer values from R-S to R+S [49]. Consequently, each rotational level of the A $^2\Sigma^+$ state is split into 2 components (ρ-doublet). The rotational energy of these two spin-rotation components is given by [49]:

$$E_{rot,f_1} = B_v R(R+1) + \frac{1}{2}\gamma R, \quad \text{for } J = R + \frac{1}{2} \quad (f_1), \tag{2.9a}$$

$$E_{rot,f_2} = B_v R(R+1) - \frac{1}{2}\gamma (R+1), \quad \text{for } J = R - \frac{1}{2} \quad (f_2). \tag{2.9b}$$

Here γ is the spin-rotation coupling constant and has the value of 0.224 cm^{-1} for the ground vibrational state of the A electronic state [58], while the rotational constant B_0 is 19.961 cm^{-1} [51]. The parity is given by [53]:

$$p = (-1)^R. \tag{2.10}$$

A simplified diagram of the energy levels of the ground and first excited electronic states of OH is depicted in Fig. 2.2.

2.3 Stark effect of OH

Due to their large permanent dipole moment, μ = 1.668 Debye [59], the OH molecules can be spatially selected, filtered and oriented. The detailed characterization of the state selection and orientation of the OH molecule via the Stark effect has been given previously [48, 60-62]. A short description is presented in this paragraph to support the treatise in the following chapters.

In a vector representation the total angular momentum, $\vec{J}$, precesses around the direction of the external electric field. The $\vec{J}$ vector has 2J + 1 quantized projections on the electric field axis. For each value of this projection, M_J, corresponding to one set of J, Ω quantum numbers, a certain degree of average orientation of the molecules with respect to the electric field is achieved (Figure 2.3).

The Hamiltonian describing the interaction between the permanent dipole moment $\vec{\mu}$ and the external electric field $\vec{E}$ is [49, 50, 54]:

$$H' = -\vec{\mu} \cdot \vec{E}. \tag{2.11}$$

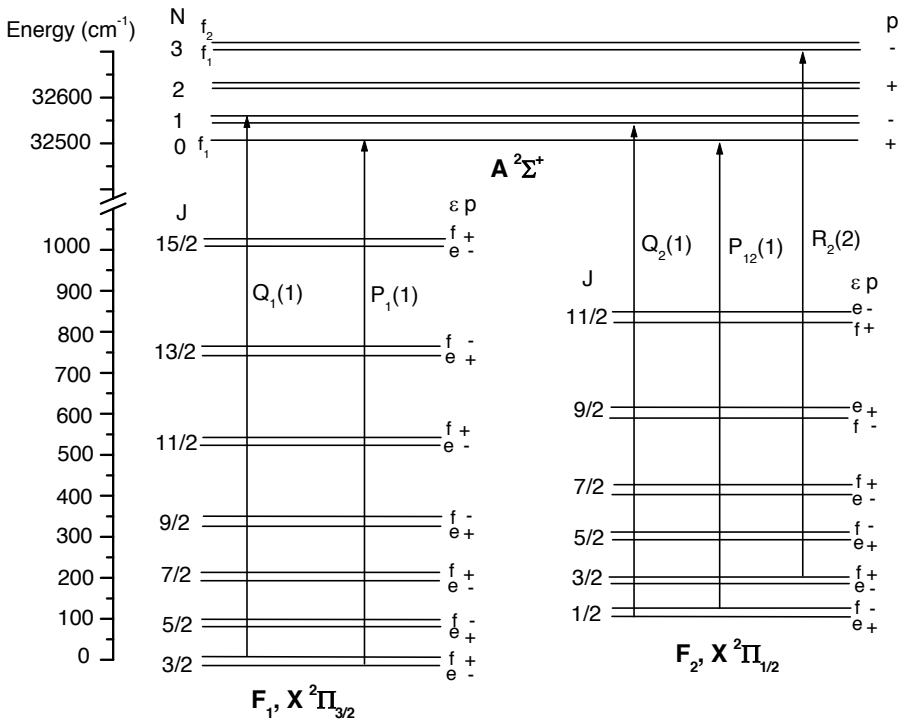

Fig. 2.2 *Rotational energy levels for the ground and first excited electronic states of OH molecule. The Λ- and ρ-doublet splitting are not shown to scale. For the lowest electronic state J has the values: N + 1/2 for* F_1, *Ω = 3/2, and N - 1/2 for* F_2, *Ω = 1/2, where N is given by R+/Λ/. For the excited state, N = R, each N value corresponds to two values of total angular momentum quantum number: J = N + 1/2 (*f_1*) and J = N – 1/2 (*f_2*). Some electric dipolar transitions are depicted:* Q_1 *(1),* P_1 *(1),* Q_2 *(1),* P_{12} *(1) and* R_2 *(2). The conventional notation is given in the text.*

The matrix elements of this Hamiltonian between the Hund's case (a) basis functions are non-zero if J = J', Ω = Ω' and $M_J = M_{J'}$, in which case they are given by [48, 53]:

$$\left\langle \Omega J M_J \left| H' \right| \Omega J M_J \right\rangle = -\mu E \frac{M_J \Omega}{J(J+1)}. \qquad (2.12)$$

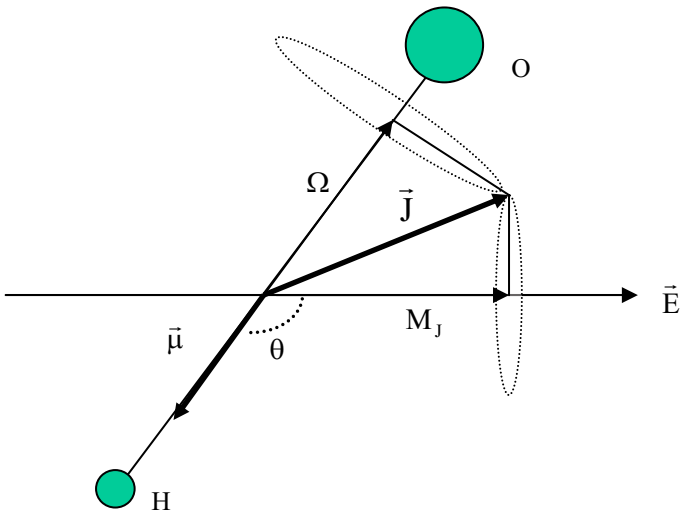

Fig. 2.3: *Vector representation for the total angular momentum* $\vec{J}$ *with its projections and the dipole moment* $\vec{\mu}$ *of the OH molecule in the ground electronic state. The space fixed axis Z is chosen in the direction of the external field* $\vec{E}$ *and the molecular axis Z' has the direction from the O atom to the H atom (parallel to the dipole moment). The Z and Z' directions make the angle θ, a measure of the degree of orientation.*

As mentioned in paragraph 2.2, the ground state of OH is characterized by an intermediate Hund's case and its eigenfunction is thus a mixing of the two spin-orbit component Ω = 1/2 and Ω = 3/2 basis functions. Following Eqs. (2.6) and (2.7) the eigenfunctions in the absence of the electric field can be written:

$$\left|\Omega\, J\, M_J\, \varepsilon\right\rangle = \frac{C_{\Omega,3/2}}{\sqrt{2}}\left(\left|3/2\, J\, M_J\right\rangle - \varepsilon\left|-3/2\, J\, M_J\right\rangle\right) + \frac{C_{\Omega,1/2}}{\sqrt{2}}\left(\left|1/2\, J\, M_J\right\rangle - \varepsilon\left|-1/2\, J\, M_J\right\rangle\right), \quad (2.13)$$

where $C_{\Omega,\,3/2}(J)$ and $C_{\Omega,\,1/2}(J)$ are the spin-orbit mixing coefficients, values of which are given in Ref. [55, 56].

The Stark Hamiltonian matrix elements on this basis are zero for states with the same ε symmetry (e or f). The matrix elements that couple states with different symmetry are given by:

$$\langle \Omega\, J\, M_J\, f \,|H'|\, \Omega\, J\, M_J\, e\rangle = \langle \Omega\, J\, M_J\, e \,|H'|\, \Omega\, J\, M_J\, f\rangle =$$

$$= -\mu E \frac{M_J}{J(J+1)}\left[\frac{3}{2}(C_{\Omega,3/2})^2 + \frac{1}{2}(C_{\Omega,1/2})^2\right]. \qquad (2.14)$$

In the presence of the external electric field two correlated effects appear: a (Stark) splitting of the energy levels and a mixing of the ε symmetries, e and f. Both effects increase with the magnitude of the electric field applied. The energy corresponding to the two Λ-doublet sublevels in the presence of an external electric field, E, can be expressed as a function of the electric field intensity, E, and the Λ-doublet splitting in the absence of the electric field, Δ_0, as follows [48]:

$$W_{f/e} = \frac{\Delta_0}{2}\left(1 \pm \sqrt{1 + \left[\frac{2 \cdot Q(E)}{\Delta_0}\right]^2}\right), \qquad (2.15)$$

where the + sign holds for the expression of W_f and the – sign holds for the expression of W_e and Q(E) is the matrix element of the potential given by the expression (2.14).
In Fig. 2.4, the Λ-doublet splitting of the Ω = 3/2, J = 3/2 state is shown as a function of the intensity of the electric field. The internal energy corresponding to the lowest e sub-states decreases with the electric field and therefore these states are called *high field seeking* states. Similarly, the upper energy sub-levels, f, correspond to *low field seeking* states. These properties allow the manipulation of the OH molecules trajectories by means of inhomogeneous electric fields.Another effect of the electric field is parity or symmetry mixing. If an external electric field is applied the eigenfunctions become a linear combination of the eigenfunctions (given in Eq. 2.13) for zero electric field. The labels e and f lose their designation with the increase of the external electric field intensity. The experiments presented here are performed at relatively low field strengths, conditions for an intermediate regime between pure parity states and fully mixed parity states, when parity has no longer a meaning. The new eigenfunctions, labeled by correspondence to the ones in zero external field, become [48, 64, 65]:

$$\psi_f = \alpha(E)|\, \Omega\, J\, M_J\, f > + \beta(E)|\, \Omega\, J\, M_J\, e > \qquad (2.16a),$$

$$\psi_e = \alpha(E)|\, \Omega\, J\, M_J\, e > - \beta(E)|\, \Omega\, J\, M_J\, f > \qquad (2.16b),$$

where α and β are the parity mixing coefficients, normalized such that the sum of their squares is one.

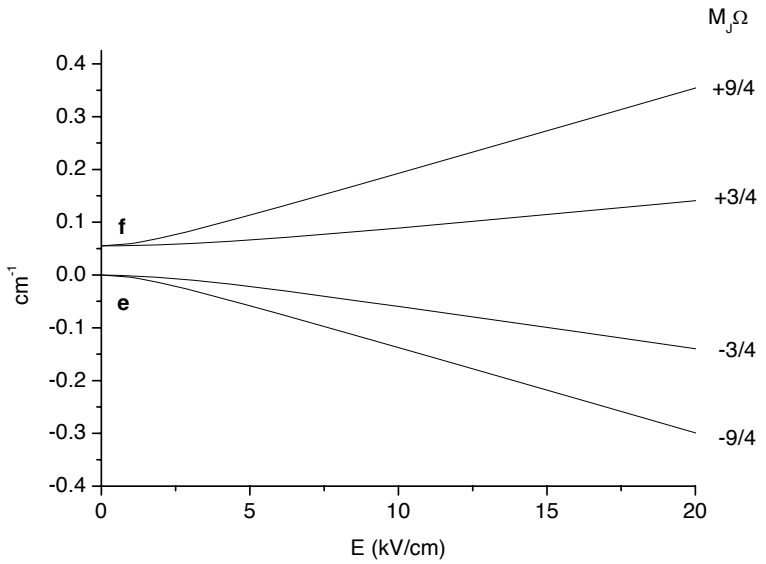

Fig. 2.4: *Stark energy level splitting for OH $X\,^2\Pi_{3/2}$, J = 3/2 [63]. The 2 J + 1 = 4 fold degeneracy is lifted partially by the Λ-doublet splitting and fully in the electric field.*

The value of β^2 within the interval [0,1] indicates the degree of mixing. These coefficients are given by [60]:

$$\alpha(E) = \frac{1}{\sqrt{2}} \sqrt{1 + \frac{1}{\sqrt{1 + \left(\frac{2Q(E)}{\Delta_0}\right)^2}}}, \tag{2.17a}$$

$$\beta(E) = \mp \frac{1}{\sqrt{2}} \sqrt{1 - \frac{1}{\sqrt{1 + \left(\frac{2Q(E)}{\Delta_0}\right)^2}}}. \tag{2.17b}$$

The plus and minus sign in Eq. (2.17b) holds for positive and negative M_J, respectively.

An illustration of the dependence of these parity-mixing coefficients on the electric field strength is shown in Fig. 2.5. The hexapole voltage is set to focus the OH molecules in the state $\Omega = 3/2$, $J = 3/2$, $M_J = 3/2$, f into the crossing region of the secondary beam.

The electric force due to Stark interaction that is experienced by an OH molecule flying along the hexapole at a radial position r with respect to the hexapole axis is given by [48]:

$$\vec{F} = \mp\left[\left(\frac{\Delta_0}{2}\right)^2 + \left(\frac{3\mu\, VM_J\widetilde{\Omega} r^2}{J(J+1)r_0^3}\right)^2\right]^{-1/2} \cdot \left(\frac{\mu\, M_J\widetilde{\Omega}}{J(J+1)}\right)^2 \cdot 18\,V^2\,\frac{r^3}{r_0^6}\cdot\vec{r}, \tag{2.18}$$

in which:

$$\widetilde{\Omega} = \frac{3}{2}\left(C_{3/2,3/2}\right)^2 + \frac{1}{2}\left(C_{1/2,1/2}\right)^2, \tag{2.19}$$

due to the intermediate Hund's case, and 2V is the voltage difference between the adjacent rods of the hexapole. In Eq. (2.18) the plus sign is for the case of the lower Λ-doublet component (e states) and the minus sign for the f states.

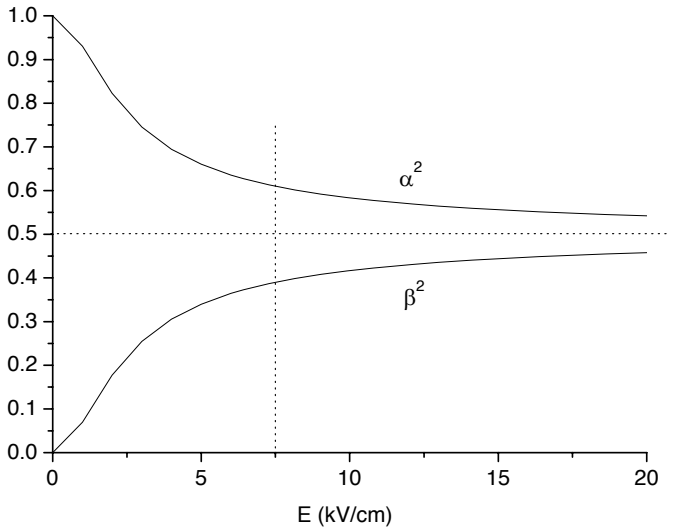

Fig. 2.5: *Squares of the parity mixing coefficients for OH $X^2\Pi_{3/2}$, $J = 3/2$, $M_J\cdot\Omega = -9/4$, as function of the external field strength. The value of these squares at the very high field limit and the electric field intensity used in the experiment for the orientation of the molecules (paragraph 2.3) are indicated with dotted lines.*

The direction of the force shows that only the molecules in the f states can be focused by the hexapole. At the high electric field limit the force exerted on these molecules is harmonic. The molecules in the lower Λ-doublet states are removed from the molecular beam. Simulated trajectories of the OH molecules along the hexapole [66] are presented in Fig. 2.6. As a result, the distribution of the hydroxyl radical population in the collision region is: 93% in the Ω = 3/2, J = 3/2, f state, 4% in the Ω = 3/2, J = 5/2, f state and less than 0.5% in each other rotational state. At the exit of the state selector an electric field orients the OH molecules with respect to the collision partner (paragraph 2.1).

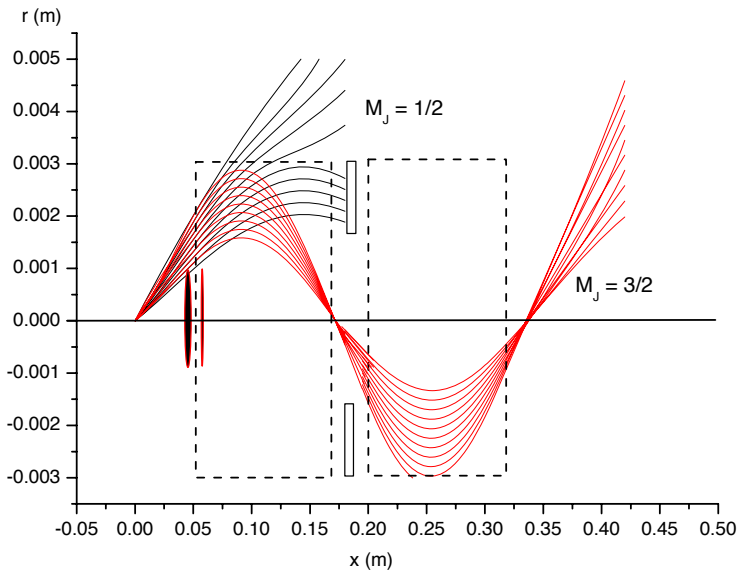

Fig. 2.6: *Simulated [66] trajectories of the OH molecules, $X\,^2\Pi_{3/2}$, J = 3/2, f, M_J =1/2 and 3/2, flying with a mean velocity of 800 m/s, from the 0.2 mm diameter nozzle (x = 0), along the double hexapole, with a voltage of alternately 23 and 0 kV on the rods. A 2 mm diameter beam-stop (x = 0.04) blocks the molecules moving along the horizontal axis. In between the two parts of the hexapole (x = 0.185), a diaphragm with a diameter of 3.5 mm blocks a large part of the molecules from other states than Ω = 3/2, J = 3/2, f, M_J = 3/2. The geometry and voltage are set such that the second focus of the molecules selected is located in the collision and detection volume (x = 0.36).*

A measure of the orientation can be given by the average cosine of θ, the angle made by the permanent dipole moment direction (molecular axis) and the external electric field direction (space fixed axis) [48]:

$$\langle \cos\theta \rangle = \int_{\theta}\int_{\varphi} \psi^{*}_{\varepsilon} \cos\theta \; \psi_{\varepsilon} \sin\theta \, d\theta \; d\varphi$$
$$= \mp 2\alpha\beta \frac{|M_J|}{J(J+1)} \left[\frac{3}{2} (C_{\Omega,3/2})^2 + \frac{1}{2} (C_{\Omega,1/2})^2 \right], \tag{2.20}$$

with Ω = 3/2 or 1/2 for the two spin-orbit components and the minus or plus sign for the states which have f or e symmetry in the absence of the electric field, respectively.
The spin-orbit mixing coefficients, $C_{\Omega, 3/2}$ and $C_{\Omega, 1/2}$, depend on the quantum number of the angular momentum, J, on the molecular rotational constant, B, and the spin-orbit constant, A. The average orientation angle is different for each set of parameters: (E, Ω, J, M_J). For the selected state Ω= 3/2, J = 3/2, f, M_J = 3/2 at the value E = 7.5 k V/cm of the electric field strength used for the orientation, we obtain <cosθ> = -0.55 and θ = 123° [63], while the maximum orientation at high field is $\langle\cos\theta\rangle_{E\to\infty}$ = -0.57. At this field strength the square of the parity mixing coefficients has been calculated via Eqs. (2.17) to be: $\alpha^2 = 0.61$ and $\beta^2 = 0.39$ [63], indicating that the parity mixing is still moderate.

2.4 Determination of the state-to-state cross-sections and steric asymmetries

Prior to the collision the OH molecules are selected in one particular internal state, the relative state-to-state cross-sections can be thus derived directly from the observed LIF intensities. In order to correct for the different degeneracy factors of the initial and final states, the fluorescence signal was divided by the excitation rate [67]:

$$ER = \frac{(2J'_{main}+1) + (2J'_{sat}+1)}{(2J'_{main}+1) + (2J'_{sat}+1) + (2J''+1)}, \tag{2.21}$$

where the labels *main* and *sat* refer to the main lines or the satellite spectroscopic lines excited together within the laser bandwidth, respectively, J' and J'' designate the total angular momentum quantum number for the fluorescent excited state and the ground state, respectively. In the absence of absolute calculated cross-sections the relative state-to-state inelastic cross-sections for the transitions (Ω', J', ε') ← (Ω'', J'', ε'') have been determined using the following formula:

$$\sigma_{rel}(\Omega',J',\varepsilon') = \frac{F_{in}(\Omega',J',\varepsilon')}{F_{out}(\Omega'',J'',\varepsilon'')} \cdot 100(\%), \qquad (2.22)$$

where F_{in} and F_{out} represent the measured in- and out-scattering fluorescence yields:

$$F_{in}(\Omega',J',\varepsilon') \propto \int_{Det\,Vol} \sigma(\Omega',J',\varepsilon' \leftarrow \Omega'',J'',\varepsilon'') \cdot v_{relative} \cdot n_{OH} \cdot n_Y \cdot dV, \qquad (2.23a)$$

$$F_{out}(\Omega'',J'',\varepsilon'') \propto \int_{Outside\ Det\,Vol} \sigma_{el}(\Omega'',J'',\varepsilon'') \cdot v_{relative} \cdot n_{OH} \cdot n_Y \cdot dV + \qquad (2.23b)$$

$$+ \int_{All\ space} \left[\sum_{\Omega',J',\in'} \sigma(\Omega',J',\varepsilon' \leftarrow \Omega'',J'',\varepsilon,) + \sigma_{reactive} \right] \cdot v_{relative} \cdot n_{OH} \cdot n_Y \cdot dV,$$

where n is the number density, $v_{relative}$ is the average relative velocity of the molecular beams, σ_{el}, σ, $\sigma_{reactive}$ are the absolute elastic, inelastic and reactive cross-section, respectively, and Y holds for the collision partner: HCl, HBr, HI and Xe. In these expressions it is assumed that before the collisions take place all OH molecules are in the initial state (Ω", J", ε"). The intersection of the laser beam and scattered OH molecular beam forms the detection volume. The larger the detection volume, the smaller the contribution of the elastically scattered molecules to the out-scattering signal (2.23b). Relative state-to-state cross-sections of OH molecules in the $^2\Pi_{3/2}$, v = 0, J = 3/2, M_J = 3/2, f state have been determined for transitions up to $^2\Pi_{3/2}$, v = 0, J = 9/2 or 11/2 and $^2\Pi_{1/2}$, v = 0, J = 5/2 or 7/2 states by collisions with HCl at 920 cm^{-1} collision energy, with HBr at 750 cm^{-1}, with HI at 690 cm^{-1} and with Xe at 630 cm^{-1} collision energy. The out-scattering signal, F_{out} (Ω", J",∈"), in the denominator of Eq. (2.22), is the same for all the final states probed, but can differ from system to system. For comparison of the OH-Y systems, the relative cross-sections have been divided by the relative cross-section for the scattering to one particular state, as chosen, Ω'= 3/2, J'= 3/2, e. The product $v_{relative} \cdot n_{OH} \cdot n_Y$ can be assumed constant over the entire detection volume. For measurements of the steric asymmetries an orientation field is created in the collision region by four parallel rods biased in pairs in order to induce an electrostatic field parallel or anti parallel to the relative velocity vector of the molecular beams. The polarization of the laser beam has been set to maximize the fluorescence yield in the presence of the electric field, which corresponds to a laser polarization at an angle different from 0 or 90˚ with respect to the electric field. Consequently, both $\Delta M_J = 0$ and $\Delta M_J = \pm 1$ transitions are excited and saturated, therefore allowing to compare the populations of the rotational states probed.

The state-to-state steric asymmetries used to quantify the orientation effect on the scattering process are defined as:

$$S(\Omega', J', \varepsilon') = 100 \cdot \left(\frac{\sigma_{HO-Y} - \sigma_{OH-Y}}{\sigma_{HO-Y} + \sigma_{OH-Y}} \right)_{\Omega', J', \varepsilon'} \quad \%, \tag{2.24}$$

where $\sigma_{HO\text{-}Y}$ and $\sigma_{OH\text{-}Y}$ represent the state-to-state cross-sections for the scattering of the OH molecules oriented towards the collision partner with the O or the H-side, respectively. A positive steric asymmetry indicates the preference for scattering at the O-side and alternatively, an H-side preference corresponds to a negative value of the steric asymmetry.

When using laser-induced fluorescence to deduce the state-to-state cross-sections the question of the density-to-flux transformation arises [68]. With $N_{\Omega, J, \varepsilon}$ the number of OH molecules in the (Ω, J, ε) state and n_Y the number density of the OH collision partner, Y, the rate of OH molecules that are present in the detection volume and scattered out of the initially populated state (Ω"= 3/2, J" = 3/2, ε"= f) into each probed final state (Ω', J', ε') is given by [69]:

$$\frac{dN_{\Omega', J', \varepsilon'}}{dt} = \sigma(\Omega', J', \varepsilon' \leftarrow 3/2, 3/2, f) \cdot v_{relative} \cdot N_{3/2, 3/2, f} \cdot n_Y - \left[\frac{(dN_{\Omega', J', \varepsilon'})_{out}}{dt} - \frac{(dN_{\Omega', J', \varepsilon'})_{in}}{dt} \right], \tag{2.25}$$

where the first term accounts for the production of molecules in the final state by the inelastic scattering process, while the second term, in the parenthesis, accounts for the rate of the net loss of scattered molecules outside the detection volume (difference between the rate of scattered molecules which exit the detection volume and the rate of scattered molecules which enter the detection volume).

As shown in Figs. 2.7 and 2.8 the experimental geometry allows symmetry of the scattering along the OH beam axis with respect to the center of the detection volume. The contribution of the scattered OH molecules which enter the detection volume at its left side is balanced by the contribution of the scattered OH molecules which exit the detection volume at the right side and the reverse. In the limit of a large detection volume the second term in the Eq (2.25) accounting for the net losses can be neglected and the fluorescence signal is proportional to the rate of production of molecules by the inelastic scattering process, as approximated in Eqs. (2.23).

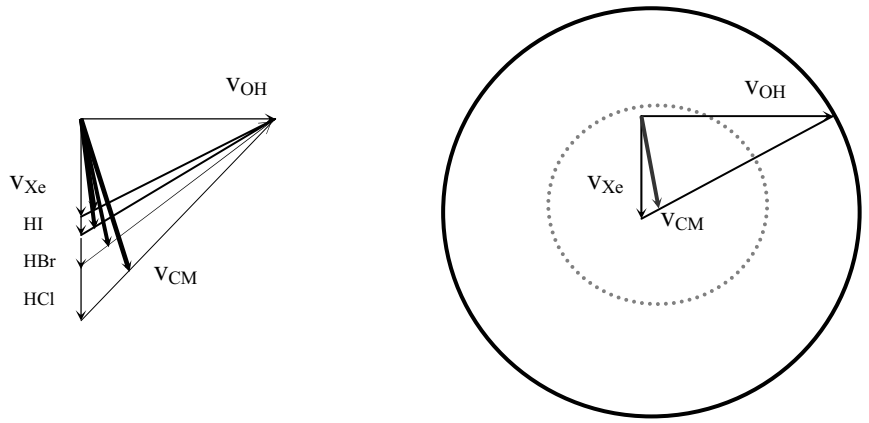

(a) **(b)**

Fig. 2.7 *Velocity diagrams comprising:* ***(a)*** *the laboratory velocities of the OH and Y (Y = Xe, HI, HBr and HCl) prior to the collision (v_{OH} and v_Y -thin arrows), the center of mass velocities for the OH-Y systems - thick arrows and* ***(b)*** *the velocity Newton diagrams for OH-Xe. The bold circle represents the projection on the scattering plane of the velocity Newton sphere for the scattered OH molecules in the lowest internal state (Ω'= 3/2, J'= 3/2, e). The dotted circle represents the projection on the scattering plane of the velocity Newton sphere for the OH molecules which by scattering with Xe are excited to the highest internal state probed (Ω'= 3/2, J'= 9/2).*

However, for a time of the scattering process long relative to the detection time, the LIF measurements probe the steady state number density of the products [69]. In such conditions the total rate in Eq. (2.25) is zero (the loss and the production rates equilibrate) and Eq. (2.25) becomes:

$$\sigma(\Omega', J', \varepsilon' \leftarrow 3/2, 3/2, f) \cdot v_{relative} \cdot N_{3/2,\,3/2,\,f} \cdot n_Y = \oint_{\text{Det Vol}} n_{\Omega',J',\varepsilon'}(\vec{r}) \cdot \vec{v}'_{\Omega',J',\varepsilon'} \cdot d\vec{A}, \qquad (2.26)$$

where v' designates the velocity of the scattered OH molecule in the laboratory frame and the integration is over the total surface enclosing the detection volume.
The laboratory velocity of the OH molecules which by collision change their internal energy with ΔE (Ω', J', ε') is given by:

$$\vec{v}'_{\Omega',J',\varepsilon'} = \vec{v}_{CM} + \vec{u}_{rel}(\Omega', J', \varepsilon') =$$

$$= \frac{m_{OH} \cdot \vec{v}_{OH} + m_Y \cdot \vec{v}_Y}{m_{OH} + m_Y} + \vec{e} \cdot \left(\frac{m_Y}{m_{OH} + m_Y} \cdot \sqrt{2 \frac{E_{coll} - \Delta E(\Omega', J', \varepsilon')}{\mu}} \right), \tag{2.27}$$

where $\vec{v}_{CM}$ and $\vec{u}_{rel}$ are the center of mass velocity and the relative velocity in the center of mass frame, respectively, $\mu = m_{OH} \cdot m_Y/(m_{OH} + m_Y)$ is the reduced mass, $\vec{e}$ is the normalized vector which indicates the velocity angular distribution of the scattered molecule in the center of mass frame, $\vec{v}_{OH}$ and $\vec{v}_Y$ are the velocities of OH and Y before the collision. The distribution of the number density of scattered molecules may be assumed homogeneous over the entire detection volume, thus Eq. (2.26) becomes:

$$n_{\Omega',J',\varepsilon'} = \frac{\sigma(\Omega', J', \varepsilon' \leftarrow 3/2, 3/2\, f) \cdot v_{relative} \cdot N_{3/2,3/2,f} \cdot n_Y}{\oint_{Det\ Vol} \vec{v}'_{\Omega',J',\varepsilon'} \cdot d\vec{A}}. \tag{2.28}$$

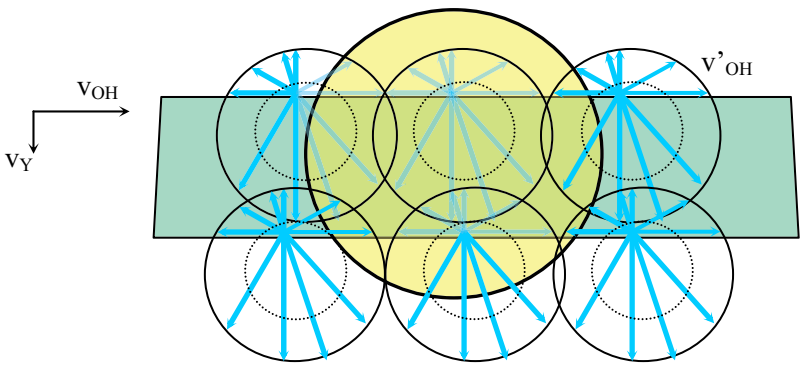

Fig. 2.8 *Drawing of the projections on the scattering plane of the cylindrical volumes of the molecular scattering (rectangle ~ 9 mm length, 2 mm diameter) and of the detection (bold circle ~ 4 mm diameter). The laboratory axes orientations are the same as in the Fig. 2.6 as well as a few projections of the velocity Newton spheres enveloping the laboratory velocities, v', of the scattered OH molecules.*

The number density of the molecules in the final state (Ω', J', ε') and thus the fluorescence signal are inversely proportional to the flux through the detection volume. Consequently, the scattering products with small laboratory velocities are detected more efficiently than those with large laboratory velocities [69]. The ratios of the fluorescence signal measured for each final state and the fluorescence signal measured for the (conventionally chosen) Ω'= 3/2, J'= 3/2, ε'= e final state:

$$\rho(\Omega',J',\varepsilon') = \frac{F_{in}(\Omega',J',\varepsilon')}{F_{in}(3/2,3/2,e)} = \frac{n_{\Omega',J',\varepsilon'}}{n_{3/2,3/2,\,e}}, \tag{2.29}$$

are correlated to the ratios of the absolute state-to-state cross-sections:

$$\frac{\sigma(\Omega',J',\varepsilon' \leftarrow 3/2,3/2,f)}{\sigma(3/2,\,3/2,\,e \leftarrow 3/2,3/2,f)} = \rho(\Omega',J',\varepsilon') \cdot C(\Omega',J',\varepsilon'), \tag{2.30a}$$

with

$$C(\Omega',J',\varepsilon') = \frac{\oint_{\text{Det Vol}} \vec{v}'_{\Omega',J',\varepsilon'} \cdot d\vec{A}}{\oint_{\text{Det Vol}} \vec{v}'_{3/2,\,3/2,\,e} \cdot d\vec{A}}. \tag{2.30b}$$

For the evaluation of the C (Ω', J', ε') factor, which by multiplication transforms the experimental ratio ρ into a ratio of absolute cross-sections, the angular distribution of the scattered OH molecules is needed. This requires knowledge of the differential cross-sections, which are unknown for the systems under study. In order to estimate the effect of the flux-to-density transformation, i.e. the size of the C (Ω', J', ε') factor, we considered two extreme situations:

a) largest possible anisotropy of the velocity angular distribution:

- v'= maximum for all molecules scattered into the lowest final internal state, Ω'= 3/2, J'= 3/2, ε'= e, i.e. $\vec{u}_{rel} \| \vec{v}_{CM}$, and
- v'= minimum for the molecules scattered into all excited final internal states, i.e. $\vec{u}_{rel} \| -\vec{v}_{CM}$.

From Eqs. (2.27) and (2.30b) the expression for the C factors becomes:

$$C_{aniso}(\Omega',J',\varepsilon') = \frac{v_{CM} - \frac{m_Y}{m_{OH}+m_Y}\left(2\frac{E_{coll}-\Delta E(\Omega',J',\varepsilon')}{\mu}\right)^{1/2}}{v_{CM} + \frac{m_Y}{m_{OH}+m_Y}\left(2\frac{E_{coll}}{\mu}\right)^{1/2}}. \tag{2.31}$$

b) fully isotropic velocity angular distribution:

$$1 \geq C_{iso}(\Omega',J',\varepsilon') \geq C_{iso\ min}(\Omega',J',\varepsilon') \equiv \left(\frac{E_{coll} - \Delta E(\Omega',J',\varepsilon')}{E_{coll}} \right)^{1/2}. \qquad (2.32)$$

For both extreme cases we calculated the C factors corresponding to the OH-Ar system, for which both experimental and theoretical state-to-state cross sections are available. Figure 2.9 shows for comparison the experimental ratios ρ [43], the same ratios multiplied with the factors $C_{iso\ min}$ and C_{aniso}, and the ratios of the theoretical cross-sections [45] corresponding to each final internal state probed for OH molecules scattered by Ar. As expected, by taking into account the $C_{iso\ min}$ factors the ratios decrease.

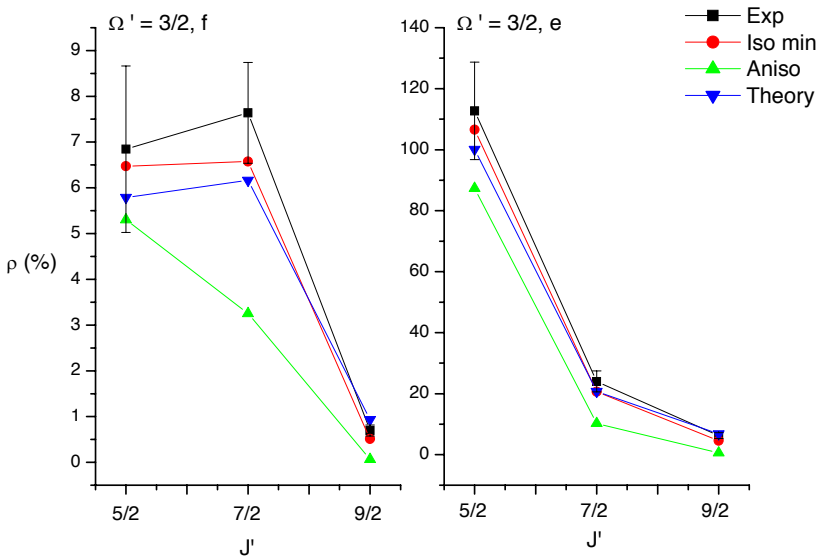

Fig. 2.9 *Ratios of the cross-sections for the OH (Ω', J', ε')←(Ω"= 3/2, J"= 3/2, ε"= f) transitions to the cross-section for the Λ-doublet transition (Ω'= 3/2, J' =3/2, ε'= e) in collisions with Ar at 746 cm^{-1} collision energy. The designation of symbols is as follows: squares for the experimental values, circles and triangles for the experimental values multiplied with the $C_{iso\ min}$ and the C_{aniso} factors, respectively, and upside down triangles for the theoretical ratios. The experimental errors are only given for the uncorrected experimental values.*

In general, the decrease of the experimental ratios by the multiplication with $C_{iso\ min}$ is within the experimental error, indicating that for an isotropic angular distribution of the velocity of the scattered OH molecules a flux-to-density correction is not significant at the present experimental accuracy. In fact, for the spin-orbit conserving transitions the agreement with theory becomes better. An extreme anisotropy of the velocity angular distribution would result in larger corrections for the experimental results and larger deviations with the theoretical values. However, such a distribution is highly improbable. Similar considerations hold for all the systems studied in this work, for which the experimental accuracies are comparable or lower than for the OH-Ar system. Therefore we decided not to take into account the flux-to-density transformation.

2.5 Characterization of the secondary beam

2.5.1 Formation of the secondary beam

The secondary molecular beam refers to the collision partner for the hydroxyl radical: HCl, HBr, HI or Xe. This beam is formed in a vacuum chamber separated from the collision chamber by a skimmer with an orifice of 3 mm in diameter. Similar to the primary beam the beam source is a pulsed supersonic valve (Jordan C-211) operating at 10 Hz. The pulse duration is about 50 μs (FWHM). The valve nozzle with a diameter of 0.5 mm is positioned 30 mm from the skimmer and about 90 mm from the collision center.

Considering the mean transversal beam spread the diameter of the secondary beam at the scattering center is 4-5 times larger than the size of the focused OH beam. For the inelastic collision experiments the backing pressure of the secondary beam gas has been chosen such that the collision induced decrease of the OH initial is not more than 10%, which assures the single collision regime. For the detection of the reaction products different mixtures of the secondary beam gas with rare gases have been used as well in order to vary the collision energy. Some relevant properties of the secondary molecular beam are listed in Table 2.2 for the various scattering gases studied.

2.5.2 Resonance enhanced multiphoton ionization

Most applied methods to detect atoms and molecules involve ionization. Once charged, the particles can be very efficiently collected and separated by their masses or velocities. For atoms and diatomic systems one-photon-absorption ionization requires vacuum-ultra-violet (VUV) or extreme-ultra-violet (XUV) radiation [71].

Table 2.2: *Properties of the secondary beam for the various scattering gases studied: the mass, ionization potential, dissociation energy, the rotational constant for the ground vibration and electronic state, the equilibrium inter-atomic distance, the estimated laboratory velocity and collision energy, the rotational temperature, the electric dipole and quadrupole momenta and the polarizability.*

Molecular property	HCl	HBr	HI	Xe
I.P. (eV)	12.74	11.67	10.38	12.13
D_0 (eV)	4.44	3.76	3.05	-
Electronic ground-state	$^1\Sigma^+$	$^1\Sigma^+$	$^1\Sigma^+$	$^1S_0$
B_0 (cm^{-1})	10.48	8.35	1.61	-
r_e (Å)	1.27	1.41	1.61	-
v (m/s)	1070 ± 150	707 ± 100	565 ± 80	470 ± 70
$\mu = \frac{m_{OH} \cdot m_Y}{m_{OH} + m_Y}$	11.60	14.05	15.01	15.05
$E_{coll\ OH\text{-}Y}$ (cm^{-1})	920 ± 250	750 ± 190	690 ± 190	630 ± 140
T_{rot} (K)	20 ± 5	19 ± 3	17 ± 4	-
Dipole[a] (D)	1.08	0.82	0.38	0
Quadrupole[b] (DÅ)	3.8	4	6	0
Polarizability[c] ($Å^3$)	3.2	4.5	6.7	4

[a] *experimental values [70]*
[b] *calculated zz diagonal-term of the electric quadrupole moment tensor [70]*
[c] *calculated diagonal-terms average of the polarizability tensor [70]*

With ultra-violet (UV) radiation a multi-photon absorption process will be needed to reach the continuum of the internal state of the ion.The high photon fluxes of pulsed UV lasers can compensate for the low values of the multi-photon absorption cross-sections.

Competing processes, such as predissociation, fluorescence, collision quenching or other decay mechanisms lead to a smaller ion yield. However, these losses are small for atoms and small molecules in molecular beams. Generally, for an n-photon-transition the transition rate (s^{-1}) is predicted to be [71]:

$$\frac{dN}{dt} = \sigma_n I^n, \tag{2.33}$$

where I is the laser flux, expressed in photons·m^{-2}·s^{-1}, and σ_n is the n-photon absorption cross-section with the unit $m^{2n}s^{n-1}$.

If the system has to absorb at least two photons to be ionized and one of the intermediate absorption steps involves the resonant excitation of the molecule/atom to a stable electronic state, the ionization cross-section increases considerably. This process is called Resonance Enhanced Multiphoton Ionization (REMPI) [71, 72-74]. Two of such ionization methods are employed in this study for the characterization of the secondary beam and for the detection of reaction products: (2+1) and (1+1') REMPI, as schematically shown in Fig. 2.10. For the resonant ionization methods the dependence of the transition rate on the laser flux given in Eq. (2.33) becomes empirically I^m, for which m usually is not an integer and is smaller than the number of photons absorbed, n.

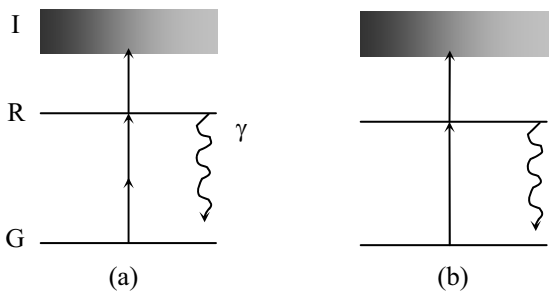

Fig. 2.10: *Ionization by multiphoton absorption for: (a) (2+1) and (b) (1+1') REMPI. The horizontal lines designate energy levels for bound states: G-ground state and R-resonant intermediate state, while the bands mark the continuum I of the ion. At the resonant level R the absorption leading to ionization may compete with decay via various mechanisms, at a decay rate γ.*

At very high laser fluencies the excitation or the ionization step may become saturated in the sense that the rate of the saturated step does not increase any further with the laser flux and reaches its maximum value.

Assuming that all molecules that decay return to the ground state, the rate equations for the three-level system shown in Fig. 2.10 are given by [71, 74, 75]:

$$\frac{dN_G}{dt} = -\sigma_{GR} I^2 (N_G - N_R)$$

$$\frac{dN_R}{dt} = \sigma_{GR} I^2 (N_G - N_R) - \sigma_{RI} I N_R - \gamma N_R \qquad (2.34)$$

$$\frac{dN_I}{dt} = \sigma_{RI} I N_R ,$$

with N the number density of molecules in the ground (G), resonant (R) or ion continuum (I) states, σ_{GR} the two-photon absorption cross-section for the excitation step, σ_{RI} the one-photon absorption cross-section for the ionization step and γ the rate of the decay from the resonant state.

For laser pulse duration $T << 1/\gamma$ and saturation of the excitation step, Eqs. (2.34) lead to: $N_I \propto \sigma_{RI} \cdot I$, while in case of saturation of the ionization step Eqs. (2.34) result in: $N_I \propto \sigma_{GR} \cdot I^2$. However, various effects of the laser beam focusing and profile may blur the expected dependence of the ion signal on the laser power. Electrostatic lenses using the velocity-map imaging configuration [76] are employed to collect the ions on the detector. The geometry of the electrostatic lenses and the voltages used determine the mass and/or velocity resolution [76]. The ions are detected by two micro-channel plates coupled to a phosphor screen and CCD camera.

2.5.3 REMPI spectra of HCl, HBr and HI

The halogen hydride photochemistry varies strongly with the atomic number of the halogen. The spin-orbit interaction of the halogen atom becomes stronger with increasing atomic number. The spin-orbit splitting of the energy levels of the ground state is 881 cm^{-1} for Cl, 3685 cm^{-1} for Br and 7603 cm^{-1} for I [77]. UV and VUV photodissociation studies of HX (X = F, Cl, Br, I) [78-83] indicate the presence of three purely dissociative states involved in the fragmentation: the A $^1\Pi_1$ and the a $^3\Pi_1$ states, which correlate adiabatically with the formation of ground state atoms H (^2S) and X ($^2P_{3/2}$), and the a $^3\Pi_0$ state that correlates with the H (^2S) + X*($^2P_{1/2}$) fragments.

For Hydrogen Chloride the spin-conserving transitions are favored and only the A $^1\Pi_1$ state is populated after the absorption of one photon. However, for Hydrogen Bromide (Fig. 2.11) and Iodide, with a much stronger spin-orbit interaction, the a $^3\Pi$ states are predominantly involved. Broad absorption bands peak around 155 nm, 175 nm and 220 nm for HCl, HBr and HI, respectively, and fade away at 277 nm for HCl, at 327 nm for HBr and at 401 nm for HI [84].

In Figs. 2.12, 2.13 and 2.14 REMPI spectra of HCl, HBr and HI are shown. The spectra were obtained using a laser system consisting of the frequency doubled dye-laser (Lambda Physik ScanMate), pumped by a 10 Hz repetition rate, ~10 ns pulse, Nd: YAG laser (Continuum Powerlite). The UV radiation of 1- 2 mJ/pulse is focused with a lens of 15 cm focal length. For the HBr ion detection the focusing is weaker. The atomic lines for the ground and first excited state Br are indicated as sticks below the spectrum showing at what excitation wavelengths the Br and HBr transitions overlap. The assignment is based on the spectral analysis of Callaghan and Gordon [85].

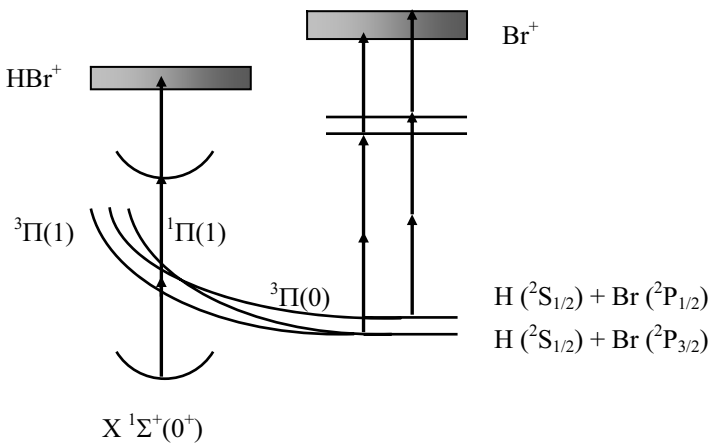

Fig. 2.11: *Scheme of ionization of HBr X $^1\Sigma^+(0^+)$ and Br by (2+1) REMPI. The three dissociative states of HBr are reached by one-photon absorption, after which the dissociation and the further excitation compete. A process involving 3 UV photons lead to the parent ion formation, while 4 photons absorption give birth to the fragment ions H($^2S_{1/2}$)and Br ($^2P_{3/2}$) or Br* ($^2P_{1/2}$).*

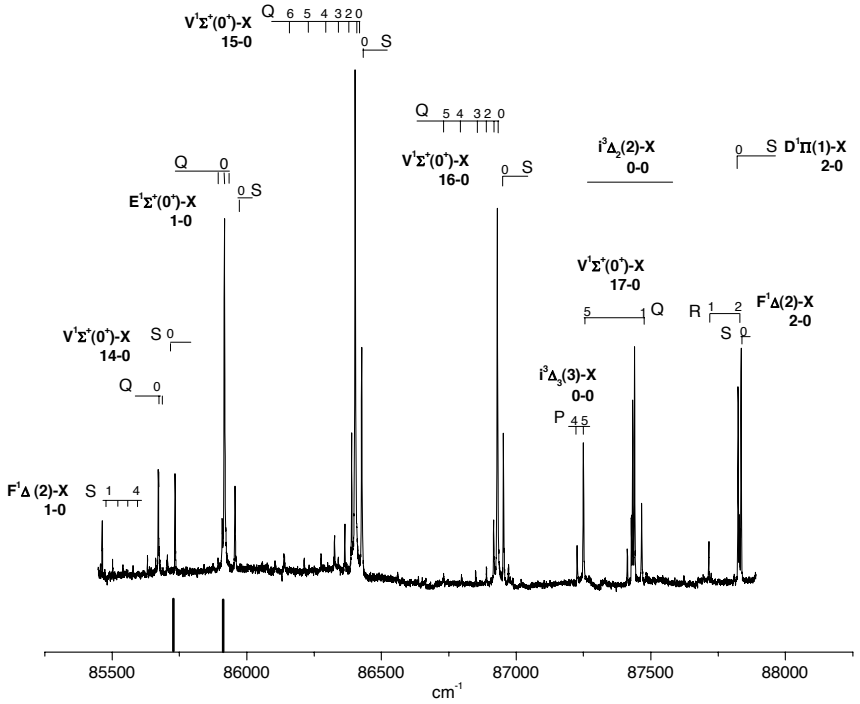

Fig. 2.12 *(2+1) REMPI spectrum of HCl. The stick spectrum gives the wavelengths for the atomic Chlorine lines.*

2.5.4 Rotational population distribution

For the derivation of the rotational temperature of the secondary beam (2+1) or (1+1') REMPI spectra have been used. In the absence of alignment and laser power saturation effects the ion signal, I, is given by [80-83]:

$$I = \frac{C \cdot P(v'', J'') \cdot q(v'', v') \cdot S(J'', J')}{2J''+1}, \qquad (2.35)$$

where J" and v" are the total angular momentum and vibration quantum numbers of the ground electronic state, J' and v' are the corresponding quantum numbers for the resonant

intermediate state, q is the Frank-Condon factor, S is the two-photon rotational line strength, C is a constant depending on the detector efficiency and laser intensity, and P is the population of the ground state rotational levels given by the Boltzmann distribution, which assumes thermodynamic equilibrium:

$$P(v'',J'') = \frac{(2J''+1)\cdot e^{-\frac{E(v'',J'')-E(v'',0)}{kT}}}{Q_{v''}(T)}, \tag{2.36}$$

$$Q_{v''}(T) = \sum_{J}(2J+1)\cdot e^{-\frac{E(v'',J)-E(v'',0)}{kT}} = 1/N_0. \tag{2.37}$$

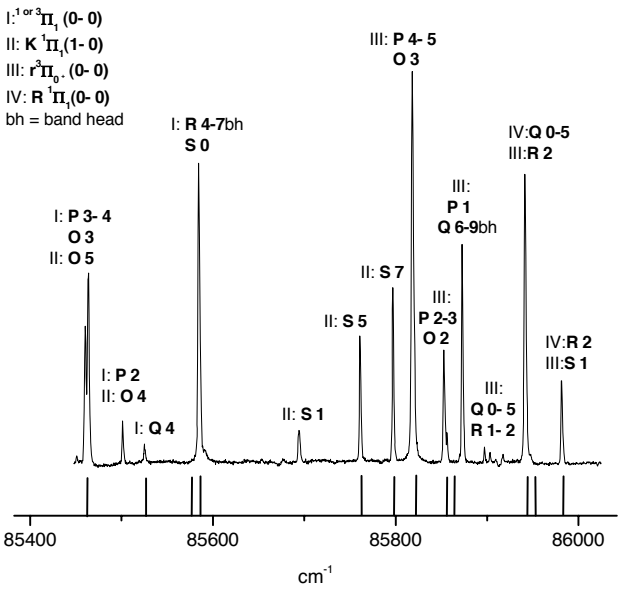

Fig. 2.13 *(2+1) REMPI spectrum of HBr. The stick spectrum gives the wavelengths for the atomic Bromine lines*.

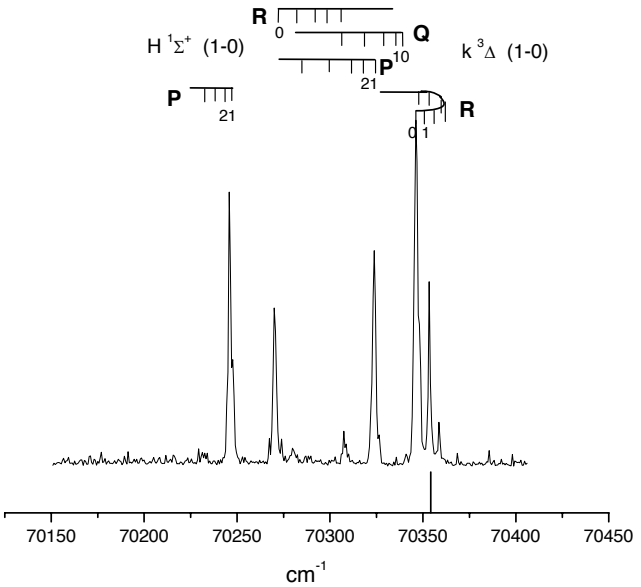

Fig. 2.14 *(1+1') REMPI spectrum of HI. The stick spectrum gives the wavelengths for the atomic Iodine lines.*

In these expressions E (v, J) ≈ E (v, 0) + $B_v \cdot J \cdot (J+1)$ is the rotational energy of a rigid rotor, N_0 represents the population of the ground rotational level (J = 0) and T is the rotational temperature describing the population distribution. The rotational temperature for this rigid rotor approximation can be obtained by combining the equations (2.35-2.37). In a logarithmic plot:

$$\ln\frac{I}{S} = \ln(CN_0q) - \frac{B_vJ(J+1)}{kT} \tag{2.38}$$

as function of J(J+1), the slope B_v/kT gives the rotational temperature. Here S (J', J") are the Hönl-London line strength factors for the excitation transitions [80, 86]. The relative signal intensities of each rotational line are extracted from the spectra by taking the area under the peaks. Rotation spectra are shown in Figs. 2.15 - 2.17. The average rotational temperatures deduced are 20 ± 5 K, 19 ± 3 K and 17 ± 4 K for HCl, HBr and HI, respectively, at the mentioned backing pressures. For the HBr molecular beam a study of the dependence of the rotational temperature on the backing pressure revealed rotational temperatures of 26 ± 6 K and 15 ± 2 K for 400 mbar and 1750 mbar, respectively.

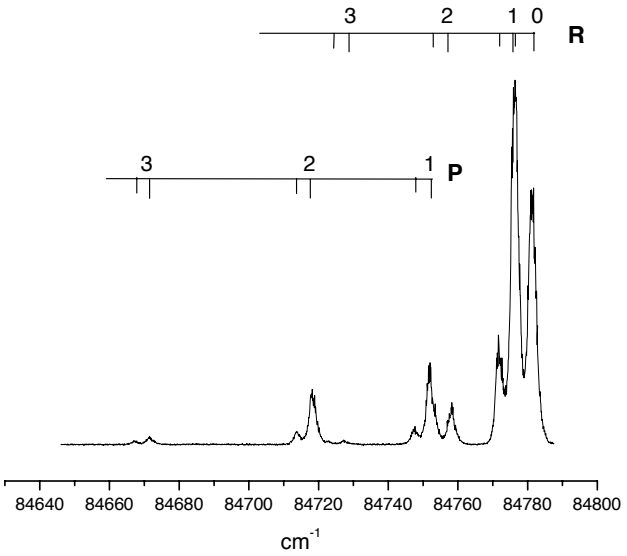

Fig. 2.15 *(1+1') REMPI $V\ ^1\Sigma^+ \leftarrow X\ ^1\Sigma^+$ (12-0) spectrum of pure HCl at 800 mbar backing pressure. The isotope shifts are marked in the plot ($^1H\ ^{35}Cl$ and $^1H\ ^{37}Cl$ have the natural abundances of 77% and 23%, respectively).*

The dependence of the HBr ion signal, S, on the backing pressure, p, for p > 650 mbar, was found:

$$S = k_1 \cdot p + k_2 \cdot p^2 , \tag{2.39}$$

This indicates that dimerization contributes also to the rotational cooling [87]. The concentration of dimers, C, in the beam:

$$C = k_2 \cdot p / k_1 , \tag{2.40}$$

is estimated to (18 ± 5) % at 1 bar stagnation pressure, corresponding to the measurements conditions. It is likely that dimers are present also in the beams of the other halides [88] and as well in the beam of Xe [89]. These weakly bound van der Waals complexes are instable with respect to the collisional dissociation.

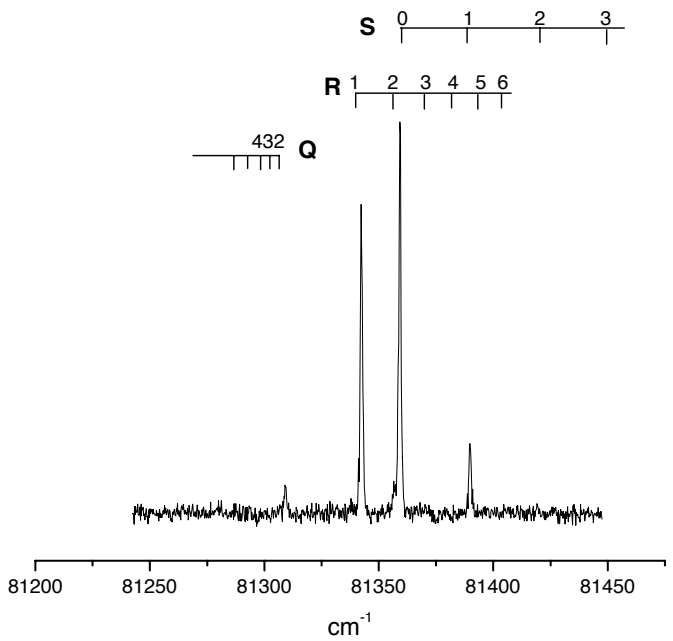

Fig. 2.16 *(2+1) REMPI $I\,^1\Delta\,(2) \leftarrow X\,^1\Sigma^+$, (0-0) spectrum of an expansion of pure HBr at 1 bar backing pressure*

The dipole moments of the ground state $(HCl)_2$ and $(HBr)_2$ are reported to be (1.5 ± 0.1) D [88] and 1.7 D [90], respectively, values that are larger than in the case of the monomer. Therefore, the dimers from the secondary beam may contribute to the long-range dipole-dipole interaction with the OH molecules. The dissociation energy of the HCl dimer measured by Pine et al. [91] is (431 ± 22) cm^{-1}. Latajka et al. [92] found that the binding energies of the dimer complexes decrease in the order HCl > HBr > HI. They have calculated the interaction energies of these HX dimers to be about 570, 480 and 370 cm^{-1}, for X = Cl, Br and I, respectively. The L-shaped equilibrium geometries of the H-X-H'-X' dimers are found to have a X-X' bond length of about 3 times the internuclear distance corresponding to the equilibrium geometry of the monomer. The energy of collision with the OH radical at conditions of our experiments exceeds the binding energy of the dimers for all the systems studied. If these complexes fragment, their short-range interaction with the OH molecules might be similar with the one of the monomer.

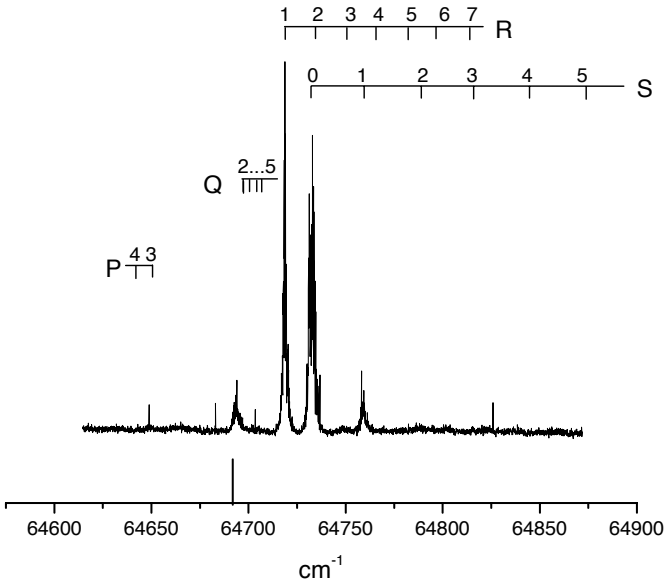

Fig. 2.17 *(2+1) REMPI $f^3\Delta(2) \leftarrow X^1\Sigma^+$ (0,0) spectrum of an expansion of pure HI at 1.1 bar backing pressure. The stick spectrum gives the wavelengths for the atomic Iodine lines.*

The Xe dimer is even more weakly bound. Its electronic ground state is repulsive except for a shallow van der Waals minimum at large internuclear separation, having a depth of 196 cm^{-1} [93]. The 1.3 $Å^3$ [94] polarizability of the dimer is 3 times smaller than the polarizability of the Xe atom, indicating that the dispersion and the long-range interaction with the OH molecule is weaker for the Xe dimer than for the Xe atom.

Chapter 3

Reactive scattering of the OH molecule

3.1 Introduction to reaction dynamics

For two molecular beams with number densities n_1 and n_2 colliding with a relative velocity v_{rel}, the rate of the product formation is given by [95]:

$$\frac{dn_p}{dt} = n_1 \cdot n_2 \cdot v_{rel} \cdot \sigma_{react}, \tag{3.1}$$

where n_p designates the product density. The reaction cross section, σ_{react} (m^2), is a measure of the reaction probability at given conditions. This cross section depends on the nature of the reactants, the collision energy, the internal energy and the relative angle of incidence for the reactants. If the internal energies of the reactants and products are well defined, state-to-state reactive cross sections can be obtained. The product $\sigma_{react} \cdot v_{rel}$ averaged over the relative velocity in case of equilibrium gives the thermal reaction rate k (T) ($m^3 \cdot molec^{-1} \cdot s^{-1}$) that characterizes the reaction at temperature T:

$$k(T) = \int_0^\infty \sigma_{react} \cdot v_{rel} \cdot f(v_{rel}) \cdot dv_{rel}, \tag{3.2}$$

with f (v_{rel}) the probability that the encountering molecules have the relative velocity v_{rel}.

The energy disposal, i.e. the difference between the formation enthalpies of the products and reactants at 0 K, ΔH^0_0, the internal energies and the kinetic energies of both reactants and products are correlated by the total energy balance:

$$(E_{int} + E_{coll})_{reactants} = (E_{int} + E_{coll})_{products} + \Delta H^0_0 . \tag{3.3}$$

Possible transition states with their energy barriers, van-der-Waals complex wells or splitting into multiple channels shape the total potential energy along the reactive coordinates. From reactants to products the system evolves through a variety of configurations, inter-atomic distances and orientations of the constituent atoms or bonds.

3.2 OH reactivity

In the present study we tried to observe the reaction products of the OH-HX scattering processes, with X = Cl, Br or I. These processes are not yet all amenable for a theoretical description, partially because the potential energy surfaces are not well known.

A high reactivity is predicted for the hydroxyl radical with halogen hydrides. The highly exothermic reactions:

$$OH + HCl \rightarrow H_2O + Cl, \quad \Delta H°_0 = -5534\ cm^{-1}, \tag{3.4}$$

$$OH + HBr \rightarrow H_2O + Br, \quad \Delta H°_0 = -10992\ cm^{-1}, \tag{3.5}$$

$$OH + HI \rightarrow H_2O + I, \quad \Delta H°_0 = -16685\ cm^{-1}, \tag{3.6}$$

are important for atmospheric chemistry since they produce halogen atoms that catalyze ozone destruction. As hydrogen atom transfer reactions they constitute a step in computational complexity from atom-diatom to diatom-diatom systems. According to the kinetic and photochemical data given by the IUPAC Subcommittee for Gas Kinetic Data Evaluation [84], the reaction (3.4) has a thermal rate of $(7.8 \pm 0.1)\cdot10^{-19}$ $m^3\cdot molec^{-1}\cdot s^{-1}$ at 298 K and an increase of the rate with the temperature. Conversely, for the reactions (3.5) and (3.6) the thermal rates decrease with an increase in temperature. At 298 K, the rate constants are $(1.1 \pm 0.1)\cdot10^{-17}$ $m^3\cdot molec^{-1}\cdot s^{-1}$ and $(7.0 \pm 0.3)\cdot10^{-17}$ $m^3\cdot molec^{-1}\cdot s^{-1}$, respectively. For the OH + HCl and OH + HBr reactions, barrier heights of around 300 - 900 cm^{-1} [20, 22, 23, 25, 82], and 0 - 300 cm^{-1} [21, 32, 84], respectively, are reported, whereas no barrier at all was found for OH + HI [38, 84].

Using interpolated *ab initio* quantum scattering calculations by extended methods to the rotation bond approximation model, Yu and Nyman [23] obtained for the OH + HCl reaction thermal rate constants in agreement with experimental results. They found an early saddle point and a HOHCl van der Waals complex in the entrance channel, as shown in Fig. 3.1. The corresponding classical barrier height calculated was about 720 cm^{-1} and values for the van der Waals well relative to the reactants and the binding energy of about 1910 cm^{-1} and 1470 cm^{-1}, respectively. According to these calculations, the transition state (TS) has a non-planar geometry with a torsion angle between the HOH and OHCl planes of 52° and with values of 142° and 104° for the <HOH and <HOCl angle, respectively. But the HOHCl complex has a planar geometry with angles of 174° and 113° for <HOH and <HOCl, respectively. The inter-atomic distances relax slightly when going from the TS to the complex. For HCl in the ground vibronic state and OH in the ground rotational state, Yu and Nyman have estimated the reaction cross section for collision energies up to 1450 cm^{-1}.

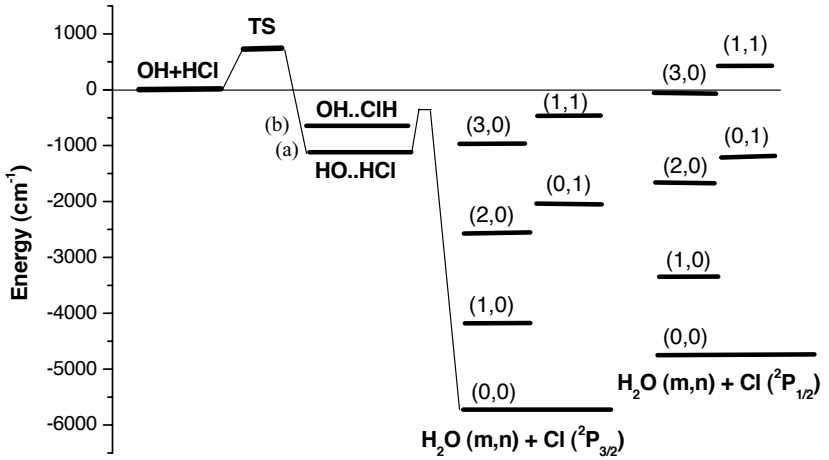

Fig. 3.1 *Energy diagram along the reaction pathway for OH+HCl [23, 26]. The notation for the vibration energy levels of H_2O product, (m,n), designate by m the quantum number for the bending mode and by n the quantum number for the asymmetric and symmetric stretch modes. The labels (a) and (b) refer to Fig. 3.2*

This cross section is predicted to be quite large at low translation energy due to tunneling. The reactive cross section increases significantly with the relative kinetic energy of the colliding molecules, from about $6 \cdot 10^{-22}$ m^2 at 320 cm^{-1} collision energy up to $1.7 \cdot 10^{-20}$ m^2 at 1450 cm^{-1} collision energy. Wormer et al [26] computed for OH-HCl four-dimensional diabatic PES's correlated with the two-fold degenerate $^2\Pi$ ground state of the hydroxyl radical using *ab initio* coupled-cluster and multi-reference configuration interaction methods. In addition to the HO-HCl global minimum with a well depth of 1123 cm^{-1}, they found a local minimum with an energy well of 655 cm^{-1}, for which the molecular configuration is very different. Whereas at the global minimum the HCl molecule is nearly linear with the bond axis, it makes an angle of 87° with the OH radical in the geometry of the local minimum, as shown in Fig. 3.2. For a minimum with a bent (L-shaped) geometry it is expected that, besides the interaction involving the dipole electric moments, the interaction involving the quadrupole electric moments contributes significantly.

The quite large energy disposal is enough to provide the products with internal excitation. If we use the notation H_2O (m, n) with m the quantum number for the bending mode and n the quantum number for the asymmetric and symmetric stretch modes, the states up to (3,0), (0,1) and (1,1) are energetically accessible, as shown in Fig. 3.1.

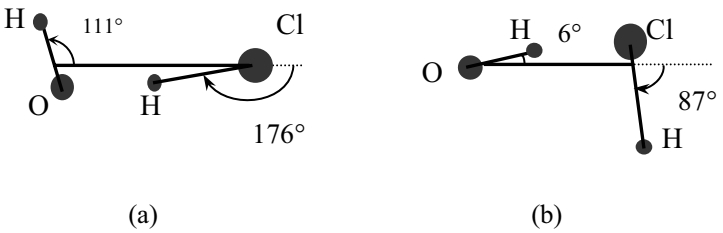

Fig. 3.2 *Structure at the global (a) and local (b) minimum of the lowest adiabatic potential energy surface of OH-HCl [26]*

However, Clary et al. [21] have found that the H_2O molecule will be produced with the highest probability in its ground vibrational state if OH is not rotating and both OH and HCl are not vibrationally excited, as in the case of our experiments. Consequently, the products H_2O and Cl ($^2P_{3/2}$) share a total of about 6450 cm^{-1} kinetic energy and H_2O and Cl ($^2P_{1/2}$) would share about 5570 cm^{-1}. A kinetic energy of 2180 cm^{-1} is estimated for Cl and 1860 cm^{-1} for the Cl* product. The results of Clary et al. were based on the rotating bond approximation model for quantum scattering calculation. The cross section for the reaction of the OH radical in its ground rotational state with HCl in the ground vibration state is predicted about $4 \cdot 10^{-20}$ m^2 for 890 cm^{-1} collision energy for our pure HCl molecular beam experiments and more than two times larger at the energy of 2980 cm^{-1} as obtained in case of 5% HCl seeded in He.

Also for the OH + HBr reaction Clary et al. [21] reported quantum scattering calculations using the rotating bond approximation and treating explicitly the bending vibration and local OH stretching vibration in H_2O as a function of the vibration of HBr and rotation of OH. The authors found a strong dependence of the reaction cross section with the rotational quantum number of the OH molecule. For both reactants in the ground vibrational energy state and the hydroxyl radical in its ground rotational state, the resulting OH + HBr reaction cross section was $2.8 \cdot 10^{-19}$ m^2 at a collision-energy of 730 cm^{-1}. The vibrational distribution of the H_2O product was predicted to be (1,1), (0,2), (2,1), (1,2) in order of decreasing cross sections. These results are in general agreement with the vibrational distribution of the H_2O product measured by IR chemiluminescence by Butkovskaya and Setser [31]. In a direct dynamics study Liu et al. [33] found that the OH + HBr reaction proceeds via a hydrogen bounded complex and subsequently a transition state. An energy barrier of about 310 cm^{-1} was obtained in contrast to Clary et al. [21] and Nizamov et al. [32] who found a potential well instead of a reaction barrier, equal to 602 cm^{-1} and 623 cm^{-1}, respectively.

For OH + HI no calculations of rate constants or reaction cross sections have been reported so far, due to the lack of a PES.

3.3 Detection of the reaction products

In order to observe reaction products REMPI methods combined with time-of-flight (TOF) mass spectrometry were used. Assuming the ionization step saturated, a comparison between the (2+1) and (1+1') REMPI schemes gives:

$$\frac{N_{(2+1)}}{N_{(1+1')}} = \frac{\sigma_2 \cdot I_{(2+1)}^2 \cdot V_{(2+1)}}{\sigma_1 \cdot I_{(1+1')} \cdot V_{(1+1')}}, \tag{3.7}$$

where the subscripts (2+1) and (1+1') are used to label the two REMPI methods, N refers to the ion yield and V designates the detection volume (given by the intersection of the laser beam and the two molecular beams). The notations σ and I are the same as in paragraph 2.5.2. The one-photon absorption cross section, $\sigma_{1,}$ is in the range of $10^{-20} \div 10^{-26}$ m^2 and the two-photon cross section, σ_2, can take a value between 10^{-56} and 10^{-65} m^4s [68]. Focusing the laser beam for the case of (2+1) ionization can compensate for the large difference in order of magnitude of the two cross sections. However, the drawback is a reduction of the detection volume. The (1+1') REMPI scheme does not necessarily require focusing, but two different wavelengths are required, which for the ionization of atoms can be (VUV+UV). Both methods have been applied using schemes as depicted in Fig. 3.3.

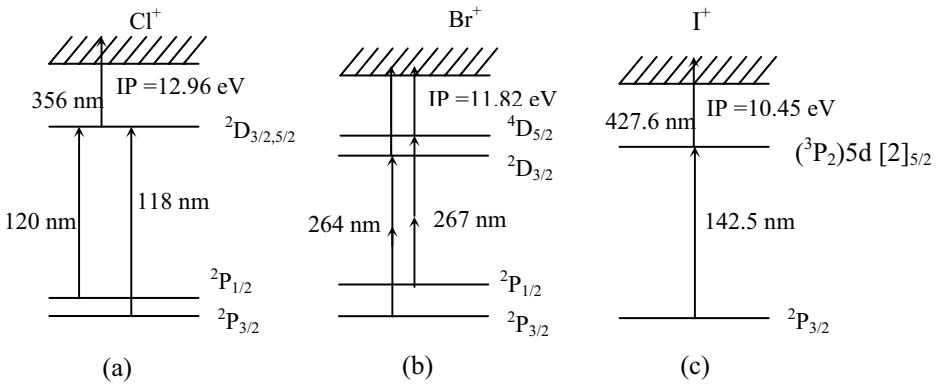

Fig. 3.3 *(2+1) REMPI scheme for the detection of Br (b) and the (VUV + UV) REMPI scheme for the detection of Cl (a) and I (c)*

The detection of the reactive product by similar (1+1') REMPI method was reported by Dong and coworkers [96]. A view of the experimental set-up with REMPI-TOF detection is given in Fig. 3.4

The VUV generation is based on non-resonant third harmonic generation [97-99], a commonly used four wave-mixing method, since it requires only one tunable laser. Using an optically nonlinear medium, coherent visible or near UV radiation can be converted into radiation at a three times shorter wavelength with equivalent coherent properties. If an external electric field of intensity E is applied to a medium, the induced polarization response P can be written as a power series in terms of the applied field strength [97]:

$$P_i = N \cdot (\chi_i^{(1)} \cdot E_i + \sum_{jk} \chi_{ijk}^{(2)} \cdot E_j E_k + \frac{3}{2} \sum_{jkl} \chi_{ijkl}^{(3)} \cdot E_j E_k E_l + ...), \qquad (3.8)$$

where i, j, k and l are Cartesian subscripts x, y or z, $\chi^{(n)}$ is the wavelength dependent n-th order susceptibility and N is the number density of atoms in the medium.

The efficiency of the conversion decreases with the order of the harmonic generation. The generated response depends on the density N of the nonlinear medium, which for frequency tripling is a rare gas or vapor metal such as Hg and Mg [100-103].

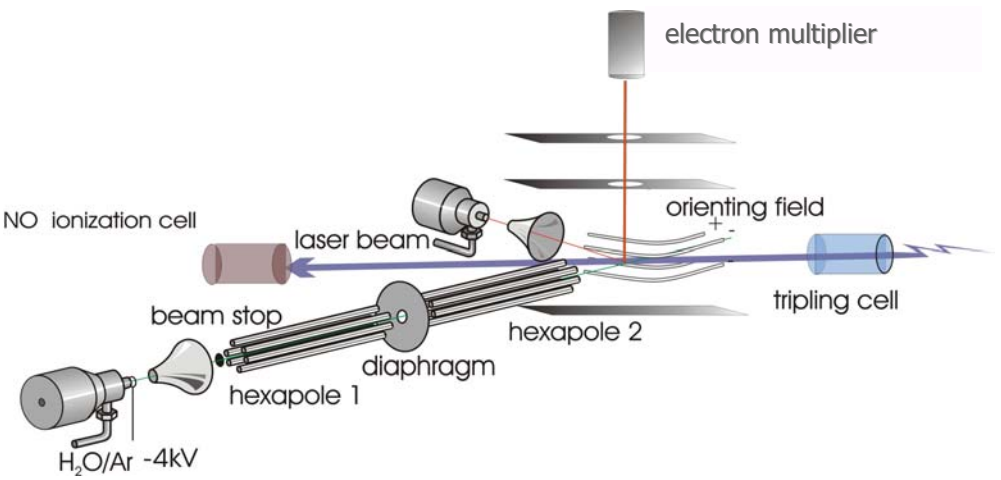

Fig. 3.4 *Drawing of the experimental set-up for the OH + HCl reactive scattering measurements*

Assuming a TEM_{00} mode for the spatial laser profile and tight focusing in the optically nonlinear medium, the third harmonic generation takes place if the wave-vector mismatch, Δk, is negative [97]:

$$\Delta k = k(3\nu) - 3k(\nu) = \frac{2\pi \cdot 3\nu}{c}\left[n(3\nu) - n(\nu)\right] < 0, \tag{3.9}$$

where the wave-number $k(\nu) = 2\pi\nu \cdot n(\nu)/c$, ν is the frequency of the fundamental radiation, n the refractive index of the medium and c the speed of light. Therefore a gas may be employed as frequency tripling medium only in the frequency ranges where it has a negative dispersion: $n(3\nu) < n(\nu)$. For a given geometry of the frequency-tripling set-up the maximum VUV radiation power, $\mathcal{P}$, is a function of the radiation frequency, tripling gas pressure, p, and focal length of the optical system, f :

$$\mathcal{P}_{max}(3\nu) = \mathcal{P}(\nu, p_{optim}, f_{optim}) \tag{3.10}$$

For Xe the negative dispersion spectral regions at 117.6-118.9 nm and 140.4-146.8 nm are used and for Kr the one at 120-123.2 nm. For these rare gases a cylindrical cell with 160 mm length is provided with a 25.4 mm diameter MgF_2 exit window. The transmittance of the 2 mm thick MgF_2 window is expected to be about 45% [104]. The rare gas cell has been mounted at 100 mm from the molecular beams crossing region assuring that the diverging co-propagating VUV and UV laser beams cover the crossing volume of the molecular beams. The third harmonic generation is monitored by the signal collected in a NO (IP = 9.3 eV, $\lambda < 133.3$ nm) ionization cell, used also for the calibration of the VUV radiation flux. The 120 mm long ionization cell contains two coaxial electrodes: a wire kept at negative low voltage surrounded by a cylindrical electrode grounded via a 100 kΩ resistor and connected to a current amplifier via a 10 nF capacitor. For an optimum ion signal collection in the linear ion-photon pair regime, a voltage of –350 V is applied on the inner electrode. The cell is filled with NO at a pressure of 0.13 mbar and the ion signal is amplified via a (Keithley 427) current amplifier. The reported photo-ionization cross section of NO at 118-120 nm of about $1.2 \cdot 10^{-22}$ m^2 [110, 78] is used for the estimation of the tripling conversion efficiency. Lenses with different focal length varying from 40 mm to 500 mm were tried for the focusing of the UV fundamental light in the rare gas cell. The lens can slide in a tube outside the vacuum chamber, such that the position of the focus with respect to the exit cell window was tuned to maximize the VUV output. This function and the optimum parameters are to be determined experimentally. The conditions for the optimal third harmonic generation were met by using a lens of 150 mm focal length, for which the focus was estimated to be at about 5 mm distance from the MgF_2 window.

Maximum VUV powers were obtained (Eq. 3.10) as shown in Fig. 3.5. The maximum VUV yield at 117.6 nm corresponds to an estimated conversion efficiency of $1.5 \cdot 10^{-6}$. For all spectral regions mentioned the efficiency decreases with the wavelength.

Enhanced phase-matching conditions are possible by mixtures of rare gases [98, 101]. The wave vector mismatch defined in the equation (3.9) can be expressed as [102]:

$$\Delta k(\nu) = C(\nu) \cdot N, \tag{3.11}$$

with C, the wave-vector mismatch/atom. For a mixture of Xe and Ar:

$$\Delta k(\nu)_{optimum} \propto C_{Xe}(\nu) \cdot p_{Xe}(\nu) + C_{Ar}(\nu) \cdot p_{Ar}(\nu). \tag{3.12}$$

As a result of the spectral dependences of the Ar and Xe wave-vector mismatches per atom, new phase-matching conditions are built for mixtures with new partial optimum pressures.

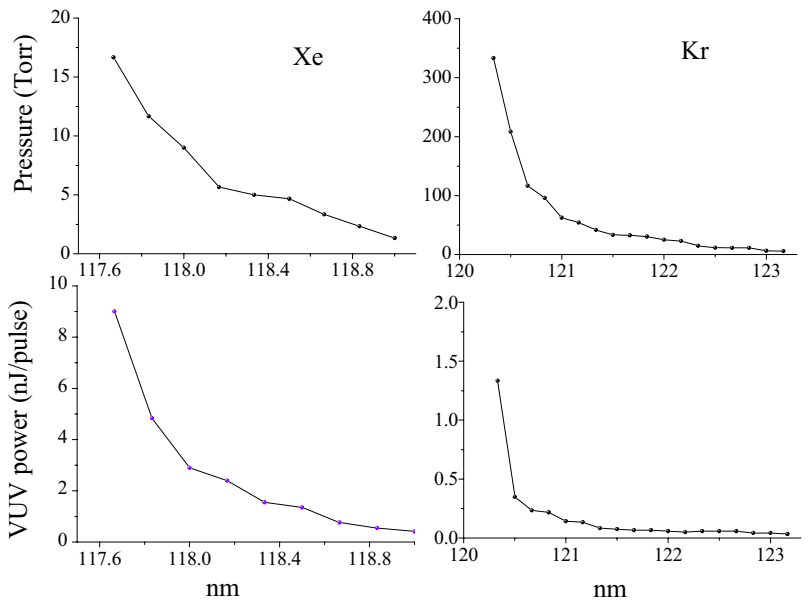

Fig. 3.5 *The optimum pressures for the phase matching in pure rare gases giving the maximum third order generation yield in the 117.6-118.9 nm Xe negative dispersion spectral domain and 120-123.2 nm Kr negative dispersion domain (upper panels). The spectral dependence of the power of the VUV radiation is given in the lower panels.*

These dependences are mapped in Fig. 3.6. As shown, when starting to add Ar in the tripling cell filled with Xe at the optimum pressure, the phase-matching condition breaks and the VUV intensity goes down. At higher Ar pressure a new phase matching is possible and the third harmonic yield increases. At some frequencies the maximum yield is even one order of magnitude larger, fulfilling the enhanced phase-matching by a proper gas mixture. Very similar enhancements were reported by Lockyer and Vickerman [101]. When Kr + Ar mixtures are used the addition of Ar until total pressures around 670 mbar created conditions for uncontrolled electrical discharge, photo-ionization and plasma formation in the tripling cell. This made the phase-matching for coherent VUV generation impossible.

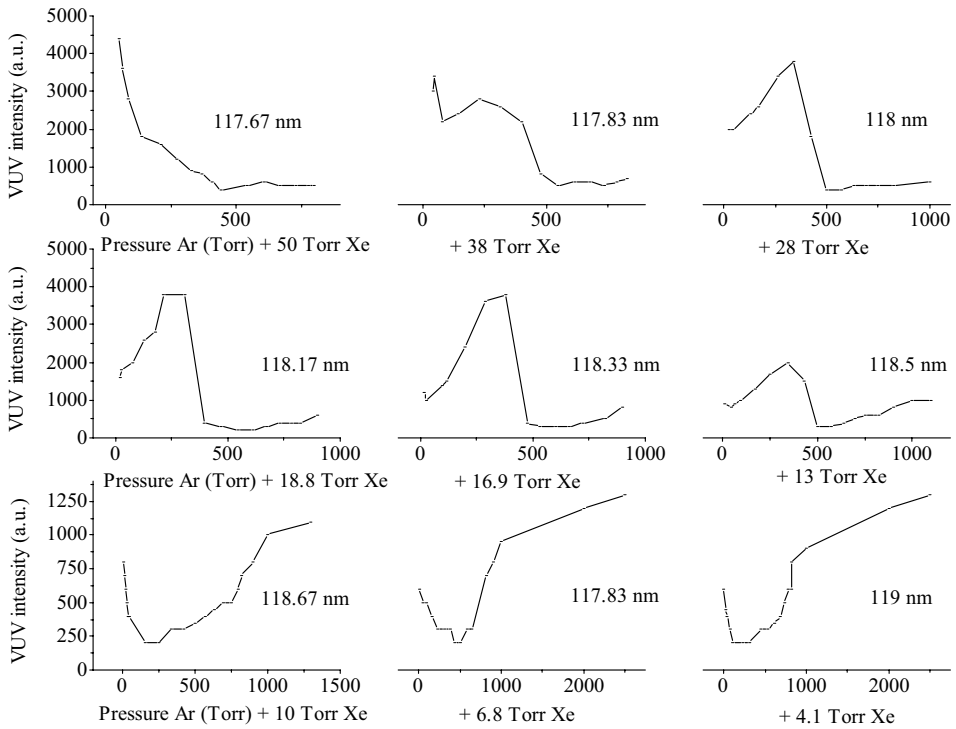

Fig. 3.6 *The intensity of the third harmonic generation at 9 different wavelengths as a function of total pressure of Xe + Ar used. For each wavelength the mixing is made using Xe at the pressure set for optimum tripling in pure Xe (Fig. 3.4) and adding Ar.*

Figure 2.15 shows a (1+1') REMPI spectrum of the HCl molecular beam of the transition V $^1\Sigma^+$, v'= 12 ←X $^1\Sigma^+$, v"= 0. The spectrum was measured using Xe at the optimum pressure for frequency tripling of 17 mbar. A (1+1') REMPI spectrum of HI is shown in Fig. 2.14. For this spectral region the Xe pressure for the tripling frequency is 50 mbar. REMPI spectra of Cl were measured using electrical discharges to dissociate HCl or Cl_2 seeded in He or Ar. The result is given in Fig. 3.7

3.4 Results

For all three OH (X $^2\Pi_{3/2}$, v = 0, J = 3/2, f) + HX systems we tried to observe the atomic reaction product X = Cl, Br and I, by applying (1+1') or (2+1) REMPI using the transitions given in Table 3.1 and Fig. 3.3. The VUV radiation around 118-120 nm and 142 nm was produced by third harmonic generation in Xe or Kr of a Nd:YAG pumped dye laser output, operating with LD 700 or LD 750 dyes and subsequently frequency doubled (≤ 7 mJ/pulse), and with Stilbene 3 (≤ 27 mJ/pulse), respectively. The UV radiation (≤ 3 mJ/pulse at 235 nm and 266 nm and ≤ 5mJ/pulse at 305 nm) was obtained by frequency doubling the dye laser output in BBO crystals, using C102, C 153 and SR 640 dyes.

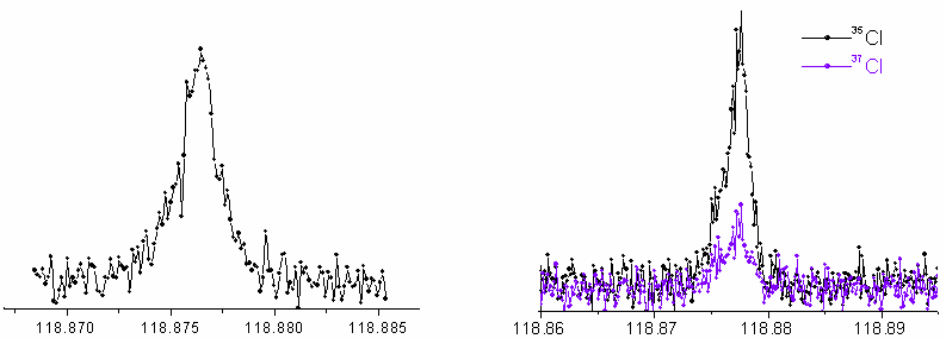

Fig. 3.7 *(1+1') REMPI spectrum of Cl produced by an electrical discharge in Cl_2-Ar mixture (a) and HCl-He mixture (b). The resonant one VUV photon excitation corresponds to 4s $^2D_{3/2,5/2}$ ← $^2P_{3/2}$ at 118.875 and 118.877 nm. Optimum tripling conditions are obtained at 3 mbar pure Xe.*

Since the absolute one and two-photon ionization cross sections are unknown for Cl and I, the ratio $N_{(2+1)}/N_{(1+1')}$, as expressed in Eq. 3.7, between the number of atomic ions obtainable by (2+1) REMPI and the number of ions obtainable by (1+1') REMPI can not be accurately estimated. Even if it is assumed that the ionization step is saturated the broad ranges in which the values of the one and two-photon absorption cross sections may vary do not allow a comparison of the two REMPI methods concerning the efficiency of the atom detection. Mixtures consisting of 5, 10 and 20% HCl in He were used for the secondary beam source in order to vary the reactive cross section, which is predicted to increase with the collision energy [21, 23]. The yield of Cl ($^2P_{3/2}$) from an electrical discharge in HCl or Cl_2 is considerably larger than the yield from the OH + HCl reaction, since the latter was not measurable. For (2+1) REMPI detection of Br and I atoms, the laser radiation is only weakly focused to increase the detection volume and to reduce the background atom signal due to the photo-dissociation of the halogen hydride.

Table 3.1 *Transitions tried for the REMPI detection of the atomic halogen product of the OH + HX reactions, for X = Cl, Br, and I*

Reaction product	Transition	Wavelength (nm)
Cl	(2+1) REMPI	
	$^2D_{3/2} \leftarrow {}^2P_{3/2}$	235.336 nm
	$^2P_{3/2} \leftarrow {}^2P_{1/2}$	236.527 nm
	(1+1') REMPI	
	$^2D_{3/2,5/2} \leftarrow {}^2P_{3/2}$	118.876 nm
	$^2D_{3/2} \leftarrow {}^2P_{1/2}$	120.135 nm
Br	(2+1) REMPI	
	$^4D_{5/2} \leftarrow {}^2P_{3/2}$	264.211 nm
	$^2D_{3/2} \leftarrow {}^2P_{1/2}$	266.697 nm
I	(2+1) REMPI	
	$(^3P_2)$ 6p $^2[3]^o_{7/2} \leftarrow {}^2P_{3/2}$	304.553 nm
	$(^3P_1)$ 6p $^2[1]^o_{1/2} \leftarrow {}^2P_{1/2}$	304.025 nm
	(1+1') REMPI	
	$(^3P_2)$ 5d $[2]_{5/2} \leftarrow {}^2P_{3/2}$	142.550 nm

In order to detect the ionized atoms we employ the Velocity-Map-Imaging method, so that the products of the reaction and the photolysis can be separated by their kinetic energy. The background from the photolysis still limited the detection of both halogen atoms with low kinetic energy, as shown by Fig. 3.8 (a) and (b), even though the detection transitions were chosen in the wavelength region at the edge of the UV absorption bands of the halides. Summations of images up to 150 000 shots for Bromine and Iodine ions did not reveal a reaction signal thus far.

In Fig. 3.8 (a) an image obtained by summation over 150 000 shots for OH+HBr reaction conditions is shown. The bright signal represents ionized Br $^2P_{3/2}$ with a velocity of 165 m/s, resulting from HBr photolysis at 264.211 nm.The Br $^2P_{3/2}$ produced by reaction is expected to have velocities of 583, 480, 507 and 380 m/s corresponding to the vibrational state predicted for the H_2O product, i.e. (1,1), (0,2), (2,1) and (1,2), respectively, in the order of the decreasing reaction cross section [21]. Ring images with the radii 3.5, 2.9, 3.1 and 2.3 times larger than the radius of the bright disc from Fig. 3.8 (a) are therefore expected, while for vibrational ground state water product the ring in the Bromine image is estimated to have a radius 4.8 times larger. The image from Fig. 3.8 (b) is obtained by acquisition over 100 000 laser shots for OH + HI reaction with detection of I $^2P_{3/2}$ at 304.553 nm. Fast Iodine atoms (244 m/s) from the photodissociation of HI are observed. Since the fastest I reaction product would have a velocity of 600 m/s, the corresponding image is expected to have a 5.7 times larger radius. The signal from the reaction would be not distinguishable from the photolysis signal in the case of H_2O product with the highest vibrational excitation possible, i.e. (1, 4). For (1+1') REMPI detection of Iodine atoms, after applying a mask on the detector in order to block the signal at low kinetic energy and increasing the detection gain, very fast Iodine atoms (957 m/s) ascribed to the dissociation of the I_2 were detected after 1000 images acquisition, as shown in Fig. 3.8 (c). Since the measurement methods were different for the inelastic and the reactive scattering, an upper limit for the cross sections for these reactive channels could not be derived from a comparison with the minimal observable inelastic cross section.

3.5 Conclusions

In our experiments no product has been so far detected for the reactions OH ($X^2\Pi_{3/2}$, v = 0, J" = 3/2, f) + HX ($X^1\Sigma^+$, v = 0, J < 4) $\rightarrow$ X ($^2P_{1/2,\ 3/2}$) + H_2O, with X = Cl, Br and I. Using the (2+1) or (1+1') REMPI methods with 235 nm or 119 nm + 357 nm photons, respectively, the detection of Cl product for the OH + HCl reaction is reasonably background-free. Much longer acquisition times may still be considered as means for detecting products.

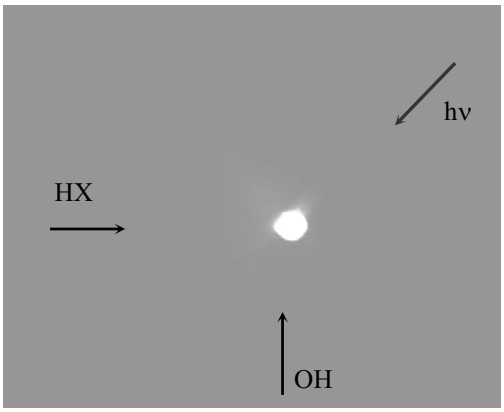

(a)

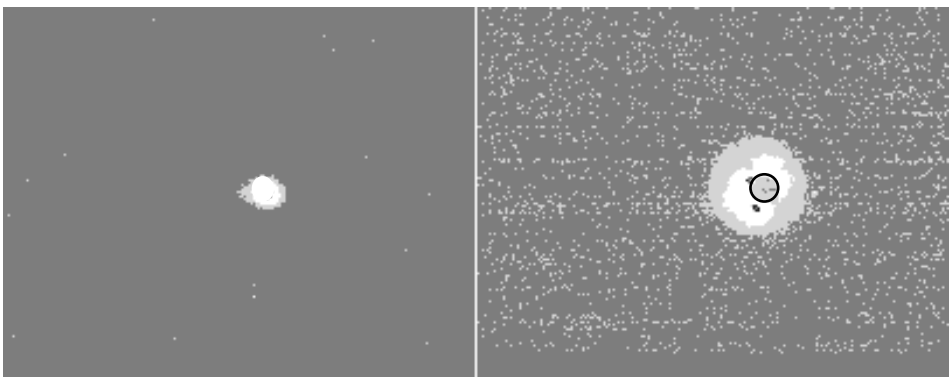

(b) (c)

Fig. 3.8 *Summations of images acquired by detection of halogen atoms, X, in OH+HX crossed-beam scattering: (a) Br at laser energy, hν, corresponding to 264.211 nm wavelength, and I at (b) 304.553 nm and (c) at 142.550 nm. The signal observed is attributed to photo-dissociation of HBr (a), HI (b and c) and I_2 (c). The image (c) was obtained for a higher gain of the detector and making use of a mask (the marked inner disc) to block the ions with low kinetic energy.*

For the study of the reactions of OH with HBr and HI with REMPI methods employing 264 nm and 305 or 143 nm photons, respectively, photo-dissociation of the Halogen Hydrides is the drawback. This sets a high threshold for the detection of the atomic reaction product. Ionization schemes requiring photons that are less efficiently absorbed by the Halogen Hydrides might be used (e.g., one-photon threshold ionization). The detection of Br atoms from the OH + HBr reaction under similar experimental conditions was recently performed successfully by Laser Induced Fluorescence at 154 nm [46]. LIF detection of the Cl, Br and I atoms could be therefore more efficient. Fluorescence detection provides no information about the differential cross section, however. An intermediate step for this study could employ a photolysis OH source, which produces less high energy ionizing photons and metastable species. In this case the state selector could be removed, giving a much shorter distance between the primary beam nozzle and the interaction region.

Chapter 4

State-to-state inelastic OH-HCl scattering in comparison with OH-CO and OH-N_2[§]

4.1 Introduction

Due to its abundance and reactivity, the OH radical is responsible for many chemical processes relevant for atmospheric and combustion chemistry [1-8]. Reactions of OH with H_2 and CO are important steps in the reaction chain of hydrocarbon/air flames. Concerning the chemistry of the Earth's atmosphere, reactive OH acts as an efficient scavenger for trace pollutants present in the troposphere and stratosphere. Reactions of OH with hydrogen halides, which are the major sinks for the halogens from the atmosphere that can participate in catalytic ozone destruction in the stratosphere, are known to be efficient re-converters of the halogens to the active forms. In particular, the OH + HCl reaction is the primary process that releases active chlorine in the atmosphere. Therefore, the rate of chlorine release from HCl controls the steady state Cl concentration in the stratosphere. In addition, the formation of HCl serves as the predominant chain termination step for the ClO_x catalyzed destruction of ozone.

The important role played by the OH + HCl reaction in the atmospheric chemistry has given rise to a wealth of experimental and theoretical studies of the reaction dynamics of this system. Quantitative information on the reactivity of the OH + HCl system is provided by an extensive set of kinetic experiments in which temperature dependent rate constants were measured in a wide temperature range [7, 14-20]. The several theoretical studies reported to date, approached the OH + HCl system at different levels of theory in order to develop the Potential Energy Surface (PES) governing the interaction and to calculate rate constants and reaction cross sections [21, 26].

[§] adapted from: R. Cireasa, M.C. van Beek, A. Moise and J.J. ter Meulen, J. Chem. Phys. 122, 074319 (2005); R. Cireasa, A. Moise and J.J. ter Meulen, J. Chem. Phys. 123, 064310 (2005)

Clary [21] performed quantum scattering calculations using the Rotating Bond Approximation (RBA) and a semiempirical potential energy surface with a classical energy barrier of 87 cm^{-1}. Steckler [22] applied variational transition-state theory using scaled *ab initio* electronic structure calculations to determine the minimum energy path (MEP). Using the Coupled Cluster with Single, Double, and Triple excitation method (CCSD(T)/PVQZ) they obtained a vibrational adiabatic ground-state reaction barrier (V_a^G) of 927 cm^{-1}. Yu and Nyman [23] carried out dynamical calculations using the RBA approach on a new PES obtained by interpolation of *ab initio* energy values computed using the Unrestricted Møller–Plesset method (UMP2) and scaling correction. The ground-state surface $^2A'$ calculated by Yu and Nyman exhibits a deep van der Waals well of –1910 cm^{-1} relative to the OH + HCl reactants possibly due to the strong dipole–dipole interactions and an early barrier (V_a^G) of 811 cm^{-1}. The theoretical calculations of Rodriguez and coworkers [24, 25] used the Large Angle Rotating Bond (LAGROBO) functional formulation of the interaction between OH and HCl in order to produce the PES. Parameters of the PES were adjusted in order to minimize the difference between the values of the rate constants obtained using quasiclassical trajectory (QCT) calculations and experimental values. The best agreement with experiments was obtained for a PES with a classical barrier of 850 cm^{-1} and a van der Waals well of -1910 cm^{-1}.

The connection between reactive and inelastic scattering for systems with highly attractive PES like OH + HCl is quite strong because the alternate complex formation-decomposition route to the inelastic process can also be regarded in a broader sense as a reactive event. A systematic study of both types of collisions is particularly fruitful in revealing the multifaceted nature of the collision dynamics and in testing the PES's developed to describe it. In spite of the great number of studies concerning the reactivity of this system, no experiments were reported so far for the state-to-state scattering of OH by HCl. Close coupling scattering calculations and quasi-classical trajectory calculations were performed by Kłos and coworkers [105] using only the V_{sum} of the PES, the results of which were compared with our experimental cross sections by ignoring their fine-structure. The development of a PES suitable for calculations on the non-reactive channel was lately approached by Wormer and coworkers [26]. The accuracy of different features of this PES is refined in order to allow for state-resolved quantum scattering calculations.

In this chapter a study of the inelasticity of the scattering of OH ($X\ ^2\Pi$) by HCl ($X\ ^1\Sigma^+$), in a crossed molecular beam set-up at collision energies around 920 cm^{-1}, is presented. Prior to collisions, the OH radicals are selected in a single quantum state, i.e., $\Omega = 3/2$, $J = 3/2$, $M_J = 3/2$, f. In the absence of other experimental and theoretical information concerning inelastic collisions of OH with HCl, we compare our data with results previously obtained by using a similar experimental set-up for the collisions of OH with CO ($E_{coll} = 450\ cm^{-1}$) and N_2 ($E_{coll} = 410\ cm^{-1}$).

In order to make the comparison more relevant, we performed new measurements on the OH + CO system at a collision energy E_{coll} = 985 cm^{-1}, comparable to that used in the OH + HCl experiments. Concerning the absolute magnitudes of the state-to-state cross sections for the OH + HCl collisions, one should expect higher values than for the other two systems, OH + CO and OH + N_2, given the stronger polar character and the higher polarizability of HCl as compared with CO and N_2 (see Table 4.1) and the consequently stronger intermolecular interactions. However, we are not able to determine absolute cross sections because this requires the knowledge of the secondary beam density which cannot be easily calibrated. We therefore restrict ourselves to the determination of relative state-to-state cross sections. These cross sections are measured for rotational excitations up to J = 9/2 within the Ω = 3/2 spin–orbit ladder and up to J = 7/2 within the Ω = 1/2 spin–orbit ladder. Information on the anisotropy of the interaction potential is inferred from the observed propensities for scattering into a particular Λ-doublet state, e or f.

Additional information on the PES anisotropy is obtained by investigating the effect of the relative orientation of the collision partners on the collision outcome. Favorable orientations of the OH molecule with respect to HCl may enhance possible competing effects implying reactive collisions when the collision energy exceeds the reaction barrier. The measured steric asymmetries are discussed in comparison with those obtained for collisions of OH with CO and N_2 at similar collision energies.

4.2. State-to-state integral cross sections

The values of the relative integral state-to-state cross sections measured in this experiment are listed in Table 4.2 and shown graphically in Fig. 4.1.

Table 4.1. *Polarity of HCl versus CO and N_2 [70]*

Polar character	HCl	CO	N_2
dipole moment (D)	1.08	0.11	0
quadrupole moment (10^{-10} D·m)	3.8	-2.0	-1.4
polarizability (10^{-30} m^3)	3.2	1.9	1.7

In order to enable a comparison of the three OH-Y systems, with Y = HCl, CO and N_2, the ratios of the relative cross sections to the relative cross section for the transition to the Ω' = 3/2, J' = 3/2, e state are considered:

$$\rho(\Omega', J', \varepsilon') = \frac{\sigma_{rel}(\Omega', J', \varepsilon')}{\sigma_{rel}(3/2, 3/2, e)} \cdot 100(\%). \qquad (4.1)$$

These results have been obtained for the OH-HCl system at 920 cm^{-1} collision energy, for OH-CO at 450 cm^{-1} collision energy and for OH-N_2 at 410 cm^{-1}. Listed in Table 4.2 are also the results of new measurements performed for the OH+CO system at a higher collision energy, 985 cm^{-1}. In Fig. 4.2 the ratios of the state-to-state cross sections for OH + HCl are presented together with the new data obtained for collisions of OH with CO. As can be noted from Table 4.2, rotational excitation of the OH radical into states up to J = 9/2 of the same spin-orbit ladder, Ω = 3/2, and J = 7/2 of the upper spin-orbit ladder, Ω = 1/2, could be detected within the sensitivity of this experiment. The maximum internal excitation requires only approximately 45% of the available collision energy of 920 cm^{-1}. The rotational energy transfer (RET) seems low in comparison to that measured for OH collisions with N_2, CO, He, Ar and CO_2 at lower collisions energies [39, 50, 111] and for NO collisions with He and Ar [40].

Besides a genuine 'inefficient' RET, several other factors may be responsible for this low conversion rate. Generally, the S/N ratio for the measurements of the excitation into higher J states, for which the cross sections are smaller, is decreasing making the detection difficult. Moreover, for the OH + HCl system, we also have to take into account that for collision energies above the reaction barrier, reactive processes may play a role in the dynamics. The reaction barrier was predicted to lie between 850 and 915 cm^{-1}, but some comparisons of the TS rate constants to the experimental values suggested that the real value might be as low as 350 cm^{-1} [21-25]. Therefore, the collision energy of 920 cm^{-1} used in this experiment is likely to exceed the reaction barrier. If reactions do take place, the collision-induced populations of higher rotational states may drop below the detection limit.

As can be seen from Figs. 4.1 and 4.2, the behavior of the relative cross sections with the amount of rotational excitation, ΔE_{rot}, appears to obey an energy-gap law: its magnitude is decreasing as ΔE_{rot} increases. This is qualitatively similar to the trend obtained for OH + CO and OH + N_2 collisions, except for the values measured for excitation into higher rotational states of the Ω = 1/2 spin-orbit ladder. A propensity for spin-orbit conserving transitions is apparent when similar amounts of rotational excitation are considered. Generally, the same propensity was found for collisions of OH with Ar, He, N_2, CO and CO_2 [43, 55, 106, 57].

Table 4.2. *Ratios of state-to-state cross sections to the cross section for the transitions to the Ω'= 3/2, J' = 3/2, e for inelastic collisions of OH ($X\,^2\Pi_{3/2}$, v'' = 0, J'' = 3/2, f) with HCl presented in comparison with the cross sections ratios obtained for the scattering of OH by CO and N_2 [106]. The errors represent one standard deviation and for OH + HCl were obtained by statistical analysis weighting with $1/q^2$, where q is the error for one individual measurement.*

Final state			OH+HCl	OH+CO		OH+N_2
Ω'	J'	ε'	E_{coll} = 920 cm^{-1}	985 cm^{-1}	450 cm^{-1}	410 cm^{-1}
3/2	5/2	e	11.34±0.481	14.20±0.51	10.40±1.58	12.25±1.75
	5/2	f	11.70±0.59	10.72±0.51	8.00±1.13	4.90±0.70
	7/2	e	3.18±0.28	4.64±0.20	2.20±0.31	1.85±0.27
	7/2	f	3.16±0.30	-	2.44±0.36	1.78±0.27
	9/2	e	0.88±0.18	1.09±0.13	0.14±0.06	0.67±0.16
	9/2	f	1.48±0.54	0.67±0.17	0.24±0.08	0.78±0.03
1/2	1/2	e	2.69±0.16	4.05±0.26	2.92±0.42	3.50±0.83
	1/2	f	2.65±0.37	3.04±0.30	2.46±0.36	2.50±0.35
*	3/2 &5/2	e	3.22±0.23	4.20±0.31	2.04±0.30	1.68±0.24
	3/2	f	1.50±0.15	2.03±0.23	1.42±0.23	1.40±0.24
	5/2	f	2.35±0.44	2.27±0.28	0.90±0.13	0.20±0.10
	7/2	e	1.57±0.18	-	-	-

***** *the measured cross section contains contributions from both 3/2 e and 5/2 e states as the absorption lines used to probe them could not be resolved within the laser bandwidth.*

Notably, for OH + HCl system, no evident propensity for excitation into a particular Λ-doublet component of the same rotational state was measured. If the de-excitation into the Ω = 3/2, J = 3/2, e state is not taken into account, the ratios between the sum of the cross sections for scattering into states of e symmetry and the sum of the cross sections for scattering into states of f symmetry within the same spin-orbit ladder, Ω = 3 /2, are 0.94, 1.2, 2.2, 9.4 and 6.3 for collisions with HCl, CO, N_2, Ar and He, respectively. The same trend of the e/f cross section ratio was found for scattering into the Ω = 1/2 spin-orbit component, though the propensity is weaker: 0.91, 1.0, 1.3, 2.3 and 2.6. It seems that the e/f cross section ratios are in line with the polarity of the collision partner. The most spherically symmetric collision partner has the highest propensity for scattering into states of e symmetry, while for the most polar molecule there is no propensity.

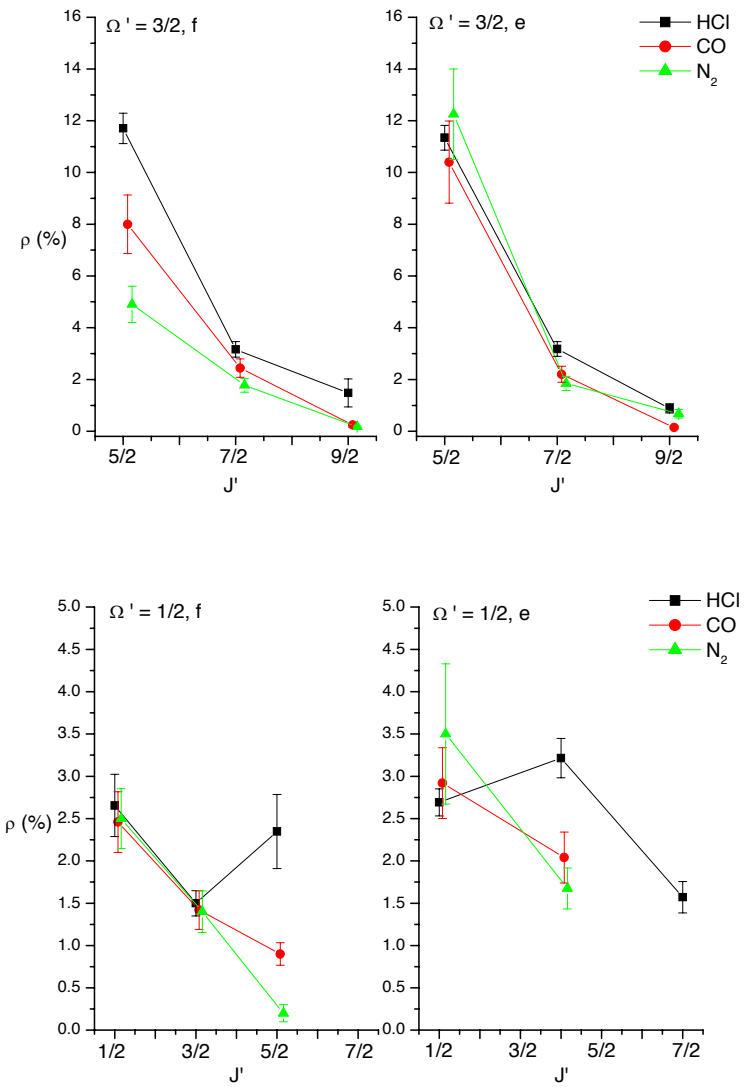

Fig. 4.1 *Ratios, ρ (Ω', J', ε') (%), of the absolute state-to-state inelastic cross sections to the absolute cross section for the transition to the Ω'= 3/2, J'= 3/2, e state of OH ($X\,^2\Pi$, v = 0) Ω''= 3/2, J''= 3/2, f in collisions with N_2 at 410 cm^{-1} collision energy (triangles), with CO at 450 cm^{-1} collision energy (circles), and with HCl at 920 cm^{-1} collision energy (squares), for the transitions to the Ω'= 3/2 states – upper panel and to the Ω'= 1/2 states-lower panel. The transitions to the Ω'= 1/2, J'= 3/2 and 5/2 e sattes are characterized by the sum of their cross sections as the absorption lines used to probe them could not be resolved within the laser bandwidth.*

For the scattering of OH by CO the increase of the collision energy determines a decrease of the cross section for the Λ-doublet transition and, therefore, an increase of the ratios (Eq. 4.1), but the general trends are unchanged. The magnitude of the inelastic cross sections and the scattering propensities reflect the shape of the potential energy surface (PES) governing the interaction between the collision partners.

Considering the complexity of the quantum treatment of a 4-atom system, the development of a full dimensional PES is a very demanding task and the prior knowledge of the cross sections may be helpful in refining different features of the PES. OH is an open shell molecule with a $^2\Pi$ ground state. In the absence of external fields this state is degenerate, but the approach of the collision partner lifts this degeneracy, giving rise to two electronic potential surfaces on which the collision takes place. If the collision partner is spherically symmetric (e.g. Ar), the colliding particles occupy the same plane and the two potential surfaces have either A' or A" symmetry with respect to the reflection of the spatial electron coordinates relative to the triatomic plane. For a molecule with a π^3 electronic configuration, as is the case for the OH radical, the A' symmetry corresponds to a distribution of the half filled π orbital in the scattering plane and to a distribution of completely filled π orbital perpendicular to this plane, whereas for the A" symmetry the orbital distribution will be the opposite [57]. The corresponding PES's defined in the body-fixed (collision) frame may then be labeled by $V_{A'}$ and $V_{A"}$, according to their symmetry. However, when the collision partner is not spherically symmetric, as for the interaction of OH with HCl, CO or N_2, there is in general no plane of symmetry.

It has been found at different levels of theory [22, 24-26] that for the OH-HCl interaction the most stable van der Waals complex has a planar geometry. If we consider the OH collision partner as a pseudo-atom and restrict the discussion only to planar collision geometries, it will be possible to use the above notation for the PES's and to use the scattering formalism described by Alexander [57] employing the PES's under the following forms:

$$V_{sum} = \frac{1}{2}(V_{A'} + V_{A"}), \tag{4.2}$$

$$V_{dif} = \frac{1}{2}(V_{A'} - V_{A"}). \tag{4.3}$$

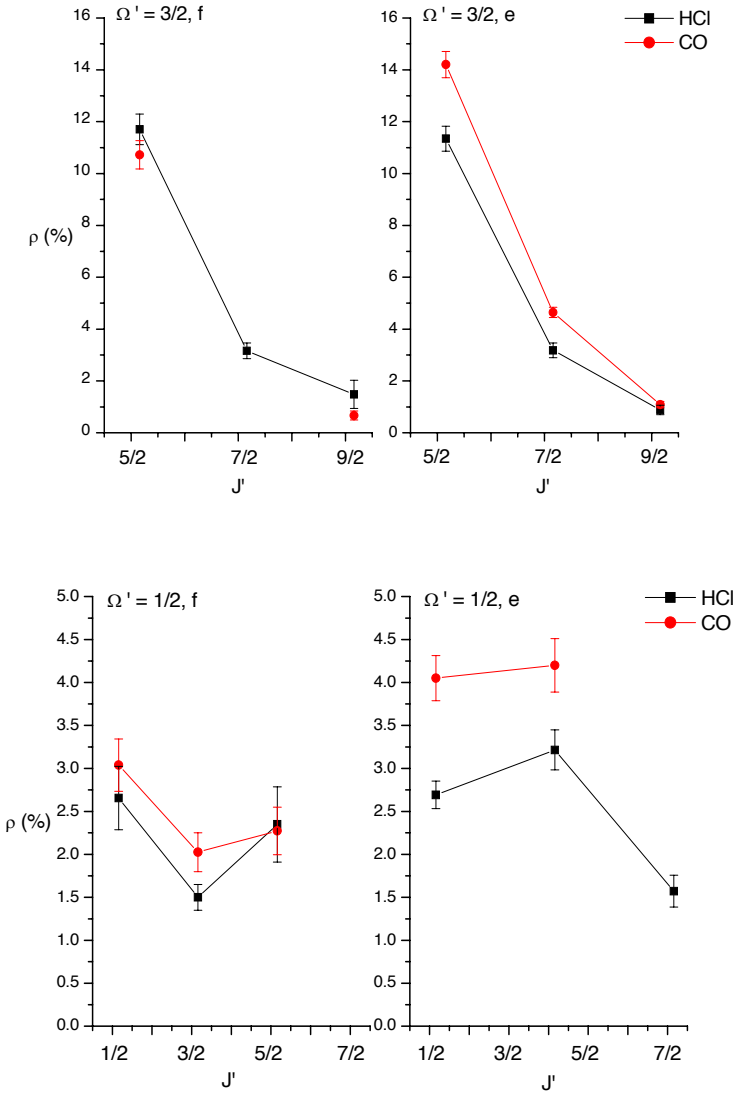

Fig. 4.2 *Ratios, ρ (Ω', J', ε') (%), of the absolute state-to-state inelastic cross sections to the absolute cross section for the transition to the Ω'= 3/2, J'= 3/2, e state of OH ($X^2\Pi$, v = 0) Ω''= 3/2, J''= 3/2, f in collisions with CO at 985 cm^{-1} collision energy (circles) and with HCl at 920 cm^{-1} collision energy (squares), for the transitions to the Ω'= 3/2 states – upper panel and to the Ω'= 1/2 states-lower panel.*

The angular and radial dependence of the sum and the difference potential can be expressed as [57]:

$$V_{sum}(R,\theta) = \sum_{l=0} V_{l0}(R) d^{l}_{00}(\theta), \tag{4.4}$$

$$V_{dif}(R,\theta) = \sum_{l=2} V_{l2}(R) d^{l}_{20}(\theta), \tag{4.5}$$

where $d^{l}_{00}(\theta)$ and $d^{l}_{20}(\theta)$ represent reduced rotation matrix elements and are proportional to regular and associated Legendre polynomials, respectively, and $V_{l0}(R)$ and $V_{l2}(R)$ are expansion coefficients describing the radial dependence of the potentials. They multiply the angular dependence of the potentials and therefore reflect the anisotropy of the PES. Coefficients with even l contribute to the potential surface which is head-tail symmetric with respect to the OH molecule orientation while terms with odd l contribute to the potential surface which is head-tail antisymmetric. The scattering matrix depends explicitly on the $V_{l0}(R)$ and $V_{l2}(R)$ coefficients [107]. Consequently, an estimation of their relative magnitude can be obtained from the values of the relative cross sections. It was shown that for a pure Hund's case (a) coupling and a triatomic collision system, the spin-orbit conserving transitions are governed by the sum potential, V_{sum}, and the spin-orbit changing transitions are governed by the difference potential, V_{dif}. OH can be treated as Hund's case (a) only for the lowest rotational levels.

The e/f propensities in OH + CO and OH + N_2 collisions for excitation of OH into the $\Omega = 3/2$, $J = 5/2$ states indicate a preference for transitions into rotational states of e symmetry. In terms of interaction potential this corresponds to stronger even l terms (see Table 6.2) and consequently to higher head-tail symmetry of the PES than in the OH + HCl interaction [107]. Hence, a weaker anisotropy of the potential is expected for the interaction of the OH with CO and N_2 than for the interaction with HCl. This is also indicated by the observed cross sections for the transition to the $\Omega = 1/2$, $J = 1/2$ states. According to the expression for the scattering matrix from Ref. [107], the excitation into these states can be only induced by the $l = 1$ term of the potential (V_{10}), responsible for the symmetry conserving transition, and the change the $l = 2$ terms of the potential (V_{20} and V_{22}), responsible for the change in symmetry. The ratio between the cross section for scattering into the $\Omega = 1/2$, $J = 1/2$ state of e symmetry and the cross section for scattering into the $\Omega = 1/2$, $J = 1/2$ state of f symmetry is larger for the OH-CO and OH-N_2 scattering than for OH-HCl, indicating that the V_{10} term is stronger for OH-HCl under the condition that the V_{20} term is not larger than the V_{22} term, as in the case for OH-He, OH-Ar and OH-Xe.

The anisotropic character of the potential seems be consistent with the results of theoretical calculations, which predict the most stable structure of the van der Waals complex to be formed at the O-side, ClH-OH. This complex would have a quasi-linear structure with the angle between the OH bond axis and the intermolecular axis close to the bond angle in H_2O. The depth of the van der Waals well was estimated to be in the range 870-1900 cm^{-1} [24-26]. For the interaction between OH and CO, it was shown experimentally and theoretically that two linear complexes, OH-CO and OH-OC, may be formed, with a dissociation energy, D_e, of 700-800 cm^{-1} and 400-500 cm^{-1}, respectively [108-110].

4.3 State-to-state steric asymmetries

The values of the steric asymmetries (Eq. 2.24) measured for collisions of OH with HCl in comparison with those previously obtained by our group for the inelastic collisions of oriented OH with CO and N_2 [111] are displayed in Table 4.3 and Fig. 4.3. As can be seen from Table 4.3, the steric asymmetry measured for OH + HCl system depends on the spin-orbit manifold and on the Λ-doublet symmetry of the final state and varies between 18.8% for the Ω = 3/2, J = 9/2, e state and -21.3% for the Ω = 3/2, J = 7/2, f state for spin-orbit conserving transitions, and between 9.2% for the Ω = 1/2, J = 7/2, f state and -22.2% for the Ω = 1/2, J = 5/2, state for spin-orbit changing collisions. The overall variation is similar to that observed for the OH + N_2 system, for which S varied from 25.2% for the Ω = 3/2, J = 5/2, f state to -17.7% for the Ω = 3 /2, J = 7/2, f state, but slightly lower than measured for the OH + CO system, for which S varied between 23.2% for the Ω = 3/2, J = 5/2, f state to -29.4% for the Ω = 3/2, J = 9/2, f state. It is interesting to note that for all the collision partners the highest absolute values of the steric asymmetries were generally found for spin-orbit conserving transitions. For scattering into rotational states of the same spin-orbit manifold, Ω = 3/2, we measured negative values for symmetry conserving transitions and zero or positive values for symmetry changing transitions. In turn, for spin-orbit changing transitions, Ω" = 3/2 → Ω' = 1/2, S is slightly positive and almost independent of the final rotational state and its Λ-doublet symmetry, except for the negative value measured for the excitation into the Ω = 1/2, J = 5/2, f state. This behavior is different from that measured for collisions between OH and CO or N_2. Generally, for these systems, S exhibits a quasi-monotonical dependence on the rotational quantum number of the final state, with positive values at low J and negative ones at high J. An intuitive reasoning can be used to explain such generic behavior. Considering that the unpaired electron occupying the π orbital is located closer to the O atom, one might expect a propensity for collisions at the O-side (positive S).

Conversely, the preference for collisions at the H-side (negative S) observed for excitation into high rotational states could be pictured in a classical manner using the ball-and-stick model. It is more efficient to exert a large torque, needed for high rotational excitations, at the H-side as it is further away from the center of mass. These models were used to rationalize the rotational dependence of S observed in the collisions of OH with the "spherical" Ar atom [43]. Nevertheless, these simplistic explanations cannot be used to describe the behavior of the OH + HCl system for which the intermolecular interactions are much stronger due to the existence of quadrupole and dipole moments.

While for collisions with CO and N_2, the steric asymmetry is positive for the excitation into the lowest rotational state, $\Omega = 3/2$, $J = 5/2$, f, the collisions between OH and HCl lead to a negative S with an absolute value of 16.5 ± 1.6. This result represents the most striking difference in the behavior of the OH + HCl system as compared to the OH + CO and OH + N_2 systems.

Table 4.3. *Steric asymmetries measured for inelastic collisions of OH with HCl presented in comparison with the steric asymmetries obtained for the scattering of OH by CO and N_2 [111]. The errors represent one standard deviation and for OH + HCl were obtained using a weighted statistical analysis.*

Final state			OH+HCl	OH+CO	OH+N_2
Ω'	J'	ε'	E_{coll}= 920 cm^{-1}	E_{coll}= 985 cm^{-1}	E_{coll}= 985 cm^{-1}
3/2	5/2	e	3.0±1.2	-1.6±0.5	1.1±0.7
	5/2	f	-16.5±1.6	23.2±1.6	25.2±1.9
	7/2	e	-1.1±3.5	-8.8±0.8	-4.9±1.1
	7/2	f	-21.3±5.4	-23.4±2.8	-17.7±3.1
	9/2	e	18.8±12.4	-17.7±3.5	-5.5±2.6
	9/2	f	-5.28±6.53	-29.4±7.2	-7.0±3.9
1/2	1/2	e	6.7±4.0	-3.3±0.7	-13.4±1.0
	1/2	f	-0.3±3.7	10.2±1.0	1.1±1.8
	3/2 & 5/2	e*	7.1±3.3	-6.4±0.8	-5.3±1.2
	3/2	f	9.2±8.6	11.8±1.3	4.3±1.9
	5/2	f	-22.2±10.6	-6.6±1.8	-4.9±2.1

** the measured steric asymmetry contains contributions from both 3/2 e and 5/2 e states as the absorption lines used to probe them could not be resolved within the laser bandwidth*

Basically, a negative value for S means that a smaller number of OH molecules was detected in the final state, after collisions at the O-side than upon collisions at the H-side. This corresponds to larger inelastic cross sections for the scattering at the H-side, but also could be an indication that a part of the OH molecules colliding with the O-side are 'removed' from the detection region.We should recall here that for each quantum state, the collision signals for both orientations were recorded in the same measurement session. In particular, for scattering into the lowest rotational state, $\Omega = 3/2$, $J = 5/2$, f, the steric asymmetry was obtained by averaging over a set of 45 measurements recorded over a widespread period of time, indicating that its negative sign is not due to an experimental artifact.

The negative value for S is due to the anisotropy of the interaction potential with respect to the approach of HCl molecules to one or the other end of the OH radical. Therefore, by examining the topology of the PES we can obtain information to explain this behavior. The existence of strong dipole moments for both HCl and OH determines strong long-range electrostatic interactions which lead to the formation of van der Waals wells. It was found using different levels of theory [23, 25, 26, 105] that the deepest van der Waals well is located at the O-side of the OH radical and its depth was estimated in the range 870-1900 cm^{-1}. A*b-initio* calculations employing restricted coupled cluster with single, double and perturbative triple excitation (RCCSD(T)) and multi-reference configuration interaction methods of Wormer and coworkers [26] revealed on the ground-state potential surface $^2A''$, a planar L-shaped global HO--HCl complex ($\theta_{HOH} = 111^o$ and $\theta_{OHCl} = 176^o$), with a binding energy of 1123 cm^{-1}, and a T shaped local OH--ClH complex ($\theta_{HOH} = 6^o$ and $\theta_{OHCl} = 67^o$), with 655 cm^{-1} binding energy. Similar geometry and dissociation energy for the global HO--HCl complex were obtained by Lendvay [112] from a*b-initio* calculations employing quadratic configuration interaction with single, double and perturbative triple excitation (QCISD(T)). Three other more weakly bound complexes were found using the QCISD(T) method, but only one resulted in an intermolecular bond at the H-side ($D_0 \approx 250$ cm^{-1}) located on the excited potential surface, $^2A'$. Exploring the PES landscape farther into the reactive region, an early transition state (TS) can be located in the entrance channel of the $^2A'$ surface. The geometry of the TS is bent and non-planar with a H-O-H angle similar to the angle formed by the bonds of the H_2O product [22, 23, 25, 112]. In turn, the geometry is quasi-linear with respect to the approach of the HCl molecule ($\theta_{OHCl} = 143°$-$156°$), as typically found for the heavy-light-heavy reaction type. The TS and the van der Waals structure bear a remarkable similarity, (besides the torsion) only a shortening and a slight bending of the intermolecular bond are required to attain the saddle point configuration from the geometry of the complex. Thus, the orientations conducive to the formation of the HO--HCl complex are also favorable for the reaction and this complex is likely to act as a precursor for the reaction.

On the basis of the theoretical calculations presented above, the negative steric asymmetry could be interpreted as a manifestation of the van der Waals forces. Thus the experimental fact suggests that the HO--HCl well seems to influence the dynamics at this low collision energy. In the single collision regime, if 'formed', the van der Waals complex is born with an excess of internal energy that may be used to surmount the reaction barrier and/or to (pre)-dissociate the complex.

Besides the relative orientation of the reagents, the reactivity is also controlled by the height of the barrier to the reaction. This was estimated from the kinetic data to lie between 200 and 800 cm^{-1} and by theoretical calculations to be around 800-900 cm^{-1} [20, 22, 23, 25, 82]. Yu and Nyman [23] found a vibrational adiabatic ground-state barrier height (V_a^G) of 810 cm^{-1}, but had to lower it to 350 cm^{-1} in order to obtain agreement with the experimental rate constants. Steckler et al. [22] who calculated a higher barrier (V_a^G = of 920 cm^{-1}) using the CCSD(T) method appreciated an uncertainty much larger than 100 cm^{-1} due to the use of different basis sets for the calculation of the zero-point energies. Consequently, it is reasonable to assume that the real barrier to the reaction would be in the range of 300 to 800 cm^{-1} and that the collision energy of the present experiment (920 cm^{-1} with a FWHM of 250 cm^{-1}) is very likely exceeding the barrier. The reaction cross section at this collision energy was estimated to be $1.5 \cdot 10^{-20}$ m^2 [23], quite similar in magnitude with the inelastic cross sections [105]. Moreover, Yu and Nyman [23] found that at low collision energies, the reaction between OH and HCl is dominated by the van der Waals forces determining tunneling effects. Supposing that the effect of the reactions is non-negligible, the OH molecules with favorable orientations may be removed from the detection region due to reactions. Under this hypothesis, the negative value obtained for the steric asymmetry can be interpreted not only as a reflection of the head-tail asymmetry of the PES, but also as an indication of possible reactions interfering in the dynamics at this collision energy.

The idea that the van der Waals well may influence the dynamics at low collision energies has some precedent confirmed both experimentally and theoretically for the Cl + HD reaction. In this case, the weak van der Waals well, located in the entrance channel, has a substantial effect on the reaction branching ratio at low collision energies when HD is rotationally unexcited [113].

Furthermore, recent five dimensional (5D) quantum wavepacket calculations and a QCT study of the reaction probabilities for the OH + CO system indicate that the van der Waals interaction in the entrance channel is largely responsible for the reactivity at collision energies below 1650 cm^{-1} [114, 115].

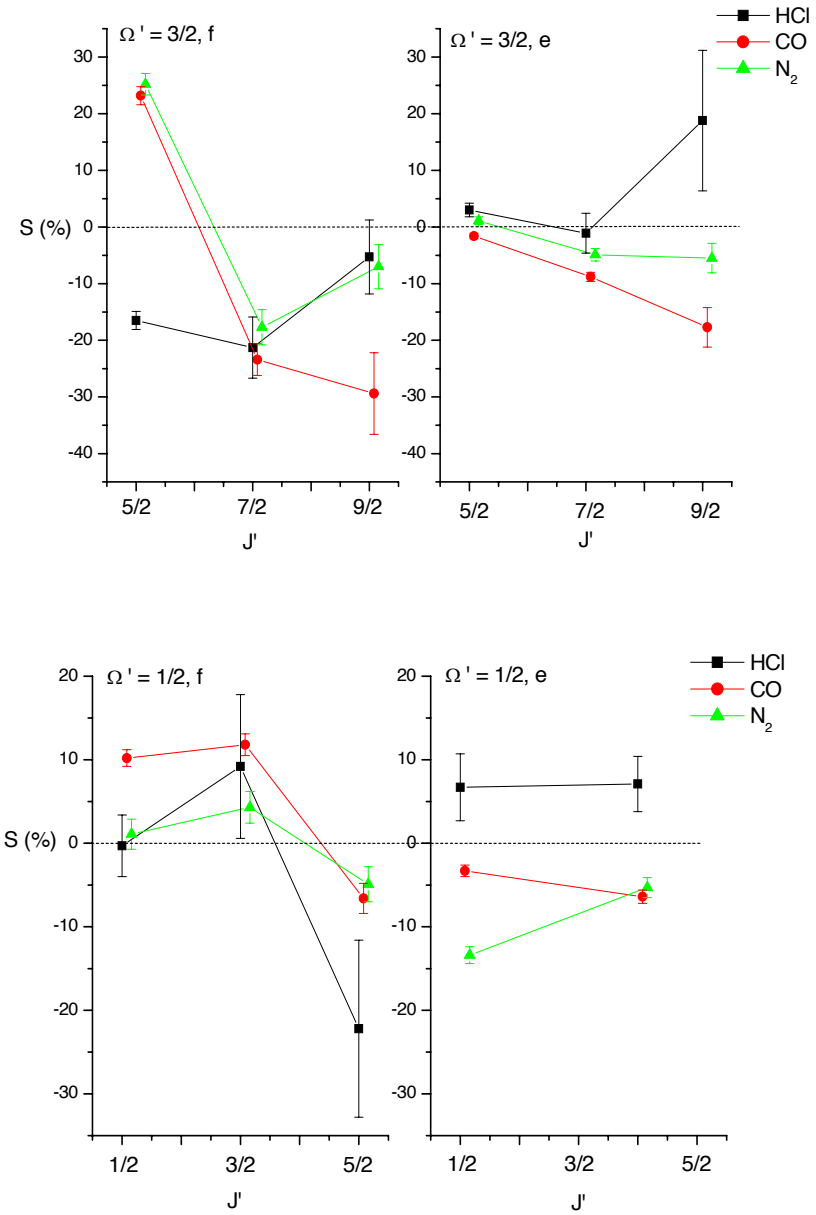

Figure 4.3. *Steric asymmetry for inelastic collisions of OH with HCl, CO and N_2 measured at the collision energies of 920 cm^{-1}, 985 cm^{-1} and 985 cm^{-1}, respectively. The final spin-orbit state and the Λ-doublet symmetry are indicated at the top of each panel.*

The PES for the OH + CO system contains two linear van der Waals complexes: OH-CO (D_e = 700-800 cm^{-1}) and OH-OC (D_e = 400-500 cm^{-1}) and two reactive intermediates, trans-HOCO and cis-HOCO, with deep wells of about 10000 cm^{-1}, which play an important precursor role connecting the reactants to the products [118, 109, 110]. From electronic structure calculations it was found that the van der Waals complexes evolve directly into cis/trans-HOCO intermediates by intermolecular bending motion [108]. Due to the low reaction barrier (V_a^G = 400 cm^{-1}) [110], at the collision energy of 985 cm^{-1}, the molecules could sample the whole PES. Taking into account these theoretical predictions, one may expect that the most favorable orientation for reactions occurs when the OH radicals are oriented with the H-side towards CO, resulting in a positive steric asymmetry in agreement with the sign of the value measured for the scattering into the Ω = 3/2, J = 5/2, f state. The scattering of OH by N_2 exhibits a similar stereodynamics as the OH + CO system for rotational excitation into this state. According to Ref. [116], the deepest van der Waals well corresponds to a linear molecular structure with a binding energy (D_e) of about 460 cm^{-1} and is also located at the H-side. From the comparison of the steric asymmetry measured for low rotational excitation (Ω = 3/2, J = 5/2, f) of OH as a result of collisions with HCl, CO and N_2, one finds that the corresponding sign of the steric asymmetry is related to the orientation of the OH within the van der Waals complexes. In contrast, the steric asymmetry for the scattering of OH by HCl into the Ω = 3/2, J = 5/2, e state is very small and positive. A similar value was also measured for the collisions implying excitation into the Ω = 3/2, J = 7/2, e state. In turn, a large positive steric asymmetry was measured for excitation into the Ω = 3/2, J = 9/2, e state which seems to be at variance with the other values. We have shown above that the dynamics at these collision energies seems to be influenced by the van der Waals well, therefore we could also expect the formation of energized van der Waals complexes which would dissociate releasing OH radicals with a preferential electronic orbital configuration. Unequal populations of the two lambda-doublet states corresponding to the two possible configurations of the OH electronic orbital were already found in the dissociation of water and of other OH containing complexes [117, 118].

The excitation into low rotational states of the Ω = 1/2 ladder is mainly governed by the difference potential, V_{diff}, which according to recent *ab-initio* calculations seems considerably less anisotropic than V_{sum} and exhibits only a shallow well [26]. The experimental results are in agreement with this smaller anisotropy resulting in a reduced influence of the OH orientation on the magnitude of the inelastic cross sections. We should note though that the steric asymmetry for excitation into the Ω = 1/2, J = 5/2, f state is clearly different from zero. The negative value of S could be due to the contribution to the scattering amplitude of the more anisotropic terms of the V_{sum} potential.

This interference of V_{sum} in the scattering dynamics involving the spin-orbit changing transitions is increasing with the excitation into higher rotational states for which the OH angular momentum coupling is no longer described by a pure Hund's case (a) [107].

At the low collision energies used in the experiments investigating the scattering of OH by HCl, CO and N_2, the long-range dipole-dipole and dipole-quadrupole interactions appear to dominate the dynamics at least for the lowest rotational excitation. However, it is also known that strong long-range anisotropic forces may induce a loss of the initial state orientation of the reactants, through trapping and reorientation effects [119, 120]. Trapping may cause a reduction of the steric effect for collisions taking place at large intermolecular distances. In this case, the collision partner being captured by the partly attractive potential will fly around the target molecule and will collide with it on the side or even at the back. The reorientation effects consist in a change of the molecular axis orientation due to the same long-range forces, resulting in a reduction of the steric effect and may also be present over a wider range of impact parameters than trapping. In general, the collisions at large impact parameters are responsible for the excitation into low rotational states. Conversely, the collisions resulting in a large change in the internal energy will occur mostly at small impact parameter. Consequently, the reduction of the steric effect may affect all final rotational states excited in the present experiment.

An inspection of the steric asymmetry, S, measured for the highest rotational state excited in the present experiments, Ω = 3/2, J = 9/2, f, reveals a reduction of its absolute value as compared to the values determined for excitation into lower J states. If reorientation effects would take place, the prepared orientation would be scrambled as the molecular axis of the two partners would be steered by the long-range interaction into a preferred orientation. In these conditions, the scattering signals measured for the two initially prepared orientations will differ less and S will diminish and approach zero which may explain the reduction of the steric asymmetry for the transition to the Ω = 3/2, J = 9/2, f, state. Because OH is not rotating and has a lower moment of inertia than HCl, its axis would reorient easier. Besides, for HCl molecules which are rotating, the intermolecular axis cannot orient itself so easily. The strong dipole-dipole interactions may reorient some of the molecules initially oriented with the H-side towards HCl in such a way that their O-side would be more exposed to the HCl attack. The strength of the long-range interactions and the initial state of the colliding partner determine the degree of reorientation. As the long-range forces are the strongest for the interaction between OH and HCl we also should expect stronger reorientation effects than in the case of OH + CO and OH + N_2 systems. In addition, assuming that the beam temperature is the same for all OH collision partners, about 20 K, the rotational population distribution will peak at higher rotational states for CO and N_2 as compared to HCl for which the most populated states at this temperature are J = 0 and J = 1.

For the former two, the long-range electrostatic forces are averaged over the rotational distribution which will result in their further reduction as compared to those describing OH-HCl interaction and weaker reorientation effects are to be expected. Of course, the magnitude of the reorientation effects depends also on the time needed for OH molecular axis to reorient itself as compared to the relative velocity. It is difficult to asses the reorientation issue for the excitation into $\Omega = 3/2$, J = 9/2, f state, partially due to the large experimental uncertainties affecting the measurement of the corresponding steric asymmetry. Therefore, additional experiments and theoretical calculations are required to provide higher accuracy information and a systematic survey of S by varying the initial conditions as relative velocity and rotational temperature.

4.4. Summary

Relative state-to-state cross sections for inelastic scattering of OH ($X^2\Pi$) by HCl ($X^1\Sigma^+$), measured at a collision energy of 920 cm^{-1} are reported. Prior to the collisions, the OH radicals are prepared in a single quantum state, $\Omega = 3/2$, J = 3/2, f, by means of rotational cooling in a supersonic expansion followed by an electrostatic state selection. In the absence of other experimental and theoretical data concerning this system, the results are compared in a qualitative manner with results previously obtained for the collisions of OH with CO (E_{coll} = 450 cm^{-1}) and N_2 (E_{coll} = 410 cm^{-1}) under similar experimental conditions. To allow for a quantitative comparison, we have also performed new measurements for the OH + CO system (E_{coll} = 985 cm^{-1}) using the same experimental set-up. As noted previously, for collisions of OH with CO and N_2, there is a propensity for spin-orbit conserving transitions that tends to decrease with the amount of the rotational excitation. With respect to the Λ-doublet symmetry, in the collisions of OH with HCl, no propensity is found. This behavior is notably different from that for collisions of OH with N_2, for which a propensity for symmetry changing excitation was found, similarly to the collisions with spherical partners studied in earlier work. For the OH + CO system, the propensity for symmetry changing excitations is much weaker and mainly apparent at low rotational excitations. This lack of preference for a Λ-doublet state is related to the shape of the PES governing the collision process and suggests that the PES is less head-tail symmetric with respect to the OH orientation for the interaction with HCl than for that with CO and N_2.

From the rotationally resolved relative cross sections for collisions in which OH is oriented with either the O-side or the H-side towards HCl, we have derived the steric asymmetry S. The results are presented in comparison with data previously obtained by our group for collisions of OH with CO (E_{coll} = 985 cm^{-1}) and N_2 (E_{coll} = 985 cm^{-1}) under similar experimental conditions.

Once again, the comparison with these two systems points towards the fact that the PES is less head-tail symmetric with respect to the OH orientation for the interaction with HCl than for that with CO and N_2 as it was also indicated by the lack of Λ-doublet propensity found for the relative cross sections measured for collisions between HCl and non-oriented OH radicals.

A remarkable difference was observed for the scattering into low J states where a preference for collisions at the H-side (negative S) was found, while for the OH + CO/N_2 system the collisions at the O-side (positive S) were preferred. A decrease in the negativity of the steric asymmetry seems to be apparent for the scattering into the highest J state, Ω = 3/2, J = 9/2, f, as also found for the OH + N_2 system. For the interpretation of these results we have taken into account the anisotropy and the topology of the interaction potential governing both inelastic and reactive collisions. The presence of a well corresponding to the van der Waals complex located at the O-side of OH and correlating with the transition state seems to play a role in the dynamics at this low collision energy. Moreover, from previous experimental and theoretical data we estimate that the collision energy of the present study should exceed the reaction barrier. The interference of reactions could also be used to explain the negative steric asymmetry obtained for the excitation into Ω = 3/2, J = 5/2, f state, as opposed to the positive value obtained for collisions of OH with CO for which the collisions at the H-side would lead to reactions via the OH-CO van der Waals complex correlating with the HOCO intermediate. The decrease in the negativity of the steric asymmetry for higher rotational excitation may indicate that reorientation effects may influence the dynamics at this collision energy.

The interpretation of our data in terms of the anisotropy of the PES indicates that the scattering dynamics at this collision energy (920 cm^{-1}) may be influenced by the HO--HCl van der Waals well and by reorientation effects determined by the long-range electrostatic forces and may as well involve reactive collisions. Additional experiments of the OH + HCl system concerning studies of reactive collisions and van der Waals complexes would be very useful in ascertaining the proposed explanations and understanding its dynamics. A reactive study at this low collision energy may seem very challenging, as the reactive cross sections are predicted to be quite small, but we expect it to be feasible by the application of the sensitive REMPI technique for the detection of the atomic reaction product. Furthermore, by extending the investigation of the system dynamics over a wider energy regime, one can establish the influence of the reorientation effects and the relative contribution of the reactive channel. Another way of verifying the interpretation proposed herein would be to perform similar inelastic scattering measurements involving the isotopomers of OH and/or HCl that will sample different regions of the respective potential energy surfaces involving higher reaction barriers due to the change in the zero point energy and possibly slightly more bound van der Waals complexes.

An important step in understanding the stereodynamics of this system at low collision energies can be made with the help of quasi-classical trajectories and quantum scattering calculations. For a meaningful comparison with experimental results, it is necessary to obtain inelastic and reactive cross sections using potential energy surfaces which include accurate descriptions of the van der Waals and the transition state regions.

Chapter 5

State-to-state inelastic scattering of OH ($^2\Pi_{3/2}$, v = 0, J = 3/2, f) by HCl, HBr and HI[§]

5.1 Introduction

The interaction of the hydroxyl radical with hydrogen halides is expected to play an important role in atmospheric chemistry, since the atomic halogen released by the reactive path can efficiently catalyze the ozone destruction in various layers of the atmosphere. Not all known so far, the molecular interaction potentials for OH – HX systems, with X = Cl, Br and I, determine the interplay between elastic, inelastic and reactive processes involved in collisions of these molecules. The present experimental study on the state-to-state inelastic scattering of the hydroxyl radical by collisions with a diatomic molecule joins previous work on the kinetics of the OH + HX reactions and on the computation at different levels of approximation of the Potential Energy Surface (PES) of these systems to reveal in more details the intermolecular interaction [13-39]. The inelastic collision channel is characterized by state-to-state cross sections for the rotationally inelastic scattered OH molecules. Due to the lack of complementary theoretical results, the measured relative cross sections are only mutually compared.

5.2 State-to-state relative cross sections

Using the experimental set-up described in **Chapter 2,** relative inelastic state-to-state cross sections have been measured for the scattering process: OH ($X\ ^2\Pi_{3/2}$, v = 0, J = 3/2, f) + HX ($^1\Sigma$, v = 0, J < 4)$\rightarrow$ OH ($X\ ^2\Pi$, v = 0, Ω', J', e/f) + HX, with Ω'= 3/2 and 1/2, corresponding to spin-orbit conserving and changing transitions, respectively, J' up to 11/2, and X = Cl, Br and I. The flux-to-density transformation is considered to have only a minor effect on the presented results at the present experimental accuracy and is not taken into account in the data analysis (see paragraph 2.4).

[§] adapted from: A. Moise, R. Cireasa, D.H. Parker and J.J. ter Meulen, J. Chem. Phys. 125, 204315 (2006); A. Moise, D.H. Parker and J.J. ter Meulen, J. Chem. Phys., 126, 124302 (2007)

As mentioned in paragraph 2.4, for each collision-induced transition (Ω", J", ε") → (Ω', J', ε') the relative state-to-state inelastic cross section is given by Eqs. (2.22)- (2.23):

$$\sigma_{rel}(\Omega',J',\varepsilon') = \frac{F_{in}(\Omega',J',\varepsilon')}{F_{out}(\Omega'',J'',\varepsilon'')} \cdot 100(\%), \tag{5.1}$$

$$F_{in}\ (\Omega',J',\varepsilon') \propto \int_{Det\,Vol} \sigma(\Omega',J',\varepsilon' \leftarrow \Omega'',J'',\varepsilon'') \cdot v_{relative} \cdot n_{OH} \cdot n_Y \cdot dV, \tag{5.2}$$

where F_{in} (Ω', J', ε') is the fluorescence signal due to the increase of the (Ω', J', ε') state population of OH by in-scattering, F_{out} (Ω", J", ε") is the decrease of the signal due to the OH molecules scattered out of the (Ω", J", ε") internal state, initially populated, n is the number density, $v_{relative}$ is the average relative velocity of the molecular beams and σ is the absolute inelastic cross section. By the scattering process the population of the initial state Ω"= 3/2, J"= 3/2, f is depleted by only 6 to 10%, ensuring single collision conditions. As given in Table 5.1, 62 - 81% of the scattered molecules are detected in different excited rotational states. The loss of population is due to inelastic and elastic scattering outside the probe area and possible reactive processes. Their total contribution is thus equal within the experimental accuracy for scattering by HBr and by HCl, while for HI the loss of population is larger. The removal of OH molecules by reactive scattering might give a larger contribution to the out-scattering for OH-HI compared to OH-HBr and OH-HCl, according to the reaction rates [13-20, 27-31, 34-39].

Table 5.1 *The mass of the collision partner of the OH molecule, the sum over the relative state-to-state cross sections involving all final internal states, the collision energy and the highest rotational state probed for OH-Y scattering, with Y = HCl, HBr and HI*

Y	HCl	HBr	HI
M_Y (a.m.u.)	36.5	81	128
$\sum_{\Omega',J',\varepsilon'} \sigma_{rel}(\Omega',J',\varepsilon')_{OH-Y}$ (%)	81 ± 2	80 ± 2	62 ± 2
$E_{coll\ OH-Y}$ (cm^{-1})	920	750	690
$(\Omega', J')_{max\ excitation}$	1/2, 7/2	3/2, 11/2	1/2, 7/2

The results for the relative inelastic state-to-state cross sections are listed in Table 5.2. By collisions the OH ($^2\Pi_{3/2}$, v = 0, J = 3/2, f) molecules are rotationally excited to both spin-orbit states $^2\Pi_{3/2}$ and $^2\Pi_{1/2}$, conserving or changing the state parity, or are slightly de-excited to the lower Λ-doublet state, (Ω'= 3/2, J'= 3/2, e), changing only the parity. In case of scattering by HBr the highest rotational energy state excited is (Ω'= 3/2 J'= 11/2), which is populated by a very small number of the scattered molecules, below 1%. For this case the conversion of the collision kinetic energy to rotational energy is 532 cm^{-1}, still bellow the total available energy. For the other collision systems the highest state populated is (Ω'= 1/2, J'= 7/2), corresponding to 417 cm^{-1} internal excitation. The collision induced Λ-doublet transition (parity changing), for which the energy change is only 0.055 cm^{-1}, presents the largest cross section.

Table 5.2 *Relative state-to-state cross sections, σ_{rel} (%), for inelastic collisions of OH with HCl, HBr and HI. The errors represent one standard deviation and were obtained by weighted statistical analysis.*

Final state			OH+HCl	OH+HBr	OH+HI
Ω'	J'	ε'			
3/2	3/2	e	55.36 ± 1.43	51.90 ± 0.88	41.67 ± 1.34
	5/2	e	6.28 ± 0.21	5.48 ± 0.52	4.76 ± 0.62
	5/2	f	6.48 ± 0.28	5.73 ± 0.35	6.21 ± 0.56
	7/2	e	1.76 ± 0.15	2.15 ± 0.40	1.71 ± 0.53
	7/2	f	1.75 ± 0.16	2.55 ± 0.31	2.46 ± 0.48
	9/2	e	0.49 ± 0.10	1.50 ± 0.39	0.38 ± 0.64
	9/2	f	0.82 ± 0.30	1.39 ± 0.34	0.81 ± 0.64
	11/2	f	-	0.62 ± 0.32	-
1/2	1/2	e	1.49 ± 0.08	1. 84 ± 0.24	0.96 ± 0.31
	1/2	f	1.47 ± 0.20	1.35 ± 0.27	0.32 ± 0.45
	3/2 & 5/2	e*	1.78 ± 0.12	2.45 ± 0.30	1.99 ± 0.44
	3/2	f	0.83 ± 0.08	1.47 ± 0.32	0.11 ± 0.37
	5/2	f	1.30 ± 0.24	0.90 ± 0.60	0.25 ± 0.42
	7/2	e	0.87 ± 0.10	0.78 ± 0.08	0.03 ± 0.63
	7/2	f	-	-	0.21 ± 0.61

**the measured cross section contains contributions from both 3/2 e and 5/2 e states as the absorption lines used to probe them could not be resolved within the laser bandwidth*

The large value of the relative cross section for the transition to the Ω'= 1/2, J'= 3/2 and 5/2 e states is due to the fact that it includes contributions from excitations to both rotational states, probed by transitions unresolved within the laser bandwidth. The measured cross section for the transition to the Ω'= 3/2, J' = 5/2, f final state has been corrected for the initial population of this state assuming that the out-scattering affects the population of the J = 3/2 and J = 5/2 states with the same percentage.

For a comparison of the OH-HX systems the ratios of the relative cross sections to the relative cross section for the transition to the Ω' = 3/2, J' = 3/2, e state are considered, as given by Eq. (4.1). Under the assumption that the product $v_{relative} \cdot n_{OH} \cdot n_Y$ (Eq. 5.2) is constant over the entire detection volume, the resulting ratios ρ (Ω', J', ε') are the ratios of the absolute inelastic state-to-state cross sections for the transition to each probed state and the absolute inelastic cross section for the transition to the Ω'= 3/2, J'= 3/2, e state. The ratios are shown graphically in Fig. 5.1 for the OH-HI system at 690 cm^{-1} collision energy, for OH-HBr at 750 cm^{-1} collision energy and for OH-HCl at 920 cm^{-1}.

Relative to the number of molecules that due to the collisions with HX (X = Cl, Br, I) change only the state parity, the amount of molecules rotationally excited decreases with increasing rotational quantum number and this trend is notable for all halogen hydride partners. The fact that the largest cross sections correspond to the lowest rotational excitations, indicates that collisions at large impact parameters dominate the inelastic scattering process. This can be related to the strong long-range electrostatic interaction for these systems containing molecules with large permanent electric moments, as shown in Table 5.3.

Table 5.3 *Molecular properties: mass, electric dipole moment, electric quadrupole moment and polarizability for OH, HCl, HBr and HI [70]*

HX	Mass (a.m.u.)	Dipole[a] (D)	Quadrupole[b] (D Å)	Polarizability[c] (Å^3)	Electronegativity[d] atom X
OH	17	1.66	1.4	1	3.44
HF	20	1.82	2.1	0.7	3.98
HCl	36.5	1.08	3.6	2.4	3.16
HBr	81	0.83	4.2	3.3	2.96
HI	128	0.38	6	6.7	2.66

[a] *experimental values*

[b] *calculated zz diagonal-term of the electric quadrupole moment tensor*

[c] *average of the calculated diagonal-terms of the polarizability tensor*

[d] *Pauling scale, in which the electronegativity is 2.20 for the H atom.*

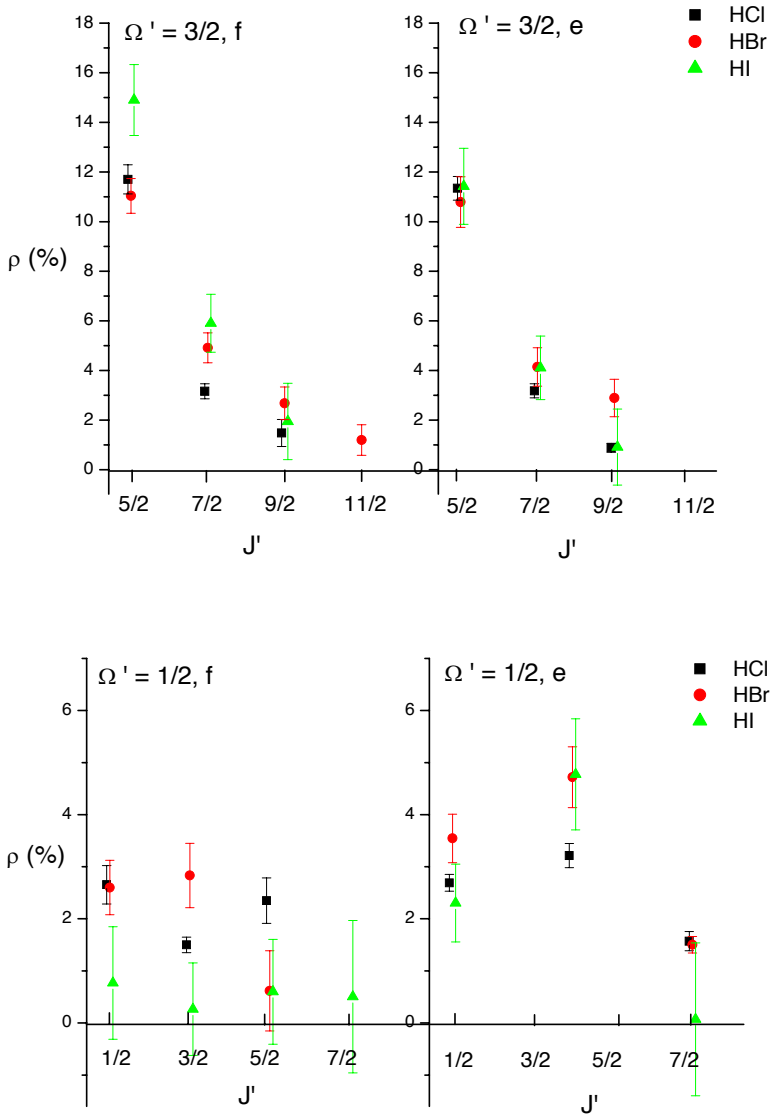

Fig. 5.1 *Ratios, ρ (Ω', J', ε') (%), of the absolute state-to-state inelastic cross sections and the absolute cross section for the transition to the Ω'= 3/2, J'= 3/2, e state of OH ($X\,^2\Pi$, v = 0, Ω"= 3/2, J"= 3/2, f) in collisions with HI at 690 cm^{-1} collision energy (triangles), with HBr at 750 cm^{-1} collision energy (circles), and with HCl at 920 cm^{-1} collision energy (squares), for the transitions to the Ω'=3/2 states – upper panel and to the Ω'= 1/2 states – lower panel.*

The cross sections for the spin-orbit conserving transitions decrease faster with rotational excitation for OH scattered by HI than for scattering by the other two halides. For the transitions changing the spin-orbit manifold and conserving the symmetry, i.e. Ω'= 1/2, f, the cross sections for OH-HI scattering are nearly zero. For this reason the corresponding steric asymmetries were not measurable. Within the experimental accuracy no propensity with respect to the symmetry is measured for OH-HCl and OH-HBr, while for OH-HI a propensity for the Ω'= 3/2, f and Ω'=1/2, e states is revealed, except for the Ω'= 3/2, J'= 7/2 state. The Ω'= 3/2, f and Ω'= 1/2, e states correspond to the electronic configuration with the unpaired electronic orbital antisymmetric with respect to a reflection in the molecular rotation plane. Obviously, in collisions with HI the OH molecules exhibit a tendency to retain this configuration above changing it into the orbital configuration symmetric with respect to a reflection in the molecular rotation plane. This might be related to the large difference in the intermolecular interactions involving the electric quadrupole moment and polarizability which are much larger for OH-HI than for the OH-HBr and OH-HCl systems, as reflected in Table 5.3. These interactions may differ for the two electronic configurations (orbital of unpaired electron in plane of rotation or perpendicular to it) resulting in such a symmetry propensity.

5.3 State-to-state steric asymmetries

The molecular collision dynamics are inherently influenced by the relative orientation of the collision partners. Along each interaction pathway, reactive, inelastic or elastic, the molecular system may have a variety of spatial configurations, which are determined by the balance of the Pauli exchange repulsive forces and the electro-magnetic forces. Favoring one configuration by molecular orientation prior to the collision, the outcome of the collision can be controlled to a certain extent. Angle-dependent barriers and cone of acceptance for product channels are frequently key-issues for various reactions. One of the methods employed to orient polar molecules in the laboratory frame is the use of weak homogeneous electric fields preceded by hexapole fields. The radial field of the hexapole focuses only the trajectories of molecules in a particular quantum state, creating the so-called molecular state selection and a local orientation. A subsequent weak homogeneous field is necessary in order to achieve the desired uniform orientation.

In this study the stereodynamical issues of the inelastic scattering of OH by HCl, HBr and HI are addressed. The experiments are performed in a crossed molecular-beam setup at collision energies of 920, 750 and 690 cm^{-1}, respectively. By means of static electrical fields, the OH reagent is selected in a single-quantum state, v" = 0, Ω"= 3/2, J"= 3/2, M_J"= 3/2, ε"= f, and is oriented with either the O-side or the H-side pointing towards the collision partner (Chapter 2).

Defined by Eq. (2.24), the steric asymmetry S is used to quantify the orientation effect on the scattering process. The steric asymmetries were measured as a function of the OH rotational excitation and Λ-doublet symmetry for the scattering into either spin-orbit manifolds.

The measured steric asymmetries corresponding to the OH-HCl, OH-HBr and OH-HI scattering are displayed in Table 5.4 and presented graphically in Fig. 5.2. Generally, for the spin-orbit changing transitions the experimental accuracies are lower and no clear trend with J' is observed. When comparing the steric asymmetries among all three OH-HX systems some particularities are notable. For the transitions to the Ω'= 3/2, J'= 5/2 and 7/2, f states, relatively large negative steric asymmetries are measured for OH-HCl whereas the steric asymmetries are nearly zero for OH-HBr and OH-HI. The experimental accuracy is lower for the results of OH-HI and except for the transitions to Ω'= 3/2, e states no major differences are notable in comparison with the steric asymmetries for the OH-HBr system. An increase of the steric asymmetries with decreasing cross sections can be identified.

Table 5.4. *Steric asymmetries, S (%), measured for inelastic collisions of OH with HCl, HBr and HI*

Final state			OH+HCl	OH+HBr	OH+HI
Ω'	J'	ε'			
3/2	5/2	e	3.0 ± 1.2	1.3 ± 2.8	8.2 ± 2.8
	5/2	f	–16.5 ± 1.6	2.6 ± 3.7	–1.2 ± 4.8
	7/2	e	–1.1 ± 3.5	1.0 ± 5.6	7.5 ± 5.9
	7/2	f	–21.3 ± 5.4	–4.1 ± 6.2	–0.5 ± 8.0
	9/2	e	18.8 ± 12.4	7.4 ± 10.9	-
	9/2	f	–5.3 ± 6.5	6.7 ± 9.2	-
	11/2	f	-	9.6 ± 7.0	-
1/2	1/2	e	6.7 ± 4.0	5.4 ± 5.6	1.6 ± 6.1
	1/2	f	–0.3 ± 3.7	–2.8 ± 6.8	-
	3/2 & 5/2	e*	7.1 ± 3.3	–0.7 ± 8.0	3.3 ± 6.7
	3/2	f	9.2 ± 8.6	–2.4 ± 7.4	-

** the measured steric asymmetry contains contributions from both 3/2 e and 5/2 e states as the absorption lines used to probe them could not be resolved within the laser bandwidth.*

Intuitively it seems more efficient to exert a large torque, needed for high rotational excitations, at the H-side, as it is farther from the center of mass. Therefore, for higher rotational excitations negative steric asymmetries are expected, as have been observed for OH-Ar. Except for the transitions to the Ω'= 1/2, f states this trend is not observed. In fact, the reverse trend is observed for spin-orbit conserving transitions. Considering the fact that the unfilled electron orbital is closer to the O atom one might expect a propensity for collisions involving the OH molecules oriented with the O-side towards the collision partner (positive S) for the transitions requiring spin-orbit or e/f symmetry changes of the OH internal state. The OH-HI scattering exhibits such positive steric asymmetries for the e/f state symmetry-changing transitions.

The differences in results for the OH inelastic scattering by HCl, HBr and HI molecules may be linked to the occurrence of reactions, in which case the different energy dependences of the reaction rate constants and the different vibration distribution of the H_2O product should be taken into account. The reported kinetic studies of the OH+HX reaction indicate large rate coefficients. Among the three HX halides, X = Cl, Br and I, the HI molecule is found to have the highest room temperature rate for the reaction with the OH radical, $2 \cdot 10^{-18}$-$7 \cdot 10^{-18}$ m^3 s^{-1}, and the highest reaction exothermicity [34-39]. The correlation between the bond energy of these halides and the rate constants for their reaction with the OH molecules indicates that the reactions proceed via H atom abstraction [38, 39]. Besides their size, the three mentioned halides differ also by their electric dipole moments, averaged quadrupole moments and polarizabilities (Table 5.3), and as a consequence, the OH-HX interaction potentials have different features that measurable quantities are expected to reflect. Indeed, Butkovskaya and Setser [38] measured by IR chemiluminescence the vibrational distribution of the H_2O product in a fast flow reactor at room temperature and found that 36% of the available energy of the OH + HI reaction is converted into vibrational excitation of the H_2O molecule, while for the OH + HBr reaction 61% of the available energy is transferred to the internal vibration energy of the water and no vibrational energy is found for the water product of the OH + HCl reaction [20, 38]. The energy disposal shows that the dynamics of these reactions are different. Besides the direct H atom abstraction an alternative mechanism is likely to occur, in which the OH radical initially attacks the halogen atom end of the H'X, after which the H' atom migrates to the oxygen atom and H_2O is formed [38].

Migration of a H atom has been observed for the H + FI → HF + I, H + FBr → HF + Br and H + FCl → HF + Cl reactions which give rise to microscopic branching, i.e. "direct" and "migratory" dynamics are present as distinct routes to the same reaction products [121, 122]. The migration of hydrogen from the vicinity of a halogen atom, I, Br, Cl, to a more electronegative one, F, was found to lead to a rotationally hotter HF product. A similar migration of the H' atom from a halogen to the O atom of the hydroxyl radical may lead to a higher population of the H_2O product in the bending mode.

Butkowskaya and Setser measured a fraction of energy into the bending mode relative to the total vibration energy of 0.30 for the water molecule produced by OH + HBr and 0.46 for H_2O produced by OH + HI, and correlated the increase of this fraction to the growing component of the addition-migration reaction mechanism [38].

The hydrogen atom migration mechanism requires an attack of the OH molecule with the H-side on the halogen part of the encountered hydride. However, in the configurations for the transition states and the most stable hydrogen bonded complexes, as derived by ab initio computations for OH-HCl [26] and OH-HBr [33], the H'-side of the halogen hydride is closer to the OH molecule, the H-O-H' bonds being very close to the stable water molecule geometry. The OH-HCl four-dimensional diabatic PES's, computed by Wormer et al and correlated with the two-fold $^2\Pi$ ground state of the hydroxyl radical, reveals besides the HO-H'Cl global minimum with a well depth of 1123 cm^{-1}, a local minimum with an energy well of 655 cm^{-1}, for which the molecular configuration is very different [26]. The Cl atom is approached by the hydroxyl radical forming an almost T shaped OH-ClH' complex. The bent configuration of the molecular system for this PES minimum indicates that the interaction based on the quadrupole electric moments is strong. If the configuration of this local minimum is the only one having the halogen atom towards the hydroxyl radical, it is probably close to the configuration required for the H' migration mechanism. It should be noted that going from HCl to HBr and HI the permanent electric dipole moment decreases and the quadrupole moment increases (Table 5.3) which would lead to a relatively deeper OH-XH' minimum, assuming a similar shape of the PES for OH-HBr and OH-HI. This would be consistent with an increasing competition between the direct and migration reaction mechanisms for OH + H'X reactions, going from X = Cl to Br and I, according to the conclusions of Butkowskaya and Setser. Indeed, Liu et al [33] found the HO-H'Br complex well almost two times less deep than the HO-H'Cl well and Deskevich et al [123] found the deepest well for HO-H'F, about 4000 cm^{-1}, where HF has the largest dipole moment and the lowest quadrupole moment among the electric moments of HX molecules, X= F, Cl, Br and I. It is thus possible that two complex wells are correlated to two reaction mechanisms that lead to the same products (microscopic branching) and that the branching ratios for the two channels are different for the OH+H'X systems, with X = Cl, Br, I [121, 122].

It is interesting that the configurations for the two potential wells exhibit different orientations of the molecules with respect to each other. The presence in the PES of two minima, one for the HO-H'X configuration and the other for an OH-XH' configuration, both related to the occurrence of the reaction, may determine small steric asymmetries. For the HCl case the global minimum is very deep when compared with the local one, thus the O-side is presumed to be preferred for sampling the HO-H'Cl well region, yielding strong anisotropy effects.

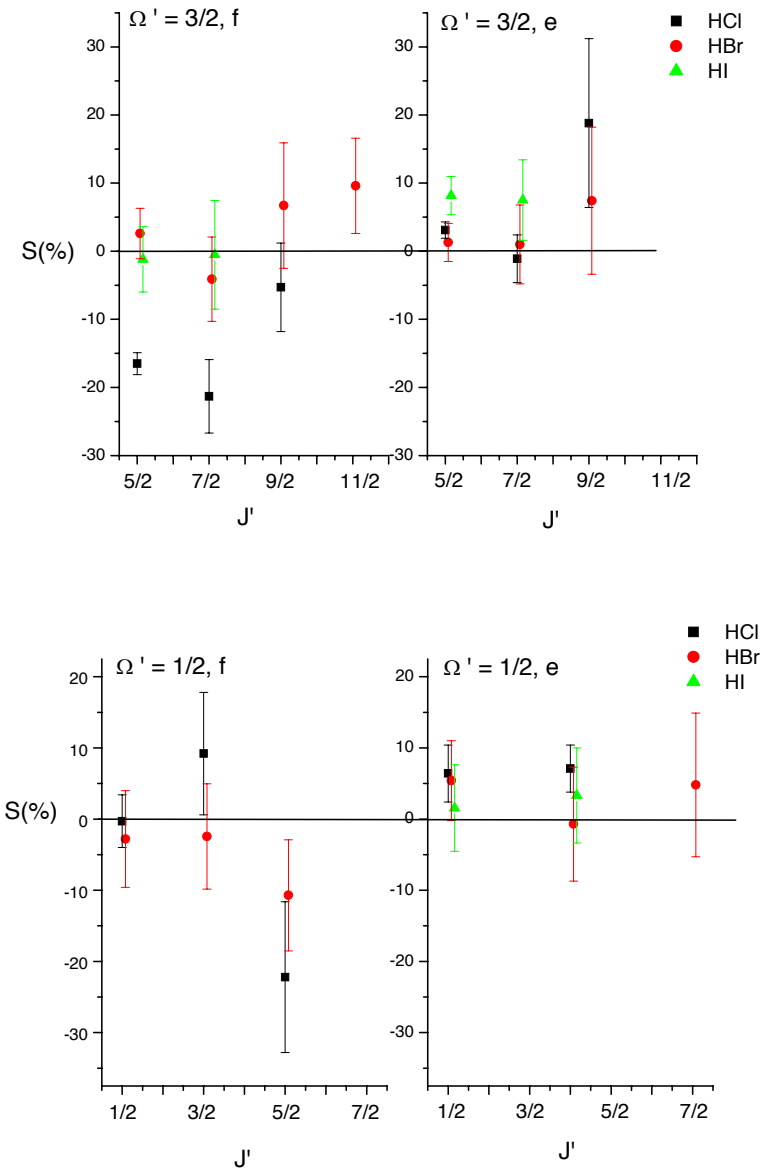

Fig. 5.2 *State-to-state steric asymmetries, S (%), for spin-orbit conserving transitions-upper panel and spin-orbit changing transitions-lower panel, for scattering of OH ($X\ ^2\Pi$, v= 0, Ω"= 3/2, J"= 3/2, f) by HI at 690 cm^{-1} collision energy (triangles), by HBr at 750 cm^{-1} collision energy (circles), and by HCl at 920 cm^{-1} collision energy (squares)*

This presumption can be confirmed by the negative steric asymmetries which indicate smaller inelastic cross sections for collisions involving the hydroxyl radical oriented with the O-side towards the HCl molecule compared to the cross sections for collisions of OH oriented with the H-side towards HCl, on the account of the losses due to reactions via the direct H atom abstraction. Such large negative steric asymmetries are observed for the spin-orbit and symmetry conserving transitions, $\Omega'= 3/2$, $J'= 5/2$ and 7/2, f, of OH molecules scattered by HCl (Fig. 5.2, upper panel). Thus, the-H side oriented molecules, sampling the region of the OH-H'Cl complex, prefer to conserve their initial state spin-orbit and symmetry, $\Omega'= 3/2$, f. For collisions with HBr and HI the second reaction mechanism, via the OH-XH' complex, may become important, in which case both the H and O side oriented molecules may be lost by reaction, resulting in smaller measured steric asymmetries. This is in agreement with the experimental results, which show almost no steric asymmetries for the OH scattering by HBr and HI (Fig. 5.2).

For the symmetry changing transitions, $\Omega'= 3/2$, e, (Fig. 5.2, upper panel) the steric asymmetries for OH-HI are small, but clearly positive. The relative state-to-state cross sections of these collision induced transitions are smaller than the cross sections for the transitions to the $\Omega'= 3/2$, f states (Table 5.4). The effect might be ascribed to the interaction involving the HI electric quadrupole moment and polarizability. Transitions to the $\Omega'= 3/2$, e states exhibit smaller cross sections and more positive steric asymmetries than transitions to $\Omega'= 3/2$, f, which means that fewer molecules are scattered to the e states and that in these collisions the O side orientation is preferred. This may be correlated to the losses by reaction via a H' migration mechanism, in which the second complex and the interaction due to the quadrupole electric moment are involved, if such reaction mechanisms indeed play a role for the OH + HI system.

Other possible effects on the measured steric asymmetries may be related to the occurrence of the exchange reaction, $OH + H'X \rightarrow OH' + HX$, and to OH reorientation. The exchange reactions for the interactions of hot H atoms with H'X molecules have larger cross sections and smaller energy barriers going from X = Cl, Br to I [124]. A decrease of the measured cross sections with rotational excitation is found faster for OH scattered by HI followed by HCl and HBr, but our measurements cannot give information about the branching ratio between an H exchange reaction and the translation-rotation energy transfer for the OH - H'X interactions. If an exchange reaction takes place it may influence the results for the steric asymmetries in the sense that possibly the H side is favored for the reaction, which would give a negative S. Weaker steric asymmetries can be found due to the possible reorientation of the OH molecules in the presence of the encountering polar molecule, as discussed in paragraph 4.3.

5.4 Conclusions

Rotationally inelastic state-to-state cross sections and steric asymmetries for the hydroxyl radical in collisions with hydrogen halides have been measured in a crossed molecular beam experiment. The differences in mass, size, electric moments and polarizability of the chlorine, bromine and iodine hydrides are reflected in the experimental results presented. A comparison among the three molecular systems points towards rich PES landscapes which are not yet completely explored.

The rotationally inelastic cross sections obtained indicate similarities among the OH-HCl, OH-HBr and OH-HI scattering systems. Generally, the spin-orbit conserving transitions dominate, the Λ-doublet transition exhibits the largest cross section and the magnitude of the cross sections decreases with the rotational excitation. The fastest decrease is found for the OH molecule scattered by HI and only for OH-HI a small preference for the A' symmetry states is observed.

The measured steric asymmetries reflect the higher anisotropy of the OH-HCl interaction potential. Small or almost no asymmetries are measured for the OH-HBr and OH-HI systems. A possible correlation between the magnitude or sign of the experimental steric asymmetries and the molecular configurations for the PES minima or the occurrence of a reaction is discussed. Findings from previous kinetic reports and improved calculations are used as support for a qualitative discussion of the anisotropy of the OH-HX (X = Cl, Br and I) interaction potentials.

Chapter 6

State-to-state inelastic scattering of OH ($^2\Pi_{3/2}$, v = 0, J = 3/2, f) by Xe

6.1 Theoretical background

The understanding of the mutual interaction of the diatomic molecule - atom systems constitutes an important step towards the study of larger systems. A high level of accuracy has been achieved for systems like OH-rare gas in computing the Potential Energy Surfaces, as confirmed by comparison with experimental results. The polar OH molecule exhibits dispersion and dipole-induced dipole interaction with the atoms from the rare gas family. Reflected in the depth of the PES wells the interaction strength is expected to increase with the polarizability of the rare gas from He to Xe as shown in Table 6.1. The PES's of the OH-He [44], OH-Ar [45] and OH-Xe [125] systems reveal minima in the range of 22 to 224 cm^{-1}. The effect of a larger polarizability on the well depth overcomes the effect of the size, which tends to expand the Pauli exchange repulsive region to larger interaction distances.

The interaction of a $^2\Pi$ diatomic molecule with an atom is described by two Potential Energy Surfaces, $V_{A'}$ and $V_{A''}$, corresponding to electronic states that are symmetric and anti-symmetric, respectively, with respect to the electronic reflection in the plane defined by the nuclei [57, 107]. Combinations of these two adiabatic potentials, as expressed in Eqs. (4.2) and (4.3), are more convenient for the scattering calculations. These potentials are functions of R, the distance between the atom and the center of mass of the molecule, r, the bond length of the molecule and θ, the angle between the vectors r and R, with θ = 0° and 180° for the collinear OH-atom and atom-OH configurations, respectively. Diagonal (v' = v") matrix elements, V_{sum} (R, θ) and V_{diff} (R,θ), obtained by integrating over r for the diatom vibration wave-functions coupled by the interaction of the diatomic molecule with the rare gas atom [57, 107], are expressed in Legendre polynomial expansions, as given by Eqs. (4.4) and (4.5).

In the approximation of a direct coupling of the initial and final states of the total atom-diatom system the cross section for the inelastic scattering is proportional to the square of the matrix element of the interaction potential, averaged over all distances R and all values of the quantum number for the orbital angular momentum of the atom, L, and the total angular momentum of the molecule-atom system, $\mathfrak{J}$ [107].

The matrix elements of the interaction potential which couple the internal states labeled ‘ and “ can be expressed as follows [107]:

$$\left\langle \Omega' J' \varepsilon' L' \Im \middle| V \middle| \Omega'' J'' \varepsilon'' L'' \Im \right\rangle = \sum_{l} f(\Im, J'', J', L'', L', l) \times \left[1 - \varepsilon' \varepsilon'' (-1)^{J'+J''+l} \right] \quad (6.1)$$
$$\times \left[A^{l}_{\Omega' J' \varepsilon', \Omega'' J'' \varepsilon''} V_{l0}(R) + B^{l}_{\Omega' J' \varepsilon', \Omega'' J'' \varepsilon''} V_{l2}(R) \right].$$

The magnitude and the sign of the f, A and B coefficients determine to which extent different V_{l0} and V_{l2} radial terms of the potential contribute to the potential matrix element.

In Table 6.2 are given the matrix elements for the OH-atom interaction potential corresponding to the coupling of the initial state, characterized by Ω”= 3/2, J”= 3/2 and ε”= f for the OH molecules and L”= 0 for the atom, with the final state, characterized by the quantum numbers: Ω’, J’, ε’and L’. As shown in Table 6.2, final states conserving the parity (p’= +) are coupled by the potential matrix elements involving the even *l* terms of the expansion of V_{sum} and V_{diff} and the states changing the parity (p’ = -) are coupled by the potential matrix elements involving the odd *l* terms of the potentials expansion. A possible propensity for transitions to the e symmetry Ω’= 3/2 final states may be attributed to the positive interference by the contributions of V_{l0} and V_{l2} terms with the same sign, while for transitions to the Ω’= 3/2 f final states a negative interference may reduce the cross sections by the contribution of V_{l0} and V_{l2} terms with different sign.

Table 6.1 *Mass and polarizability of He, Ar and Xe and total inelastic cross section for scattering of OH (Ω”= 3/2, J”= 3/2, ε”= f) by He, Ar and Xe*

Rare gas	Mass (a.m.u.)	Polarizability[a] (10^{-30} m^3)	Global PES minimum (cm^{-1})	$\sum_{\Omega'J'\varepsilon'} \sigma(\Omega'J'\varepsilon' \leftarrow \Omega''J''\varepsilon'')$ (10^{-20} m^2)	at E_{coll}(cm^{-1})
He	4	0.2	-30[b]	10.71[e]	394
Ar	40	1.6	-147[c]	32.64[f]	746
Xe	131	4.0	-224[d]	55[g]	630

[a] *ref. [77]*
[b] *ref. [44]*
[c] *ref. [45]*
[d] *ref. [125]*
[e] *ref. [126]*
[f] *ref. [43]*
[g] *ref. [127]*

Generally, for open shell molecule Hund's case (a) interacting with an atom the V_{l0} terms dominate the spin-orbit conserving transitions and the V_{l2} potential terms dominate the spin-orbit changing transitions. The OH molecules approach the (a) case for low rotational states.

6.2 Results and discussion

6.2.1 State-to-state cross sections

Table 6.3 shows the measured relative state-to-state cross sections (Eq. 2.22-2.23) and steric asymmetries (Eq. 2.24) for OH-Xe scattering at 630 cm^{-1} collision energy.

Table 6.2 *The matrix elements of the OH-atom potential interaction for Ω" = 3/2, J" = 3/2, ε"= f , p"= + and L"= 0*

Final state				
Ω'	J'	ε'	p'	$\langle V \rangle$ [a]
3/2	3/2	e	-	$-0.44 \cdot V_{10} - 0.05 \cdot V_{30}$
	3/2	f	+	$-V_{00} - 0.19 \cdot V_{20} + 0.10 \cdot V_{22}$
	5/2	e	+	$0.31 \cdot V_{20} + 0.1 \cdot V_{22} + 0.06 \cdot V_{40} + 0.01 \cdot V_{42}$
	5/2	f	-	$0.37 \cdot V_{10} + 0.18 \cdot V_{30} - 0.08 \cdot V_{32}$
	7/2	e	-	$-0.22 \cdot V_{30} - 0.1 \cdot V_{32} - 0.06 \cdot V_{50} - 0.02 \cdot V_{52}$
	7/2	f	+	$-0.24 \cdot V_{20} + 0.05 \cdot V_{22} - 0.16 \cdot V_{40} + 0.08 \cdot V_{42}$
	9/2	e	+	$0.21 \cdot V_{40} + 0.1 \cdot V_{42} + 0.05 \cdot V_{60} + 0.02 \cdot V_{62}$
	9/2	f	-	$0.18 \cdot V_{30} - 0.06 \cdot V_{32} + 0.14 \cdot V_{50} - 0.08 \cdot V_{52}$
1/2	1/2	e	+	$-0.04 \cdot V_{20} + 0.28 \cdot V_{22}$
	1/2	f	-	$-0.06 \cdot V_{10}$
	3/2	e	-	$0.1 \cdot V_{10} - 0.04 \cdot V_{30} - 0.2 \cdot V_{32}$
	3/2	f	+	$0.07 \cdot V_{20} + 0.27 \cdot V_{22}$
	5/2	e	+	$-0.07 \cdot V_{20} + 0.16 \cdot V_{22} - 0.05 \cdot V_{40} + 0.16 \cdot V_{42}$
	5/2	f	-	$-0.03 \cdot V_{10} - 0.07 \cdot V_{30} - 0.23 \cdot V_{32}$
	7/2	e	-	$0.06 \cdot V_{30} - 0.16 \cdot V_{32} + 0.05 \cdot V_{50} - 0.14 \cdot V_{52}$
	7/2	f	+	$0.02 \cdot V_{20} + 0.06 \cdot V_{22} + 0.08 \cdot V_{40} + 0.20 \cdot V_{42}$

[a] *ref. [56, 107]*

In order to diminish the presence of Xe clusters in the beam, the measurements are performed at 800 mbar backing pressure, conditions at which less than 4% of the OH molecules are out-scattered by collisions. Consequently, the signal-to-noise ratio is poor. Out of the maximum 4% scattered molecules from the Ω"= 3/2, J"= 3/2, f state, (55 ± 5) % are detected in different rotational states. As shown in Table 6.3 the transitions conserving the state parity, p' = p" = +, exhibit larger cross sections than the transitions changing the state parity. This propensity for parity conservation is present for almost all rotational states probed and indicates that the even *l* terms of the Legendre expansion of the potential dominate the odd *l* terms.

Table 6.3 *State-to-state cross sections, σ_{rel} (%), and steric asymmetries, S (%), for inelastic collisions of OH (Ω"= 3/2, J"= 3/2, ε"= f, p"= +) with Xe at 630 cm^{-1} collision energy.*

Final state					
Ω'	J'	ε'	p'	σ_{rel} (%)	S (%)
3/2	3/2	e	-	33.70 ± 1.88	-
	5/2	e	+	8.64 ± 1.57	–6.7 ± 3.8
	5/2	f	-	2.07 ± 1.47	18.6 ± 10.0
	7/2	e	-	0.03 ± 1.50	-
	7/2	f	+	1.25 ± 0.89	5.2 ± 10.2
	9/2	e	+	3.37± 1.52	-
	9/2	f	-	0.03 ± 1.35	-
1/2	1/2	e	+	0.85 ± 0.88	–5.7 ± 11.1
	1/2	f	-	0.03 ± 1.33	-
	3/2 & 5/2	e*		1.17 ± 1.25	-
	3/2	f	+	2.05 ± 0.96	-
	5/2	f	-	0.11 ± 1.11	-
	7/2	e	-	0.03 ± 1.26	-
	7/2	f	+	1.42 ± 1.55	-

** the measured cross section contains contributions from both 3/2 e and 5/2 e states as the absorption lines used to probe them could not be resolved within the laser bandwidth*

Figure 6.1 shows the measured absolute state-to-state cross sections for the OH (Ω"= 3/2, J"= 3/2, ε"= f) + Xe scattering system in comparison with the corresponding theoretical results [125]. The values are scaled such that the sums of the cross sections over all final internal states are equal for the experiments and for the theoretical results. Relative to the corresponding theoretical cross sections the experimental cross sections for the e/f symmetry changing transitions, $\Delta\Omega = 0$ with $\Delta J = 0$ and 3 are larger, while all the other cross sections are smaller within the experimental accuracy. The decrease of the measured cross sections with the rotational excitation and the propensity for the spin orbit-conserving transitions are in general agreement with the calculations. For the spin-orbit changing transitions the experimental error bars are larger, but the general trends follow the theoretical ones. The measured value of the cross section for the transition to the Ω'= 1/2, J'= 3/2 and 5/2 e states includes contributions from excitations to both rotational states, probed by transitions unresolved.

It should be mentioned that the present results are in less good agreement with theory than the values obtained by Gilijamse and coworkers [125]. They measured the state-to-state cross sections for transitions to Ω'= 3/2, J'= 3/2 e and 5/2 e and f as well as to Ω'= 1/2, J'= 1/2 e as a function of collision energy up to 380 cm^{-1}. The reason for this discrepancy is not yet clear. A possible explanation cannot be the presence of dimers in the beam, that are well known to form easily in the case of Xe, since the backing pressure for our experiments is about three times lower than the pressure in the experiment by Gilijamse and coworkers.

For a comparison of the various OH-rare gas systems Fig. 6.3 presents the measured cross sections for the OH-He [42], OH-Ar [43] and OH-Xe scattering, scaled with theoretical results. For the scattering of OH by Xe the decrease of the state-to-state inelastic cross sections with the internal excitation is similar to the energy-gap law behavior noticed for the OH-HX molecular systems, with X = Cl, Br and I, for which the electric dipole-dipole and dipole-quadrupole interactions are dominant (Fig. 5.1). However, the decrease of the state-to-state cross sections with internal excitation is not monotonous for OH scattered by He and Ar. Since the Helium atom has a very small polarizability the quantum nature forces dominate the interactions of this atom. Argon and Xenon experience a stronger dispersion and dipole-induced dipole interaction with the polar OH molecule. This interaction strength is reflected in the magnitude of the total calculated inelastic cross section and in the depth of the potential wells, as shown in Table 6.1.

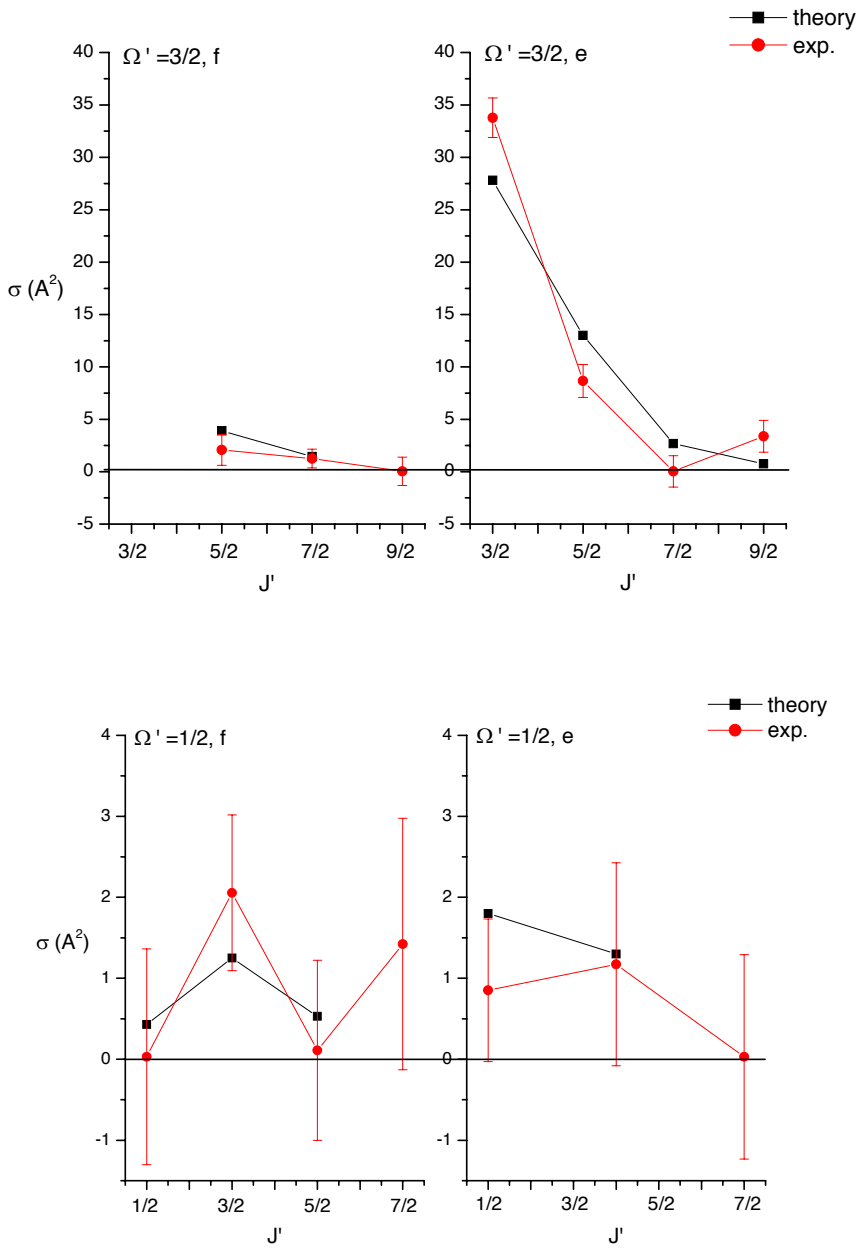

Fig. 6.1 *State-to-state cross sections for OH ($X^2\Pi$, v=0, Ω"= 3/2, J"= 3/2, f) scattering by Xe at 630 cm^{-1} collision energy for the transitions to Ω'= 3/2 states – upper panel and Ω'=1/2 states - lower panel*

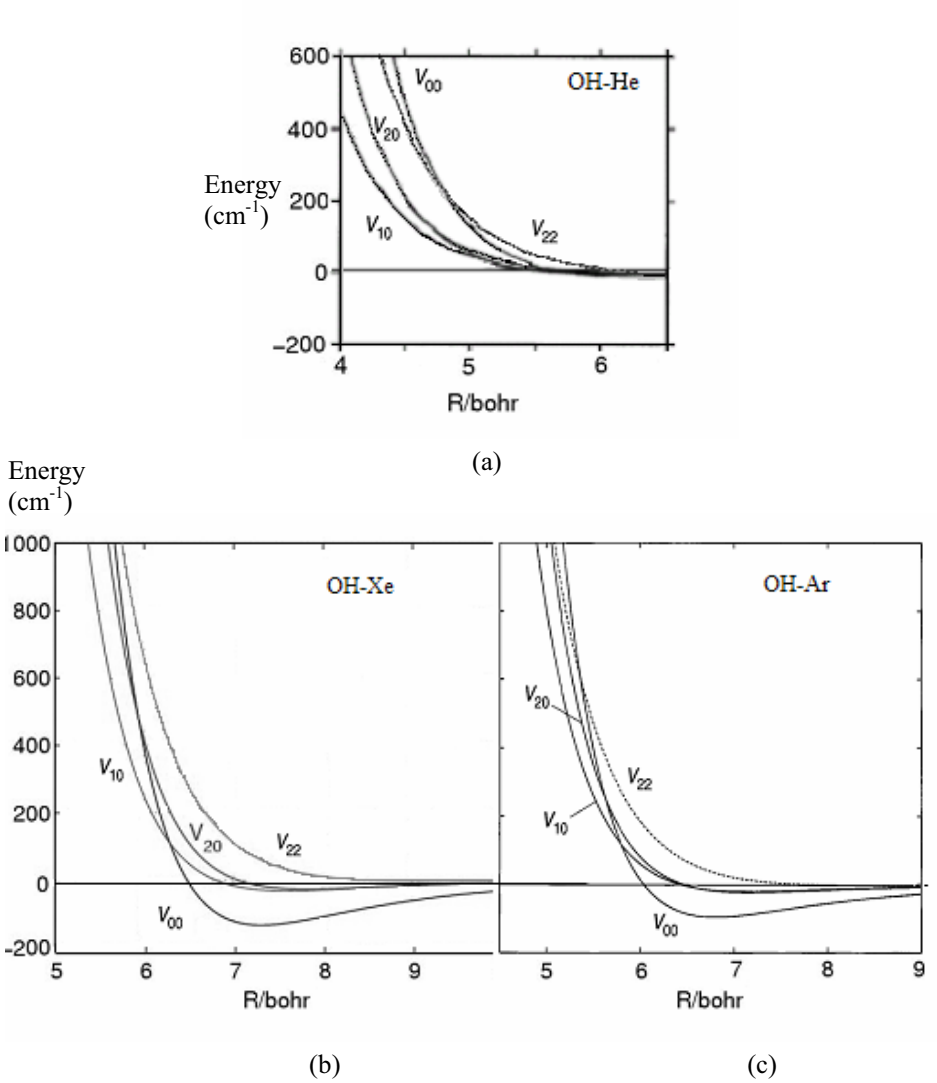

Fig. 6.2 *Radial V_{l0} and V_{l2} terms of the Legendre expansion of the potential for OH-He [126] (a), OH-Ar [45] (b), and OH-Xe [127] (c)*

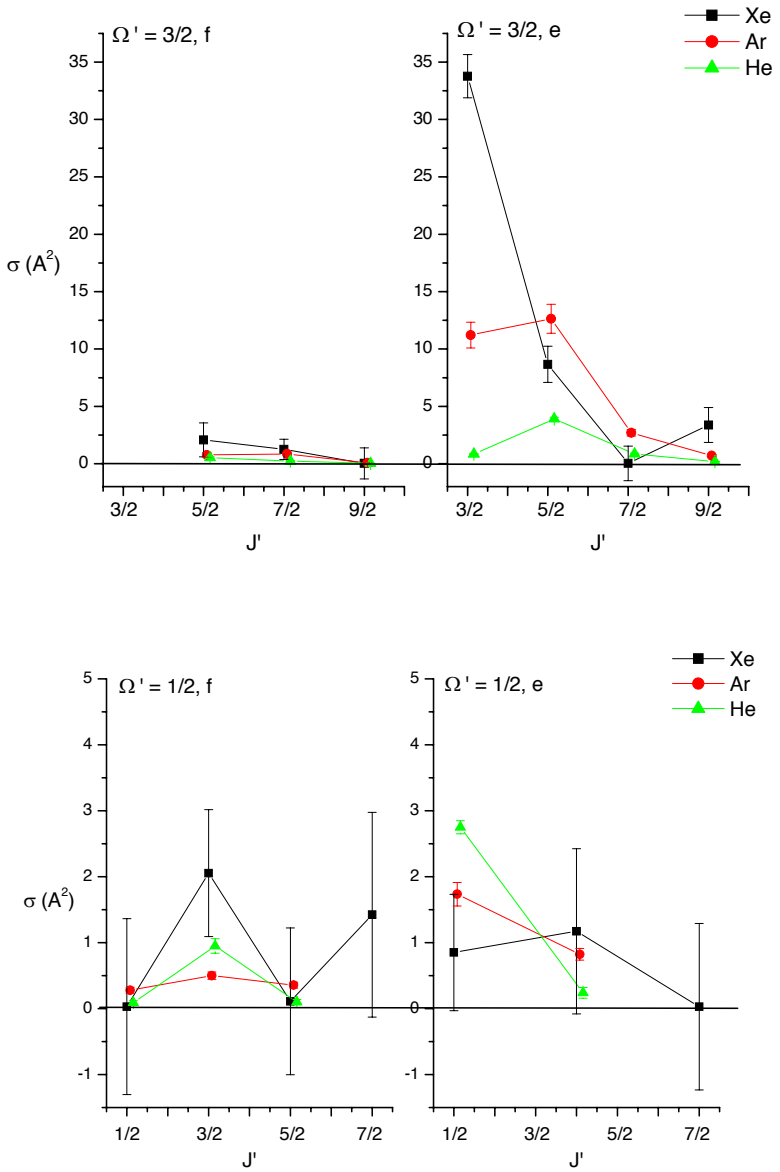

Fig 6.3 *State-to-state cross sections for scattering of OH ($X^2\Pi$, v = 0, Ω''= 3/2, J''= 3/2, f) with He at 451 cm^{-1} collision energy (triangles [a]), with Ar at 746 cm^{-1} collision energy (circles [b]), and with Xe at 630 cm^{-1} collision energy (squares), for the transitions to the Ω'= 3/2 states - upper panel and to the Ω'= 1/2 states - lower panel.*
[a] from Ref. [42]; [b] from Ref. [43]

Figure 6.2 illustrates that, for all mentioned OH-rare gas interactions, the V_{l0}(R) functions are positive at short values of R and small but negative at large R, while the V_{l2} (R) functions are positive at all R ranges. The V_{22} potential exhibits the strongest repulsive behavior, while the V_{00} and V_{10} have significant attractive parts. The most attractive potential term is V_{00} for OH-Xe with a minimum of about -130 cm^{-1} at R $\approx$ 7.2 bohr [127]. This suggests that the elastic scattering cross section is the largest for the OH-Xe collisions in comparison with OH-Ar and OH-He collisions. The cross sections for the transition to the Ω'= 3/2, J' = 3/2 e state indicate that going from He to Ar and Xe as OH collision partners the contribution to the interaction of the V_{10} term becomes more important. It is very likely that the magnitude of V_{10} contribution increases with the polarizability of the rare gas and that this term is correlated to the dipole-induced dipole interaction (in Eq. (6.3) $d^1_{00} = \cos\theta$). Similarly, the cross sections for the transition to the Ω'= 1/2, J' = 1/2 e state indicate that the repulsive V_{22} term is more significant for the OH interaction with He than with Ar and Xe.

6.2.2 State-to-state steric asymmetries

Steric asymmetry measurements have been reported before for the scattering of OH by He, Ar, *n*-H_2, and *p*-H_2 [54]. Subsequently, orientation effects were obtained for OH–CO and OH–N_2 with improved detection sensitivity [56]. The availability of high quality *ab initio* potential-energy surfaces (PES's) enabled a joint experimental and theoretical study of the OH-Ar system [63]. The agreement of the experimental steric asymmetries with those obtained by quantum scattering calculations, as depicted in Fig. 6.4, illustrates the great potential of inelastic-scattering experiments in assessing the accuracy of the PES employed.

As a measure of the orientation effect on the scattering process, the steric asymmetry S as given by Eq. (2.24), indicates by a positive value the preference for scattering at the O side of the OH molecule and by a negative value, an H side preference. The measured state-to-state steric asymmetries for OH-Xe scattering are listed in Table 6.3 and shown graphically in Fig. 6.4 together with the corresponding results from OH-Ar system [63] for comparison. For the experiments on OH-Xe scattering, only few collision induced transitions could be characterized with a steric asymmetry. This is due to a poor signal to noise ratio as a consequence of the low Xe backing pressure used in order to reduce the presence of Xe clusters in the molecular beam.

As can be seen in Fig. 6.4, a clear propensity is present in collisions with Ar to induce a higher internal excitation to the OH molecules when H is the side of the impact with the Ar atom (negative S).

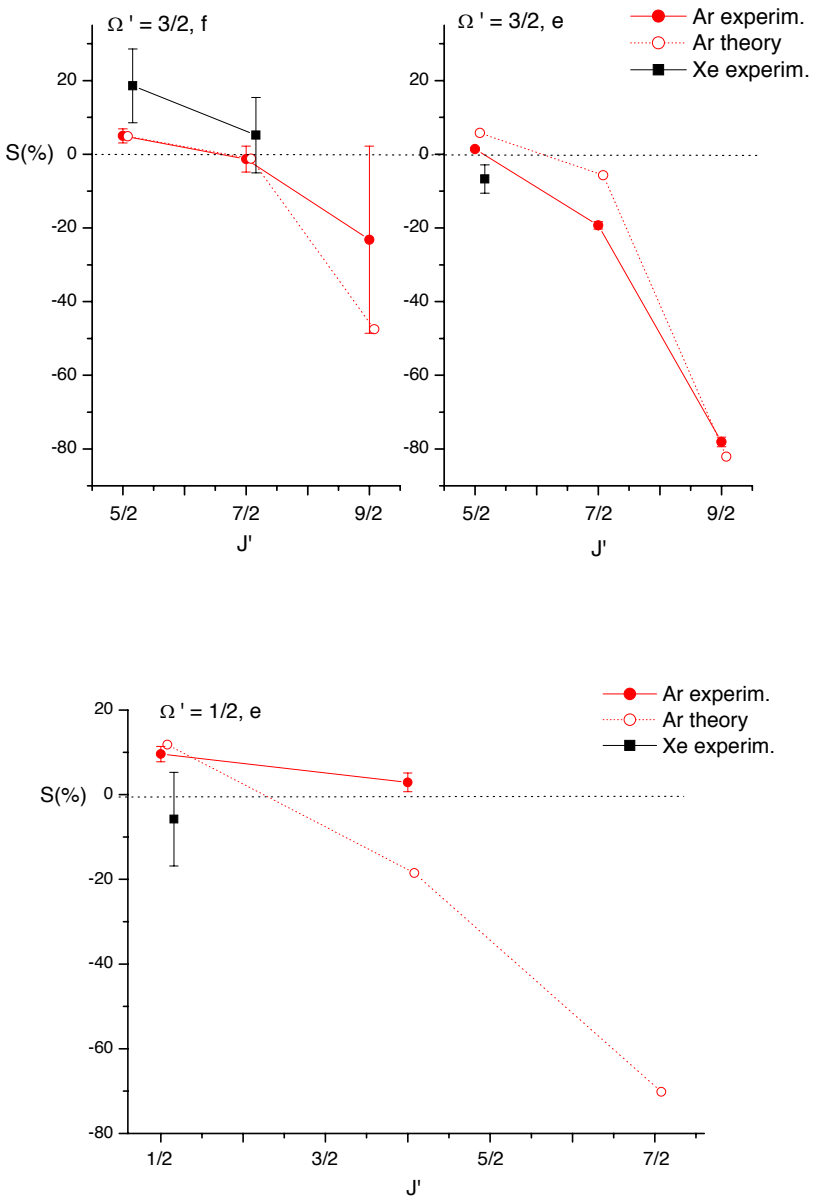

Fig 6.4 *State-to-state asymmetries for scattering of OH ($X\,^2\Pi$, v=0, Ω''= 3/2, J''= 3/2, f) with Ar at 746 cm^{-1} collision energy (circles [a]), and with Xe at 630 cm^{-1} collision energy (squares), for the transitions to the Ω'=3/2 states - upper panel and to the Ω'=1/2 states - lower panel*

[a] from Ref. [63]

Also the observed asymmetries for Xe collisions indicate that the O-side impact becomes less favored with increasing internal excitation of the scattered OH molecule. A classical ball-and-stick model matches this behavior: rotation and torque can easier be exerted at the lightest part of the molecule. Such preferences for the collisions with the H side may be linked to the global minima of the $V_{A''}$ PES for OH-Ar and OH-Xe, which are both found for the linear O-H-atom configuration ($\theta = 0°$), as shown in Table 6.4. The OH scattering into the $\Omega' = 3/2$, $J' = 5/2$, $\varepsilon' = f$ final state manifests a clear preference for the collisions of both Ar and Xe with the O side oriented OH molecules ($\theta = 180°$). This preference is stronger for Xe. The OH collision induced transition to the $\Omega' = 3/2$, $J' = 5/2$, $\varepsilon' = f$ final state probes the part of the interaction potential involving the V_{10} and V_{30} terms (Table 6.2). These terms multiply the $d^1_{00} = \cos\theta$ and $d^3_{00} = 0.2 \cdot \cos\theta \cdot (3 - 5\sin^2\theta)$ angular dependencies of the $V_{A''}$ potential, as shown in Eq. (6.3), describing the head-tail symmetry of the interaction with respect to the OH molecule. Thus a larger steric asymmetry S ($\Omega' = 3/2$, $J' = 5/2$, $\varepsilon' = f$) for scattering by Xe than for scattering by Ar may imply that the terms V_{10} and/or V_{30} are stronger for OH-Xe interaction than for OH-Ar, which is in agreement with the results from the unoriented scattering, discussed in the previous paragraph of this chapter. The OH-Xe system exhibits a larger difference between the steric asymmetries for the collision-induced transitions to the two Λ-doublet components of the same final rotational state $\Delta\Omega = 0$, $\Delta J = 1$.

6.3 Conclusions

Rotationally inelastic state-to-state cross sections and steric-asymmetries for the hydroxyl radical scattered by Xe are presented. The experimental state-to-state cross sections are considered in comparison with theoretical results and with the experimental results for the OH-He, OH-Ar and OH-Xe systems. Both theory and experiment reveal a propensity for spin-orbit conserving transitions and a decrease of the cross sections with rotational excitation.

The experimental cross sections indicate a smaller propensity for changing the state symmetry than predicted by theory, and a propensity for the conservation of parity instead. A comparison with the OH-He and OH-Ar systems may reflect the differences in mass, size and polarizability of the three rare gases. Changing the OH collision partners from He to Ar and Xe the decrease of the cross section with rotational excitation is more monotonous and the e symmetry propensity is reduced.

Table 6.4 *Values of the energy, E, for global and local minima of the $V_{A'}$ and $V_{A''}$ PES's for the OH-Ar and OH-Xe interaction and the atom-O-H angle, θ, for the corresponding configurations. $\theta = 0$ corresponds to the linear OH-atom configuration.*

System	$V_{A'}$		$V_{A''}$	
	E(cm^{-1})	θ	E(cm^{-1})	θ
OH + Ar[a]	-147	0°	-147	0°
	-136	75°	-96	180°
OH + Xe[b]	-224	90°	-200	0°
	-200	0°	-100	180°

[a] *ref [45]*
[b] *ref. [125]*

The values of the state-to-state cross sections are correlated with the contribution to the interaction of various radial terms of the potential Legendre expansion, V_{l0} and V_{l2}. A dominance of the even *l* terms over the odd *l* radial terms of the OH-Xe interaction potential is shown in the propensity for parity conserving transitions and the contribution of the V_{10} term is reflected in the very large cross section for the Λ-doublet transition. The magnitude of the cross section for this transition seems to increase with the polarizability of the OH collision partner.

As for the extensively studied OH-Ar system, the few values measured for the state-to-state steric asymmetries characterizing the OH-Xe scattering tend to confirm the classical trend: the higher the internal excitation, stronger the preference for collisions with the lighter side of the OH molecule. The asymmetries for the two Λ-doublet transitions to Ω = 3/2, J = 5/2 differ by (25 ± 11) % for the OH-Xe system and only by (3.6 ± 1.9) % for OH-Ar. Values of the asymmetry for more transitions and theoretical results are needed to complete the comparison.

References

[1] G.P. Brasseur, J. J. Orlando, G. S. Tyndall, Atmospheric Chemistry and Global Change, Oxford University Press (1999)

[2] P. Warneck, Chemistry of the Natural Atmosphere (2nd Ed.), Academic Press (2000)

[3] R.P. Wayne, Chemistry of Atmospheres (3rd Ed.), Oxford University Press (2000)

[4] J.H. Seinfeld, S.N. Pandis, Atmospheric Chemistry and Physics - From Air Pollution to Climate Change (2nd Ed.), John Wiley and Sons, Inc. (2006)

[5] C.J. Rhodes, Toxicology of the Human Environment - the critical role of free radicals, Taylor and Francis, London (2000)

[6] N.A. Cohen, Revised Model for Transition State Theory Calculations for Rate Coefficients of OH with Alkanes, Aerospace Report No. ATR-90(7179)-1 (1990)

[7] W.B. DeMore, S.P. Sanders, D.M. Golden, R.F. Hampson, M. J. Kurylo, C.J. Howard, A.R. Ravishankara, C.E. Kolb, M.J. Molina, Chemical Kinetics and Photochemical Data for Use in Stratospheric Modeling, Evaluation No. 12, JPL Publication 97-4; Jet Propulsion Laboratory: Pasadena, CA (1997)

[8] J. Warnatz and W.C.Jr, Gardiner, Combustion Chemistry, Ed. Springer-Verlag, New York (1984)

[9] NIST Chemical Kinetics Database: NIST Standard Reference Database 17 (www.kinetics.nist.gov)

[10] J.W. Hewitt, F. Yusef-Zadeh, M. Wardle, D.A. Roberts and N. E. Kassim, Astrophys. J. 652 (2), 1288 (2006)

[11] M. Wardle, F. Y. Zadeh, Science 28, Vol. 296. no. 5577, 2350 (2002)

[12] H. Weaver, D. Williams, N. Dieter, W. Lum, Nature 208, 29 (1965)

[13] M.J. Molina, L.T. Molina, C.A. Smith, Int. J. Chem. Kinet. 16, 1151 (1984)

[14] L.F. Keyser, J. Phys. Chem. 88, 4750 (1984)

[15] D. Husain, J.M.C. Plane, C.C. Xiang, J. Chem. Soc. Faraday Trans. 2 (80), 713 (1984)

[16] A.R. Ravishankara, P. Wine, J.R. Wells, R.L. Thompson, Int. J. Chem. Kinet.17, 1281 (1985)

[17] Ian W. M. Smith and M.D. Williams, J. Chem. Soc. Faraday Trans.2 (82), 1043 (1986)

[18] P. Sharkey and I.W.M. Smith, J. Chem. Soc. Faraday Trans. 2 (89), 631 (1993)

[19] F. Battin-Leclerc, I.K. Kim, R.K. Talukdar, R.W. Portmann, A.R. Ravishankara, R. Steckler, D. Brown, J. Phys. Chem. A103, 3237 (1999)

[20] N.I. Butkovskaya and D.W. Setser, J. Chem. Phys. 108, 2434 (1998)

[21] D. Clary, G. Nyman, E. Hernandez, J. Chem. Phys. 101(5), 3704 (1994)

[22] R. Steckler, G. M. Thurman, J.D. Watts, R.J. Bartlett, J. Chem. Phys. 106(10), 3926 (1997)
[23] H.G. Yu and G. Nyman, J. Chem. Phys. 113 (20), 8936 (2000)
[24] A. Rodriguez, E. Garcia, M.L. Hernandez, A. Laganà, Chem. Phys. Lett. 360, 304 (2002)
[25] A. Rodriguez, E. Garcia, M.L. Hernandez, A. Laganà, Chem. Phys. Lett. 371, 223 (2003)
[26] P.E.S. Wormer, J.A. Kłos, G.C. Broeneboom and A. vad der Avoird, J. Chem. Phys. 122, 244325 (2005)
[27] I.R. Sims, I. W. M. Smith, D. C. Clary, P. Bocherel and B.R. Rowe, J. Chem. Phys. 101 (2), 1748 (1994)
[28] D.B. Atkinson, V.I. Jamarillo and M.A. Smith, J. Phys. Chem. A 101, 3356 (1997)
[29] A.R. Ravishankara, P.H. Wine and J.R. Wells, J. Chem. Phys. 83 (1), 447 (1985)
[30] Y. Bedjanian, V. Riffault, G. Le Bras and G. Poulet, J. Photochem. Photobiol. A: Chemistry 128, 15 (1999)
[31] N. I. Butkovskaya and D. W. Setser, J. Phys. Chem. 100, 4853 (1996)
[32] B. Nizamov, D.W. Setser, H. Wang, G.H. Peslherbe and W.L. Hase, J. Chem. Phys. 105 (22), 9897 (1996)
[33] J. Y. Liu, Z. S. Li, Z. W. Dai, X. R. Huang and C.C. Sun, J. Phys. Chem. A, 105(32), 7707 (2001)
[34] M. E. Jenkin, R. A. Cox, A. Mellouki, G. Le Bras and G. Poulet, J. Phys. Chem. 94, 2927 (1990)
[35] H. Mac Leod, C. Balestra, J. L. Jourdain, G. Laverdet and G. Le Bras, Int. J. Chem. Kin. 22 (11), 1167 (1990)
[36] G. A. Tacaks and G. P. Glass, J. Phys. Chem. 77, 1948 (1973)
[37] I. T. Lancar, A. Mellouki and G. Poulet, Chem. Phys. Lett. 177, 554 (1991)
[38] N.I. Butkovskaya and D.W. Setser, J. Chem. Phys. 106 (12), 5028 (1997)
[39] P. Campuzano-Jost and J.N. Crowley, J. Phys. Chem. A. 103, 2712 (1999)
[40] A. Gijsbertsen, H. Linnartz, C.A. Taatjes and S. Stolte, J. Am. Chem. Soc. 128, 8777 (2006) and references therein
[41] D.H. Parker, K.K. Chakravorty and R.B. Bernstein, Chem.Phys. Lett. 86 (2), 113 (1982)
[42] K. Schreel, J. Schleipen, A. Eppink and J.J. ter Meulen, J. Chem. Phys. 99, 8713 (1993)
[43] M.C. van Beek, J.J. ter Meulen and M.H. Alexander, J. Chem. Phys. 113, 628 (2000)

[44] H.S. Lee, A.B. McCoy, R.R. Toczylowski and S.M. Cybulski, J. Chem. Phys. 113 (14), 5736 (2000)
[45] J.A. Kłos, G. Chalasinski, M.T. Berry, R.A. Kendall, R.B. Burcl, M.M. Szczesniac and S.M. Cybulski, J. Chem. Phys. 112 (11), 4952 (2000)
[46] T. Kasai, private communication
[47] D.R. Miller, Atomic and Molecular Beam Methods, Vol. I, edited by G. Scoles (Oxford University Press, 1988)
[48] K. Schreel and J.J. ter Meulen, J. Chem. Phys. 101, 7639 (1997)
[49] J.I. Steinfeld, Molecules and Radiation: An Introduction to Modern Molecular Spectroscopy, 2nd edition (MIT Press, 1986)
[50] G. Herzberg, Spectra of Diatomic Molecules (Van Nostrand, Princeton, 1968)
[51] G.H. Dieke and H.M. Crosswhite, J. Quant. Spectrosc. Radiat. Transfer 2, 97 (1962)
[52] J. Luque and D.R. Crosley, LIFBASE: Database and Spectral Simulation Program, Version 1.9, (www.sri.com/psd/lifbase)
[53] R.N. Zare, Angular Momentum: Understanding Spatial Aspects in Chemistry and Physics (John Wiley & Sons, New York, 1988)
[54] P.F. Bernath, Spectra of Atoms and Molecules (Oxford University Press, New York, 1995)
[55] K. Schreel and J.J. ter Meulen, J. Chem. Phys. 105, 4522 (1996); K. Schreel, State to state cross-sections for collisions of state selected and oriented OH (PhD Thesis, Katholieke Universiteit Nijmegen, 1998)
[56] M.C. van Beek, Orientation effects in non-reactive collisions of OH (PhD Thesis, Katholieke Universiteit Nijmegen, 2001)
[57] M.H. Alexander, J. Chem. Phys. 76, 5974 (1982); Chem. Phys. 92, 337 (1985)
[58] J.J. ter Meulen, W.A. Majewsi, W.L. Meerts and A. Dymanus, Chem. Phys. Lett. 94, 25 (1983)
[59] W. L. Meerts and A. Dymanus, Chem. Phys. Lett. 23, 45 (1973)
[60] T. D. Hain and T.J. Curtiss, J. Chem. Phys. A 102, 9696 (1998)
[61] J. Reuss, Atomic and Molecular Beam Methods, Vol. I, edited by G. Scoles (Oxford University Press, 1988)
[62] R. Anderson, J. Phys. Chem. 101, 7664 (1997)
[63] M.C. van Beek, J.J. ter Meulen and M.H. Alexander, J. Chem. Phys. 113, 637 (2000)
[64] J. van Leuken, J. Bulthuis, S. Stolte and J. G. Snijders, Chem. Phys. Let. 260, 595 (1996)
[65] M. de Lange et al. J. Chem. Phys. 121, 11691 (2004); Chem. Phys. Lett. 313, 491 (1999)

[66] R.T. Jongma, Th. Rasing and G. Meijer, J. Chem. Phys. 102, 1925 (1995)
[67] D.R. Guyer, L. Huwel and S.R. Leone, J. Chem. Phys. 79, 1259 (1983)
[68] H.W. Cruse, P.J. Dagdigian and R.N. Zare, Farad. Discuss. Chem. Soc. 55, 277 (1973)
[69] R.G. Macdonald and K. Liu, J. Chem. Phys. 91, 821 (1989)
[70] NIST Computational Chemistry Comparison and Benchmark DataBase (http://srdata.nist.gov/cccbdb/); S.V. Churakov and M. Gottschalk, Geochimica et Cosmochimica Acta 67 (13), 2397, 2003
[71] D.H. Parker, Laser Ionization and Mass Spectrometry, in Ultrasensitive Laser Spectroscopy (Ed. D. S. Kliger, Academic Press, 1983)
[72] M.N.R. Ashfold and J.D. Howe, Multiphoton Spectroscopy of Molecular Species, Annu. Rev. Phys. Chem. 45, 57 (1994)
[73] G.S. Hurst, M.G. Payne, S.D. Kramer and J.P. Young, Rev. Modern Phys., 41 (4), 767 (1979)
[74] V.S. Letokhov, Laser Photoionization Spectroscopy (Academic Press, New York, 1986)
[75] M.V. Ashikhmin, Yu.E. Belyaev, A.V. Demyanenko, E.A. Ryabov and V.S. Letokhov, Chem. Phys. Lett. 227, 343 (1994)
[76] D.H. Parker, Velocity Mapping Studies of Molecular Photodissociation and Photoionization Dynamics, in Photoionization and Photodetachment, Advanced Series in Physical Chemistry, Vol 10A and 10B (World Scientific Publishing Co.Ltd. Singapore, 2000)
[77] NIST Chemistry WebBook: NIST Standard Reference Database (http://webbook.nist.gov/chemistry)
[78] H. Okabe, Photochemistry of Small Molecules (John Wiley & Sons, 1978)
[79] P.M. Regan, S.R. Langford, A. J. Orr-Ewing and M.N.R. Ashfold, J. Chem. Phys. 110 (1), 281 (1999)
[80] Y. Xie, P.T.A. Reilly, S. Chilukuri and R. Gordon, J. Chem. Phys. 95 (2), 854 (1991)
[81] P.J. Dagdigian, D.F. Varley, R. Liyanage, R.Gordon and R.W. Field, J. Chem. Phys. 105 (23), 10251 (1996)
[82] T. Spigliani, D. Chandler and D.H. Parker, Chem. Phys. Lett. 137 (5), 414 (1987)
[83] R. Liyanage, P.T.A. Reilly, Y. Yang and R. Gordon, Chem. Phys. Lett. 216, 544 (1993)
[84] IUPAC Subcommittee for Gas Kinetic Data Evaluation (http://www.iupac-kinetic.ch.cam.ac.uk/)
[85] R. Callaghan and R. Gordon, J. Chem. Phys. 93 (7), 4624 (1990)

[86] R.G. Bray and R.M. Hochstrasser, Mol. Phys. 31, 1199 (1976)
[87] J. Nieman and R. Naaman, Chem. Phys. 90, 407 (1984)
[88] K. Imura, T. Kasai, H. Ohoyama, H. Takahashi and R. Naaman, Chem. Phys. Let. 259, 356 (1996)
[89] K. Norwood, G. Luo and C.Y. Ng, J. Chem. Phys. 90 (9), 4689 (1989)
[90] A. Rauk and D. A. Armstrong, J. Phys. Chem. A, 104 (32), 7651 (2000)
[91] A.S. Pine and J. Howard, J. Chem. Phys. 84 (2), 590 (1986)
[92] Z. Latajka and S.Scheiner, Chem. Phys. 216, 37 (1997)
[93] S. Minemoto, H. Tanji and H. Sakai, J. Chem. Phys. 119 (15), 7737 (2003)
[94] J.A. Baker, R.O. Watts, J.K. Lee, T.P. Schafer and Y.T. Lee, J. Chem. Phys. 61, 3081(1974)
[95] R.D. Levine and R.B. Bernstein, Molecular Reaction Dynamics and Chemical Reactivity (Oxford University Press, 1987)
[96] F. Dong, S.H. Lee and K. Liu, J. Chem. Phys. 115, 1197 (2001)
[97] C.R. Vidal, Tunable Lasers, edited by I.F. Mollenhauer and J.C. White, Topics Appl. Phys. 59 (Springer-Verlag, 1987) and references therein
[98] R. Hilbig and R. Wallenstein, Comments At. Mol. Phys, 18, 4, 157 (1986)
[99] A. Lago, G. Hilber and R. Wallenstein, Phys. Rev. A 36, 8, 3827 (1987)
[100] H. Scheingraber and C.R. Vidal, IEEE J. Quant. Electr. QE-19, 12, 1747 (1983)
[101] N.P. Lockyer and J.C. Vickerman, Laser Chem. 17, 139 (1997)
[102] R. Mahon, T.J. McIlrath, V.P. Myerscough and D. Koopman, IEEE J. Quant. Electr. QE-15, 6, 446 (1979)
[103] Y.M. Yiu, T.J. McIlrath and R. Mahon, Phys. Rev. A 20, 6, 2470 (1979)
[104] D.F. Heath and P.A. Sacher, Appl. Optics, 5 (6), 937 (1966)
[105] J.A. Kłos, J. Aoiz, R. Cireasa and J.J. ter Meulen, Phys. Chem. Chem. Phys. 6, 4368 (2004)
[106] M.C. van Beek, K. Schreel and J.J. ter Meulen, J. Chem. Phys. 109, 1302 (1998)
[107] P.J. Dagdigian, M.H. Alexander and K. Liu, J. Chem. Phys. 91 (2), 839 (1989)
[108] M.I. Lester, B.V. Pond, D.T. Anderson, L.B. Harding, A.F. Wagner, J. Chem. Phys. 113, 9889 (2000); M.I. Lester, B.V. Pond, M.D. Marshall, D.T. Anderson, L.B. Harding, A.F. Wagner, Faraday Discuss. Chem. Soc. 118, 373 (2001)
[109] K. Kudla, A.G. Koures, L.B. Harding, G.C. Schatz, J. Chem. Phys. 96, 7465 (1992)
[110] H.-G. Yu, J.T. Muckerman, T.J. Sears, Chem. Phys. Lett. 353, 578 (2001)
[111] M.C. van Beek and J.J. ter Meulen, J. Chem. Phys. 115, 1843 (2001)

[112] G. Lendvay, Abstr. Pap. - Am. Chem. Soc. 218, 202 (1999)
[113] D. Skouteris, D.E. Manolopoulos, W. Bian, H.-J. Werner, L.-H. Lai, K. Liu, Science 28, 1713 (1999)
[114] M.J. Lakin, D. Troya, G.C. Schatz, L. B. Harding, J. Chem. Phys. 119, 5848 (2003)
[115] R. Valero, D. A. McCormack, G.-J. Kroes, J. Chem. Phys. 120, 4263 (2004)
[116] M. I. Lester, R. A. Loomis, R. L. Schwartz, S. P. Walch, J. Phys. Chem. A101, 9195 (1997); M. D. Marshall, B. V. Pond, S. M. Hopman, M. I. Lester, J. Chem. Phys.114, 7001 (2001)
[117] P. Andresen, G.S. Ondrey, B. Titze, E.W. Rothe, J. Chem. Phys. 80, 2548 (1984)
[118] B.V. Pond and M.I. Lester, J. Chem. Phys. 118, 2223 (2003)
[119] R. B. Bernstein and R. D. Levine, J. Phys. Chem. 93, 1687 (1989)
[120] G. C. Groenenboom and A. J. H. M. Meijer, J. Chem. Phys. 101, 7592 (1994)
[121] D. Brandt and J.C. Polanyi, Chem. Phys. 45, 65 (1980)
[122] D. Brandt and J.C. Polanyi, Chem. Phys. 35, 23 (1978)
[123] M. P. Deskevich, D. J. Nesbitt and H. J. Werner, J. Chem. Phys. 120 (16), 7281 (2004)
[124] P.M. Aker, G.J. Germann, K.D. Tabor and J. J. Valentini, J. Chem. Phys. 90 (9), 4809 (1989)
[125] J.J. Gilijamse, S. Hoekstra, S.Y.T. van de Meerakker, G.C. Groeneboom and G. Meijer, Science, 313, 1617 (2006)
[126] A.D. Esposti, A. Berning and H.J. Werner, J. Chem. Phys. 103 (6), 2067 (1995)
[127] G.C. Groenenboom, private communication

Summary and outlook

Gas phase studies of the interaction between two individual particles ranging in size from atoms and diatoms to large bio-molecules, contribute to the understanding of many complex phenomena taking place in the chemistry of planets and interstellar space, at solid-surfaces and in gas or liquid environments. Models involving different levels of theory give information about the interaction potential energy of the two molecules as a function of inter-nuclear distances and angles of relative orientation of the constituent atoms. Calculations based on such models predict measurable quantities that can be compared with experimental results.

The interaction of the OH radical with atoms and other molecules is relevant for many physical and chemical processes involved in atmospheric, combustion and interstellar chemistry. Various experimental and theoretical studies have revealed information concerning the interaction of the hydroxyl radical with rare gas atoms like He, Ar, Ne and molecules like H_2, N_2, CH_4, CO and CO_2. A remarkably good agreement between the theoretical and experimental results was obtained for the OH-Ar inelastic scattering, confirming thus the accuracy of the theoretical models.

In this thesis crossed molecular beams experiments are presented in which the scattering of OH molecules by HCl, HBr, HI and Xe is studied. State-to-state cross sections and steric asymmetries are measured which probe the complete Potential Energy Surfaces (PES) for these atom-diatom or diatom-diatom systems. The experimental techniques employed are: supersonic molecular beam expansions, an electrical discharge to produce the hydroxyl radicals, hexapole electrostatic fields to focus and select the OH molecules in a single internal energy state (the upper of the two Λ-doublet states of the lowest rotational state, i.e. f symmetry), laser induced fluorescence to probe the population of the OH molecules which are excited by collisions, and resonance enhanced multiphoton ionization and velocity map imaging for the detection of the halogen hydrides and of the reactive scattering products. Moreover, electrostatic fields obtained by four pair-wise biased parallel-rods are used to orient the molecules with the H-side or the O-side towards the collision partner. This enables the acquisition of the most detailed information on the anisotropy of the potential energy surface.

1. The OH – Halogen Hydrides interaction

Large cross-sections and exothermicities are predicted for the reactions of hydrogen halides with the hydroxyl radical. Produced directly or through CH_3X intermediates by oceans, volcanoes emissions, biomass burning or industry, the halogen compounds play an important role in the atmospheric chemistry. For example, they may catalyze processes leading to the destruction of ozone.

Measurements performed in flow reactor experiments provide thermal rates of the OH + HX reactions, with X = Cl, Br and I, for large temperature ranges. For these reactions the rates at room temperature and the exothermicity increase with the size of the halogen. Features of the PES's indicate strongly bound van der Waals complexes mainly due to interactions based on the electric moments. Our experiments probe both inelastic and reactive channels at well defined collision and internal energy and specific orientations of the OH molecule. The quantities measured are the relative state-to-state cross sections and the steric asymmetries, which account for the effect of the OH orientation on these cross sections.

The rotational inelastic cross sections obtained indicate similarities among the OH-HCl, OH-HBr and OH-HI scattering systems. Generally, the spin-orbit conserving transitions dominate, the Λ-doublet transition exhibits the largest cross-section and the magnitude of the cross-sections decreases with rotational excitation. The fastest decrease is found for OH scattered by HI and only for this system a small preference for symmetry conserving transitions is observed.

The measured steric asymmetries reflect the higher anisotropy of the OH-HCl interaction potential. Small steric asymmetries are measured for OH-HBr and OH-HI. A possible correlation between the magnitude and sign of the experimental steric asymmetries with the molecular configurations for the PES minima and the occurrence of the reactions is discussed.

Reaction products were not detectable under the given experimental conditions, due to too low sensitivity and a high background signal. Detection methods involving laser ionization at photon energy outside the absorption ranges of the halogen hydrides or laser induced fluorescence should be considered. Enhancement of the OH beam density by relaxing the internal state purity condition or by an alternative OH production method is also recommended. Knowledge of the differential inelastic and reactive cross sections and in particular the probing of the complex intermediates will strongly contribute to a detailed understanding of these interactions.

2. The OH- Rare Gas interaction

A wealth of theoretical and experimental studies aiming at the understanding of the OH-rare gas interaction has been reported. This concerns mainly the OH-Ar and OH-He systems. In this work state-to-state inelastic cross sections and steric asymmetries for the OH molecule scattered by Xe are presented. The experimental results are compared with the theoretical results and with the previously reported results for OH-He and OH-Ar scattering. Major differences are observed. Radial terms in the Legendre expansion of the interaction potential are correlated to the relative magnitude of the cross sections for collision-induced transitions to various OH internal states. Such a correlation points to an increased dominance of the V_{10} term with the polarizability and size of the rare gas collision partner for OH. This V_{10} term is likely to reflect the strength of the dipole - induced dipole interaction. The long-range interaction forces are expected to be stronger for the OH-Xe interaction than for OH-He and OH-Ar, due to the larger size and polarizability of the Xe atoms. Indeed, for OH-Xe scattering the largest rotational inelastic cross sections are found for the lowest rotational excitations which are induced mostly by collisions at largest impact parameters. A similar strong decrease of the inelastic cross-section with rotational excitation is observed for OH scattered by polar molecules. The large e symmetry propensity and the dominance of the V_{22} and V_{20} radial terms, revealed for the OH-Ar and OH-He interactions, might be ascribed to the shorter-range forces of quantum mechanical nature.

An explanation for the deviations between the experimental and the theoretical state-to-state cross sections for OH-Xe inelastic scattering is not yet available. Therefore, a more detailed theoretical exploration of the OH-rare gas interaction and of the contribution to this interaction of each type of the intermolecular forces would be needed.

Samenvatting

Gasfase studies naar de interactie tussen twee individuele deeltjes, die variëren in grootte van atomen en diatomen tot grote biomoleculen, dragen bij aan het begrip van veel complexe fenomenen zoals die welke plaats vinden in de chemie van de interstellaire ruimte en de aardatmofeer, aan oppervlakten van vaste stoffen, in plasma's en in gas- of vloeistofomgevingen. Modellen met verschillende theoretische diepgang geven informatie over de interactie energie van twee moleculen als functie van inter-nucleaire afstanden en de onderlinge oriëntatie van de atomen in beide moleculen. Berekeningen gebaseerd op zulke modellen voorspellen meetbare grootheden zolas botsingsdoorsnedes en reactiesnelheid, die vergeleken kunnen worden met experimentele resultaten.

De interactie van het OH (hydroxyl) radicaal met andere atomen en andere moleculen en met atomen is relevant voor menig fysisch en chemisch proces in de atmosfeer, in verbrandingsprocessen en in de interstellaire ruimte. Verschillende experimentele en theoretische studies hebben informatie opgeleverd over de interactie tussen het hydroxyl radicaal en edelgasatomen, zoals He, Ar en Ne en moleculen zoals H_2, N_2, CH_4, CO and CO_2. Een opmerkelijk goede overeenkomst tussen theoretische en experimentele resultaten werd gevonden voor inelastische OH-Ar botsingen, waarmee de nauwkeurigheid van de huidige theoretische berekeningen aan intercaties van open-schil diatomen met atomen werd aangetoond.

In dit proefschrift worden de resultaten beschreven van onderzoek aan de interactie van OH moleculen met waterstofhalogenen, HCl, HBr en HI en met Xe, waarbij gebruik is gemakt van gekruiste moleculaire bundels. Botsingsdoorsnedes en sterische asymmetrieën zijn gemeten, die een maat zijn voor het complete Potentiële-Energie Oppervlak (PEO) van deze atoom-diatoom of diatoom-diatoom systemen. De experimentele technieken die hierbij zijn toegepast zijn: supersonische moleculaire-bundelexpansie, een elektrische ontlading om hydroxyl radicalen te produceren, elektrostatische velden om de OH moleculen te focuseren en in één enkele interne energietoestand (de hoogste Λ-doublet toestand van de laagste rotationele toestand) te selecteren, laser-geïnduceerde fluorescentie detectie om de bezetting van de OH moleculen vóór en na de botsingen te meten, en resonantie-versterkte multi-foton ionisatie en snelheidsprojectie voor de detectie van de waterstofhalogenen en van de reactieve verstrooiingsproducten. Verder is een elektrostatische veld gebruikt om de OH moleculen met de H- of met de O-kant te oriënteren in de richting van de botsingspartner. Dit maakt het mogelijk om de meest gedetailleerde informatie over de anisotropie van het potentiële-energie oppervlak te verkrijgen.

OH – waterstofhalogeen interacties

Grote botsingsdoorsnedes en exothermiciteiten worden voorspeld voor de reacties tussen waterstofhalogenen en het hydroxyl radicaal. De watersofhalogenen, direct of via CH_3X tussenproducten geproduceerd door oceanen, vulkanische emissie, verbranding van biomassa of emissie door de industrie, spelen een belangrijke rol in de atmosferische chemie. Zij kunnen, bijvoorbeeld, processen katalyseren die leiden tot de afbraak van ozon.

Metingen uitgevoerd in stromingsreactor-experimenten leveren reactiesnelheiden voor OH + HX reacties, met X = Cl, Br and I, binnen grote temperatuurbereiken. Voor deze reacties nemen de reactiesnelheiden (bij kamertemperatuur) en de exothermiciteit toe met de grootte van het halogeen. Eigenschappen van de PEO's wijzen op sterk gebonden van der Waalscomplexen grotendeels als gevolg van interacties gebaseerd op elektrische multipoolmomenten. In onze experimenten kunnen zowel inelastische als reactieve processen worden besturdeerd bij goed gedefinieerde botsings- en interne energieën en bij specifieke oriëntaties van het OH molecuul. De gemeten grootheden zijn de relatieve botsingsdoorsnedes voor overgangen naar specifieke interne energietoestanden en de sterische asymmetrieën hiervan, die volgen uit het effect van de OH oriëntatie op deze botsingsdoorsnedes.

De verkregen rotationeel-inelastische botsingsdoorsnedes wijzen op overeenkomsten tussen de OH-HCl, OH-HBr and OH-HI systemen. In het algemeen, domineren de spin-baan behoudende overgangen, vertoont de Λ-doublet overgang de grootste botsingsdoorsnede en neemt de grootte van botsingsdoorsnedes af met rotationele excitatie. De snelste afname is gevonden bij botsingen tussen OH en HI en alleen voor dit systeem wordt een kleine voorkeur voor overgangen met een behoud van symmetrie gevonden.

De gemeten sterische asymmetrieën tonen een grotere anisotropie van de OH-HCl interactiepotentiaal. Voor OH-HBr en OH-HI zijn kleine sterische asymmetrieën gemeten. Mogelijke correlaties tussen de grootte en het teken van de gemeten sterische asymmetrieën met de voorspelde moleculaire structuren in de PEO minima en het optreden van reacties worden besproken.

Reactieproducten waren niet meetbaar bij de gegeven experimentele condities, waarschijnlijk als gevlog van een te lage gevoeligheid en een hoog achtergrond signaal. Detectiemethoden, zoals laserionisatie bij een fotonenergie buiten het absorptiebereik van de waterstofhalogenen of laser-geïnduceerde fluorescentie zouden moeten worden overwogen. Versterking van de OH-bundeldichtheid, ten koste van de interne toestandszuiverheid of door verbeteren van de OH-produktiemethode, is ook aan te raden.

Kennis van de inelastische en reactieve botsingsdoorsnedes en in het bijzonder het aantonen van complexe tussenprodukten zal sterk bijdragen aan het gedetailleerde begrip van deze interacties.

De OH- edelgas interactie

Een grote hoeveelheid van theoretische en experimentele studies van OH-edelgas interacties is gepubliceerd. Dit betreft hoofdzakelijk OH-Ar en OH-He. In aanvulling hierop worden in dit werk worden inelastische botsingsdoorsnedes en sterische asymmetrieën voor het OH molecuul in botsingen met Xe gepresenteerd. De experimentele resultaten worden vergeleken met theoretische berekeningen aan dit systeem en met eerder beschreven resultaten voor OH-He en OH-Ar botsingen. Grote verschillen zijn gevonden. De relatieve grottes van de botsingsdoorsnedes voor overgangen naar verschillende OH interne toestanden zijn gecorreleerd aan de radiële termen van de Legendre expansie van de interactiepotentiaal. Deze correlatie wijst op een toename van de dominatie van de V_{10} term met de polariseerbaarheid en grootte van de edelgas botsingspartner van OH. Deze V_{10} term wordt waarschijnlijk grotendeels bepaald door de grotte van de dipool-geïnduceerde dipool interactie. Deze lange-afstands interactie wordt verwacht sterker te zijn voor OH-Xe dan voor OH-He and OH-Ar, vooral vanwege de grotere polariseerbaarheid van Xe. Voor OH-Xe worden inderdaad de grootste inelastiche botsingsdoorsnedes gevonden voor de laagste rotationele excitaties, die grotendeels geïnduceerd worden door botsingen bij grote impact parameters. De waargenomen sterke afname van de inelastische botsingsdoorsnedes met rotationele excitatie is eerder gezien bij OH in intercatie met polaire moleculen. De grote voorkeur voor overgangen naar toestanden met *e*-symmetrie en de overheersing van de V_{20} en V_{22} radiële termen, zoals gemeten voor OH-Ar en OH-He, kunnen worden toegeschreven aan interacties op de kortere afstand die van meer kwantummechanische aard zijn.

Een verklaring voor de afwijkingen tussen experimentele en theoretische botsingsdoorsnedes voor de OH-Xe inelastische verstrooiing is nog niet beschikbaar. Een meer gedetailleerde theoretische verkenning van de OH-edelgas interactie en van het grotte van ieder type van de inter-moleculaire krachten in deze interactie zal hieraan kumnen bijdragen.

Rezumat

Studiul in faza gazoasa intercatiei dintre doua particule, variind in marime de la atomi si molecule diatomice pana la bio-molecule mari, contribuie la intelegerea multor complexe fenomene chimice cum ar fi care au loc in spatiul cosmic si in atmosfera terestra, la suprafata solidelor ori in diferite medii gazoase sau lichide. Modelele teoretice dau informatii despre energia potentiala de interactie a doua molecule, in functie de distanta dintre nuclee si orientarea relativa a atomilor constituienti. Calcule bazate pe asemenea modele prezic marimi masurabile, precum sectiuni eficace sau rate de reactie, care pot fi comparate cu rezultatele experimentale.

Interactia radicalului OH (hidroxil) cu atomi sau alte molecule detine un rol important in multe procese fizico-chimice din atmosfera, combustie si mediul cosmic. Numeroase studii teoretice si experimentale au avut ca obiect interactia radicalului hidroxil cu gaze rare, precum He, Ar si Ne, si alte molecule, precum H_2, N_2, CH_4, CO si CO_2. Un remarcabil acord intre rezultatele teoretice si experimentale au fost obtinute pentru imprastierea inelastica OH-Ar, confirmand astfel nivelul de precizie al calculelor teoretice legate de interactia cu atomi a moleculelor diatomice cu invelis electronic incomplet.

In aceasta lucrare sunt prezentate rezultatele studiului intercatiei moleculelor OH cu hidruri halogenate, HCl, HBr si HI, si cu Xe in fascicule moleculare. Au fost masurate sectiunile eficace integrale si asimetriile sterice corespunzatoare moleculelor OH in stari de energie interna bine definite (inainte si dupa ciocnire). Aceste marimi probeaza in intregimea lor Suprafetele de Energie Potentiala (SEP) ale sistemelor atom-diatom sau diatom-diatom in studiu. Metodele experimentale ultilizate sunt: expansiunea supersonica a fasciculelor moleculare, descarcare electrica pentru productia radicalului hidroxil, camp electrostatic neomogen pentru a focaliza si selecta moleculele OH intr-o singura stare de energie interna bine definita (starea cu simetrie *f* a dubletului Λ al nivelului fundamental de energie rotationala), fluorescenta-indusa-laser pentru a proba populatia moleculelor OH excitate prin ciocniri, ionizare rezonanta multi-foton si proiectia vitezei pentru detectia hidrurilor halogenate sau a produsilor imprastierii reactive. De asemeni, un camp electrostatic omogen este utilizat pentru a orienta moleculele OH ori cu partea hidrogenului ori cu partea oxigenului catre partenerul de ciocnire.

1. Interactia OH-Hidruri Halogenate

Reactiile hidrurilor halogenate cu radicalul hidroxil sunt caracterizate prin sectiuni eficace si entalpii de reactie mari. Produsi direct sau prin intermediari CH_3X, in oceane, vulcani, plasma ori tehnologii industriale, compusii halogenati sunt foarte activi in procesele chimice ale atmosferei terestre. Ei pot cataliza, spre exemplu, procesele care determina distrugerea stratului de ozon.

Masuratori efectuate in reactoare au permis determinarea ratelor termice ale reactiilor OH + HX, cu X = Cl, Br si I, pentru domenii largi de temperatura. Ratele la T = 298 K si exotermicitatile acestor reactii cresc cu dimensiunea atomului de halogen. Analiza SEP indica prezenta unor complecsi van der Waals puternic legati, datorati in principal interactiunii bazate pe momentele electrice permanente ale moleculelor in studiu.

Experimentele prezentate in aceasta lucrare au ca scop studiul imprastierii inelastice si reactive in conditii de energie de ciocnire, energie interna si orientare a moleculelor OH bine definite. Marimile masurate sunt sectiunile eficace relative si asimetriile sterice - masura a efectului orientarii moleculelor OH asupra acestor sectiuni eficace.

Sectiunile eficace de imprastiere inelastica rotationala obtinute indica similaritati intre sistemele moleculare OH-HCl, OH-HBr si OH-HI. In general, domina tranzitiile care conserva componenta spin-orbita, tranzitia de Λ-dublet prezinta cea mai mare sectiune eficace, iar marimea sectiunilor eficace scade cu cresterea excitarii rotationale. Cea mai rapida scadere apare pentru ciocnirile moleculelor de hidroxil cu molecule de hidrura de iod, singurul sistem pentru care este observata o preferinta pentru o anumita simetrie a starii de energie interna a radicalului OH.

Asimetriile sterice masurate sugereaza ca potentialul de interactie OH-HCl e cel cel mai anizotropic. Valori ale asimetrei mici sunt obtinute pentru imprastierea OH-HBr si OH-HI. Este discutata o posibila corelare a marimii si semnului asimetriilor sterice cu configuratiile moleculare corespunzatoare minimelor SEP si cu posibilele reactii.

Produsii de reactie nu au fost detectabili in conditiile experimentale date, probabil datorita sensitivitatii scazute si semnalului datorat fotodisocierii halidelor. Metode de detectie care necesita ionizare laser, cu fotoni de energii in afara domeniului de absorptie a hidrurilor halogenate, sau fluorescenta-indusa-laser ar trebui considerate. Este recomandabila de asemeni cresterea densitatii de molecule OH prin relaxarea conditiei de puritate a starii de energie interna sau prin utilizarea unei alte metode de productie a radicalului hidroxil. Studiul sectiunilor eficace diferentiale inelastice si reactive si, in particular, probarea complecsilor intermediari pot contribui semnificativ la investigarea mai in detaliu a acestor interactii.

2. Intercatia OH-Gaze Rare

Numeroase lucrari teoretice si experimentale au avut ca scop studiul interactiilor radicalului hidroxil cu gazele rare. Aceste studii se refera in particular la OH-He si OH-Ar. In aceasta lucrare sunt prezentate sectiunile eficace inelastice si asimetriile sterice masurate pentru imprastierea radicalului hidroxil de catre xenon.

Rezultatele experimentale sunt comparate cu rezultatele calculelor teoretice care trateaza acest sistem si cu rezultatele pentru imprastierea OH-He si OH-Ar raportate anterior. Diferente majore sunt observate. Termenii radiali ai expansiunii potentialului de interactie in polinoame Legendre pot fi corelati cu marimea relativa a sectiunilor eficace pentru tranzitii ale moleculelor OH pe diferite nivele de energie interna, tranzitii induse prin ciocniri. Asemenea corelare indica o crestere a predominantei termenului V_{10} cu polarizabilitatea si dimensiunea gazului rar care ciocneste moleculele de OH. Este foarte probabil ca acest termen V_{10} reflecta taria interactiei dipol-dipol indus. Fortele de interactie la distante interatomice mari pot fi mai puternice pentru OH-Xe decat pentru OH-He si OH-Ar, datorita dimensiunii si polarizabilitatii mai mari ale atomilor de xenon. Intr-adevar, pentru OH-Xe s-au obtinut cele mai mari sectiuni eficace pentru cele mai mici excitari rotationale care sunt induse in mare parte de ciocniri la parametrii mari de impact. O similara descrestere a sectiunilor eficace inelastice cu cresterea excitarii rotationale a fost observata la imprastierea moleculelor OH de catre molecule polare. Preferinta semnificativa pentru starile de energie interna cu simetrie *e* si dominatia termenilor V_{22} si V_{20} prezente la interactiile OH-Ar si OH-He, pot fi atribuite fortelor de natura cuantica de interactiune la distanta internucleara mica.

Nu este inca gasita o explicatie a neconcordantelor dintre sectiunile eficace teoretice si cele experimentale pentru imprastierea OH-Xe. De aceea, o explorare teoretica mai in detaliu a intercatiei OH-Xe si a contributiei la aceasta intercatie a fiecarui tip de forte intermoleculare este necesara.

Acknowledgments

During my PhD study I met many people to whom I have now the joy to thank for the help, patience, advise, instruction, support, friendship, encouragement…Dank u well! Nanedri! Xièxie! Hvala! Спасибо! Grazie! Blagodaria! Děkuji! Mulţumesc!

I thank Prof. dr. J.J. ter Meulen and Prof. dr. D.H. Parker for leadership and supervision, for making possible such an achievement for me. Many thanks to the "emergency team": Leander Gerritsen, Peter Claus, Cor Sikkens and André van Roij for the technical expertise. I am very grateful to Leander for the exceptional handling of so large number of demands for this project, culminating with taming beasts like HCl, HBr and HI.

I would like to thank the members of the manuscript committee, Prof. ir. A. van der Avoird, Dr. N.J. Dam and Prof. dr. S. Stolte.

Rogier Evertsen helped me for the first and short assignment in the laboratory of our department, than Raluca Cireaşă was my tutor for more than 2 years. Calde mulţumiri, Raluca! Thanks to Koen and Michiel, who's previous work I have used and continued, to prof. D.H. Parker, Dr. N.J. Dam and Dr. F.J.M. Harren for the useful courses I have followed, to Dr. N.J. Dam for laser troubleshooting, to Dr. J. Kłos, Dr. ir. G.C. Groeneboom and Prof. dr. ir. A. van der Avoird for the complementary theoretical work and helpful discussions. Thanks to Prof. dr. W. van der Zande and Prof. dr. L. Meerts for advises, to our secretaries Ine, Erna and Magda, to all the department colleagues, office mates and friends among whom: Gowri, Kostya, Chung-Hsin, Yongwei, Dragana, Malcom, Dmitri, André, Ivo, Afric, Arijan, Jeroen, Li, Ivan, Reyer, Kijeld, the Diesel team, the "photo-acoustic group", the Probe team, Flaminia, Viola, Anna, Liesbeth, Svetlana, Frantisek, Sergiy, Kotayba... High regards for such nationally and culturally colorful bouquet of people!

I appreciate the opportunities for good professional environment and facilities, colloquia, symposia, conferences and FOM courses. I have enjoyed our dagen-uit, borrels, movie evenings, vierdaagse feesten, "national evenings" or study-group meetings.

Mulţumiri comunităţii româneşti cu pr. Dura, Elena de Chiara, Raluca, Marcela, Angela, Adriana, Ana şi Cătălin, Mihaela Goronea, Iulia si Marius, Simona si Sacco-Andrei, Nico şi Lulu, Mihaela şi Dan, Alice şi Lucian, Miruna, Lucian Ancu, Delia şi Călin, Elena şi Viorel, Roxana, Andrei, Călin şi Alina Zamfirescu, Ema, Ramona si Leo, Florin Sabo, Nicu si Roberta , de asemeni celor de acasă: dragi părinţi si mamaie, Fănică, Lidi şi Gabi, Ioana si Daria, Măriuca si Fănel, pr. Ilie, Steluţa, Irinel, M. Salomeea, A. Ioanid, M. Podgoreanu, C. Necula, M. Păiş, I. Tătulescu…

List of publications

-Inelastic state-to-state scattering of OH ($^2\Pi_{3/2}$, J = 3/2, f) by HCl
R. Cireasa, M.C. van Beek, A. Moise and J.J. ter Meulen, J. Chem. Phys. 122, 074319 (2005)

-Steric effects in state-to-state scattering of OH ($^2\Pi_{3/2}$, J = 3/2, f) by HCl
R. Cireasa, A. Moise and J.J. ter Meulen, J. Chem. Phys. 123, 064310 (2005)

-Rotationally inelastic scattering of OH ($^2\Pi_{3/2}$, v = 0, J = 3/2, f) by HBr ($^1\Sigma$, v = 0, J < 4)
A. Moise, R. Cireasa, D.H. Parker and J.J. ter Meulen, J. Chem. Phys. 125, 204315 (2006)

-State-to-state inelastic scattering of OH by HI
A. Moise, D.H. Parker and J.J. ter Meulen, J. Chem. Phys. 126, 124302 (2007)